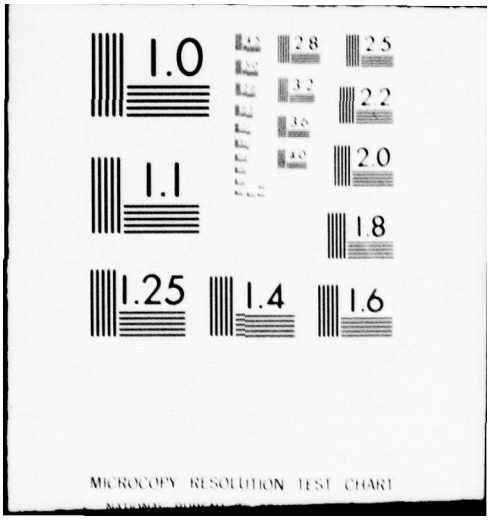
AD-A060 892 PENNSYLVANIA STATE UNIV UNIVERSITY PARK APPLIED RESE--ETC F/G 21/5
INVESTIGATION OF THE UNSTEADY PRESSURE DISTRIBUTION ON THE BLAD--ETC(U)
MAR 78 R E HENDERSON, G F FRANKE N00017-73-C-1418
UNCLASSIFIED ARL/PSU/TM-78-54 NL

1 OF 2
AD
A060 892




1.0
1.1
1.25
1.4
1.6
1.8
2.0
2.2
2.5
2.8
3.2
3.6
4.0
MICROCOPY RESOLUTION TEST CHART

AD A060892

LEVEL II

12 B.S.

INVESTIGATION OF THE UNSTEADY PRESSURE DISTRIBUTION ON THE BLADES OF AN AXIAL FLOW FAN

R. E. Henderson and G. F. Franke

12 142 p.

DDC FILE COPY

DDC RECEIVED NOV 7 1978 F

Technical Memorandum
File No. TM 78-54
14 March 1978
Contract No. N00017-73-C-1418
NGR-39-009-275
Copy No. 17

ARL/PSU TM-78-54

The Pennsylvania State University
APPLIED RESEARCH LABORATORY
Post Office Box 30
State College, PA 16801

Approved for Public Release
Distribution Unlimited

NAVY DEPARTMENT

NAVAL SEA SYSTEMS COMMAND

391 007
78 11 02 024

UNCLASSIFIED

SECURITY CLASSIFICATION OF THIS PAGE *(When Data Entered)*

REPORT DOCUMENTATION PAGE		READ INSTRUCTIONS BEFORE COMPLETING FORM
1. REPORT NUMBER TM 78-54	2. GOVT ACCESSION NO.	3. RECIPIENT'S CATALOG NUMBER
4. TITLE *(and Subtitle)* INVESTIGATION OF THE UNSTEADY PRESSURE DISTRIBUTION ON THE BLADES OF AN AXIAL FLOW FAN		5. TYPE OF REPORT & PERIOD COVERED Technical Memorandum 6. PERFORMING ORG. REPORT NUMBER
7. AUTHOR(s) R. E. Henderson and G. F. Franke		8. CONTRACT OR GRANT NUMBER(s) NASA Research Grant No. NGR 39-009-275
9. PERFORMING ORGANIZATION NAME AND ADDRESS Applied Research Laboratory Post Office Box 30 State College, PA 16801		10. PROGRAM ELEMENT, PROJECT, TASK AREA & WORK UNIT NUMBERS
11. CONTROLLING OFFICE NAME AND ADDRESS NASA Lewis Research Center; Cleveland, OH Naval Sea Systems Command; WA, DC - Code 035		12. REPORT DATE 14 March 1978 13. NUMBER OF PAGES 137
14. MONITORING AGENCY NAME & ADDRESS*(if different from Controlling Office)*		15. SECURITY CLASS. *(of this report)* UNCLASSIFIED 15a. DECLASSIFICATION/DOWNGRADING SCHEDULE

16. DISTRIBUTION STATEMENT *(of this Report)*

Approved for public release. Distribution unlimited.
Per NAVSEA - Oct. 5, 1978

17. DISTRIBUTION STATEMENT *(of the abstract entered in Block 20, if different from Report)*

18. SUPPLEMENTARY NOTES

19. KEY WORDS *(Continue on reverse side if necessary and identify by block number)*

axial flow
fan
unsteady pressure
transducers
turbomachinery
noise

20. ABSTRACT *(Continue on reverse side if necessary and identify by block number)*

The results are presented of a program to investigate the distribution of unsteady pressure on the blades of a stator blade row which operated in the wakes of an upstream rotor. These unsteady pressure distributions were measured using a blade instrumented with a series of miniature pressure transducers which was developed in this program. The influence of several geometrical and flow parameters - rotor/stator spacing, stator solidity and stator incidence angle - were studied to determine the unsteady response

DD FORM 1 JAN 73 1473 EDITION OF 1 NOV 65 IS OBSOLETE

UNCLASSIFIED

SECURITY CLASSIFICATION OF THIS PAGE *(When Data Entered)*

20. of the stator to these parameters.

These studies indicate a major influence on the stator unsteady response is due to the stator solidity. At high solidities the blade-to-blade interference has a larger contribution. While the range of rotor/stator spacings investigated had a minor influence, the effect of stator incidence angle is also significant. The data indicate the existence of an optimum positive incidence which minimizes the unsteady response. Further studies are recommended to determine the characteristics of the propagation of the wakes over the stators and behavior of the surface flow during this interaction.

ACCESSION for
NTIS White Section
DDC Buff Section
UNANNOUNCED
JUSTIFICATION
BY
DISTRIBUTION/AVAILABILITY CODES
Dist. SPECIAL
A

Subject: Investigation of the Unsteady Pressure Distribution on the Blades of an Axial Flow Fan

References: See page 127.

Abstract: The results are presented of a program to investigate the distribution of unsteady pressure on the blades of a stator blade row which operated in the wakes of an upstream rotor. These unsteady pressure distributions were measured using a blade instrumented with a series of miniature pressure transducers which was developed in this program. The influence of several geometrical and flow parameters - rotor/stator spacing, stator solidity and stator incidence angle - were studied to determine the unsteady response of the stator to these parameters.

These studies indicate a major influence on the stator unsteady response is due to the stator solidity. At high solidities the blade-to-blade interference has a larger contribution. While the range of rotor/stator spacings investigated had a minor influence, the effect of stator incidence angle is also significant. The data indicate the existence of an optimum positive incidence which minimizes the unsteady response. Further studies are recommended to determine the characteristics of the propagation of the wakes over the stators and behavior of the surface flow during this interaction.

Acknowledgment: This study was conducted under the primary sponsorship of NASA Research Grant No. NGR 39-009-275, Lewis Research Center. The administration of this grant was conducted through the Department of Mechanical Engineering, The Pennsylvania State University. Partial support was provided by the U. S. Navy, Naval Sea Systems Command, Code 035, through the Applied Research Laboratory, The Pennsylvania State University (ARL/PSU) which made available the facilities used in this study.

Table of Contents

	Page
Abstract	1
Acknowledgments	1
Nomenclature	4
List of Figures	6
INTRODUCTION	9
STATUS OF EXISTING KNOWLEDGE	10
Theoretical Prediction of Unsteady Blade Response	10
Experimental Study of Unsteady Blade Response	13
STATEMENT OF PROBLEM AND SCOPE OF WORK	14
DESCRIPTION OF FLOWS STUDIED	15
Figures	18
EXPERIMENTAL APPARATUS AND TEST PROCEDURE	21
EXPERIMENTAL APPARATUS	21
Axial Flow Research Fan	21
Instrumented Stator	22
Instrumented Rotor	24
Flow Field Measurements	25
DATA ACQUISITION	27
Instrumentation and Signal Conditioning	27
A to D Conversion and Ensemble Averaging	31
INSTRUMENT CALIBRATION	32
Instrumented Stator	32
Static Calibration	32
Dynamic Calibration	33
Instrumented Rotor	36
Hot-Film Anemometer	36
Figures	38
PRESENTATION AND DISCUSSION OF EXPERIMENTAL RESULTS	61
ROTOR WAKES	61
UNSTEADY STATOR BLADE PRESSURES	64

Page

UNSTEADY ROTOR LIFT 72

Figures 74

COMPARISON OF THEORETICAL AND EXPERIMENTAL RESULTS 108

Figures 117

SUMMARY AND CONCLUSIONS 119

RECOMMENDATIONS 124

ACKNOWLEDGMENTS 126

REFERENCES 127

Appendix A - THEORETICAL RESPONSE OF TUBE-CAVITY SYSTEMS . 132

Nomenclature

c	- chord length (m)
C_N	- Fourier modulus
$C_{p_{rms}}$	- defined in Equation (1)
i	- angle of incidence (degrees)
$\tilde{L}$	- unsteady lift (newtons)
$\tilde{M}$	- unsteady moment (newton-m)
p	- time-mean static pressure (newtons/m^2)
$\tilde{p}$	- unsteady pressure (newton/m^2)
p_{atm}	- atmospheric pressure (newtons/m^2)
r	- radius (m)
R/S	- rotor/stator axial spacing in fraction of rotor chord
s	- blade spacing (m)
S_x	- axial spacing between blade rows (m)
t	- time (s)
T'_o	- nondimensional time
u,v	- perturbation velocities in x,y direction
U	- blade rotational velocity (m/s)
V	- absolute velocity (m/s)
V_x	- axial velocity, (m/s)
w	- wake or distortion deficit (m/s)
W	- relative velocity (m/s)
W_{max}	- maximum wake velocity deficit (m/s)
x,y	- cartesian coordinates
α	- absolute flow angle (degrees)
β	- relative flow angle (degrees)
ζ	- vorticity

θ - circumferential position, or defined equation (3)

λ - wake thickness parameter

ξ - stagger angle, or wake coordinate

σ - solidity (c/s)

ϕ - phase angle

Subscripts

d - disturbance

m - mean radius

R - rotor

S - stator

1 - inlet

2 - exit

80 11 02 024

List of Figures

Figure 1 - General Disturbance Flow in a Cascade

Figure 2 - Rotor Wake Flow Relative to the Rotor Blade

Figure 3 - Rotor Velocity Diagram at Inlet and Exit

Figure 4 - Rotor Wake in Relative and Fixed Coordinates

Figure 5 - Axial Flow Research Fan

Figure 6 - Installation of Stators in AFRF

Figure 7 - Instrumented Stator Blade

Figure 8 - Instrumented Stator Blade Cross Section and Transducer Mounting Arrangement

Figure 9 - Dimensions of Transducer Cavities and Predicted Resonant Frequencies

Figure 10 - Schematic of Pitran Transducer

Figure 11 - Pitran Signal Conditioner

Figure 12 - Instrumented Rotor Blade

Figure 13 - Circumferential Location of Probes and Instrumented Stators

Figure 14 - Instrumentation and Data Acquisition Schematic

Figure 15 - Schematic of Hot-Film Anemometer Signal Conditioner

Figure 16 - Phase Shift Introduced by Krohn-Hite Filter

Figure 17 - Unfiltered and Filtered Hot-Film Output

Figure 18 - Comparison of Fourier Modulus of Unfiltered and Corrected Filtered Hot-Film Data

Figure 19 - Comparison of Phase Angle of Unfiltered and Corrected Filtered Hot-Film Data

Figure 20 - The Effect of the Number of Ensemble-Averaging Sums on Typical Pitran Output

Figure 21 - Schematic of Pitran Static Calibration Setup

Figure 22 - Pitran Static Calibration Apparatus

Figure 23 - Typical Pitran Static Calibration Data

Figure 24 - Schematic of Pitran Dynamic Calibration Setup

Figure 25 - Results of Dynamic Calibration of Pitran at x/c=0.15

Figure 26 - Results of Dynamic Calibration of Pitran at x/c=0.95

Figure 27 - Dynamic Response of Instrumented Rotor Blade

Figure 28 - Schematic of Hot-Film Calibration Tunnel

Figure 29 - Typical Hot-Film Calibration Data

Figure 30 - Rotor Wake at the Stator Leading Edge

Figure 31 - Spectral Analysis of Typical Hot-Film Output

Figure 32 - Variation of Instantaneous Angle of Incidence About Time-Mean Incidence Angle, R/S=0.5

Figure 33 - Typical Spectral Representation of Pitran Output

Figure 34 - Unsteady Pressure Coefficient versus Real Time-Suction Surface, i = -2.0 deg

Figure 35 - Unsteady Pressure Coefficient versus Real Time-Pressure Surface, i = -2.0 deg

Figure 36 - Unsteady Pressure Coefficient versus Real Time-Suction Surface, i = 17.0 deg

Figure 37 - Unsteady Pressure Coefficient versus Real Time-Pressure Surface, i = 17.0 deg

Figure 38 - Unsteady Pressure Coefficient During the Passage of a Single Rotor Wake, i = -2.0 deg

Figure 39 - Unsteady Pressure Coefficient During the Passage of a Single Rotor Wake, i = 5.0 deg

Figure 40 - Unsteady Pressure Coefficient During the Passage of a Single Rotor Wake, i = 17.0 deg

Figure 41 - Unsteady Pressure Phase Angle versus x/c-R/S=0.5, σ=0.493

Figure 42 - Unsteady Pressure Phase Angle versus x/c-R/S=0.5, σ=0.986

Figure 43 - Unsteady Pressure Phase Angle versus x/c-R/S=2.0, σ=0.493

Figure 44 - Unsteady Pressure Phase Angle versus x/c-R/S=2.0, σ=0.986

Figure 45 - Suction and Pressure Surface Phase Angle Difference versus Incidence Angle - Blade Passing Harmonic

Figure 46 - Suction and Pressure Surface Phase Angle Difference versus Incidence Angle - Twice Blade Passing Harmonic

Figure 47 - Relative Phase Angle Along Suction Surface with Incidence Angle - Blade Passing Harmonic

Figure 48 - Variation of $C_{p_{rms}}$ with Rotor/Stator Spacing at x/c=0.02

Figure 49 - Variation of $C_{p_{rms}}$ with Solidity at x/c=0.02

Figure 50 - Variation of $C_{p_{rms}}$ with Incidence Angle at x/c=0.02

Figure 51 - Variation of $C_{p_{rms}}$ with Chordwise Position

Figure 52 - Magnitude of Unsteady Lift Gauge Output versus Harmonic Number, R/S=0.5 and i = 17.0 degrees

Figure 53 - Compressor Blade Wake Interaction Considered by Meyer [12]

Figure 54 - Comparison of Measured and Predicted $C_{p_{rms}}$

Figure A-1 - Cavity-Tube Model

Figure A-2 - Orifice Resistance Ratio versus Mach Number, [44]

Figure A-3 - Mach Number Effects on Cavity-Tube Response, [45]

INTRODUCTION

In present day high bypass aircraft engines, the major source of noise is that generated by the fan. This noise arises as a result of the unsteady pressures (and, hence, lift and moment) generated on the blades due to potential interactions, interactions with wakes from upstream blades, inlet flow distortions and inlet turbulence [1,2]. The prediction of this radiated noise, and its eventual reduction, is dependent upon a knowledge of the unsteady forces which occur on the blades as discussed by Bragg and Bridge [3] and Morfey [4]. To reduce the source of fan noise in a high bypass aircraft engine, requires that the fan designer be able to predict, with a known level of confidence, the unsteady pressures, forces and moments acting on the blades as a function of the design parameters at his disposal, and the characteristics of the disturbance. These design parameters include: blade rotational speed, blade solidity, stagger angle, blade incidence angle, blade camber, blade thickness, and spacing between adjacent blade rows.

To date, there is a lack of such unsteady design data. The reasons for this are twofold: (1) most available theoretical design methods represent the unsteady response of the turbomachine blades as that of an isolated, flat plate airfoil, thus ignoring the effects of camber, thickness and solidity, and (2) the acute lack of experimental measurements to demonstrate the validity of available theories, and the effects of the various design parameters. The purpose of the subject program was to obtain experimental data to demonstrate the influence rotor/stator spacing, solidity and steady loading (incidence angle) on the unsteady pressures generated on

a stator row located downstream of a rotor. A major portion of this program was the development of an instrumented stator blade to measure the unsteady pressure distribution.

STATUS OF EXISTING KNOWLEDGE

The occurrence of unsteady lift and moments on the rotating or stationary blades of an axial flow fan stage is caused by the spatially and temporally varying flow field experienced by the blades. For a moving blade row, or rotor, these variations arise from the passage of wakes shed by upstream blades, potential interactions with adjacent stationary blade rows, inlet distortions, wall protuberances, and inlet turbulence. These wakes and distortions represent spatial variations in velocity which, while stationary with respect to the casing wall, appear as time variations to the rotor or as wakes moving past a downstream stator when they are shed from an upstream rotor. Figure 1 is representative of such a flow and depicts the flow on a cylindrical surface through a blade row in which a spatial variation exists in the inlet velocity to the rotor. The wakes of an upstream rotor will similarly appear as a time-varying flow to downstream stator blades. These periodic spatial variations in velocity lead to the pure tone or blade-passing-frequency noise observed in present day fan engines. This research program is restricted to the examination of this source of the noise generated by a fan.

Theoretical Prediction of Unsteady Blade Response

The majority of the theoretical analyses available for predicting the unsteady pressure distribution, lift or moment on a blade row experiencing a periodically varying flow of the general type shown in Figure 1 are based on the assumption that the unsteady response can be represented as that of an isolated airfoil operating in a

two-dimensional, inviscid, incompressible flow. Perhaps the best known theory for the prediction of the unsteady lift and moment is the method by Kemp and Sears [5,6]. This method is based on earlier work by von Karman and Sears [7] and Sears [8] which defines the unsteady lift and moment on an isolated airfoil exposed to a sinusoidally fluctuating velocity normal to its chord. Horlock [9] later analyzed the effects of velocity perturbations parallel to the chord and combined his results with those of von Karman and Sears to treat the case of a generalized velocity perturbation. More recently Naumann and Yeh [10] have extended Horlock's isolated airfoil analysis to include the effects of camber. The results of Naumann and Yeh are presented in a form which the designer could utilize to minimize the unsteady response and, hence, the source of radiated noise. While it is shown in [10] that the effects of stagger angle and camber can be significant, the effects of solidity are ignored because of the assumption that the unsteady flow over the neighboring blades in the blade row do not contribute to the unsteady response of the blade of interest.

The unsteady pressure distribution which exists on the blades could be estimated using the above-mentioned isolated airfoil theories. Each of these theories contains an expression for the unsteady pressure difference which is integrated to obtain the unsteady lift and moment. These methods require that the velocity deficits shown in Figure 1 be represented as Fourier series. The total response of the blade is then found by summing the response to each term in the Fourier Series. Studies have also been conducted by Yeh and Eisenhuth [11], Meyer [12], and Lefcort [13] to estimate the unsteady pressure distribution which results from the passage of a narrow strut wake over an isolated airfoil.

In contrast with the isolated airfoil analyses discussed above, are the available analyses of the response of a cascade of airfoils. Several authors, for example, Whitehead [14,15], Lotz and Raabe [16], and Smith [17], have developed analytical methods to describe the vibration of a blade row when operating in a spatially varying inflow and account for the unsteady contribution of the entire cascade. The analyses of Whitehead and Smith can also be used to predict the unsteady lift and moment for rigid, nonvibrating blades experiencing spatial velocity variations, if the blades are assumed to be uncambered flat plates which respond only to velocity variations normal to the chord. Arnoldi [18] discusses the combination of Whitehead's analysis with that of Horlock [9] to analyze the unsteady lift in a moving blade row.

The analysis of Henderson and Daneshyar [19] permits the prediction of the unsteady lift generated in a two-dimensional, nonvibrating cascade due to interaction with a sinusoidally varying inlet flow. This model includes the unsteady contribution of the neighboring blades and the effects of blade camber and angle of incidence. By utilizing this analysis, the unsteady lift on a blade in the blade row can be expressed in the form of a Sears and Horlock Function for a cascade. Comparisons of the analysis of [19] and that by Whitehead and Smith indicate good agreement in the predicted values of unsteady lift except at conditions where the spacing of the cascade equals the wave length of the disturbance. These comparisons are presented and discussed in [20]. Reference [21] presents the results of a series of calculations conducted using the analysis of [19] which show the variation of unsteady lift with blade stagger angle, solidity and the reduced frequency.

Experimental Studies of Unsteady Blade Response

As discussed above, one reason for the lack of cascade blade design data which includes unsteady flow effects is the lack of experimental measurements. Yeh and Eisenhuth [11] and Lefcort [13] have conducted experiments showing the effect of the interaction of a single airfoil with a thin, finite wake. Fujita and Kovasznay [22] have conducted experiments with a single airfoil and compared these results with the analysis by Meyer [12]. They found reasonably good agreement with the data in the absence of flow separation.

Holmes [23] has measured the time-dependent pressure distribution and total lift on an uncambered isolated airfoil operating in a sinusoidally varying, nonconvected inflow at very low reduced frequencies. These data show good agreement with the analysis by Kemp [24] which extends the analysis of Sears to treat a nonconvected gust. The experiments by Holmes have been extended by Satyanarayana [25] to include the effects of a cascade. These experiments demonstrated a definite effect of solidity on the unsteady pressure distributions and the lift generated in a cascade. Comparisons of these data with the predicted unsteady lift are presented in [26]. The characteristics of the unsteady boundary layer on this cascade are discussed in [27] and [28].

The experimental evaluation of the unsteady lift and pitching moment on a blade of an axial flow rotor due to the interaction with inlet distortions is reported by Bruce and Henderson [29]. These data are compared with the theoretical predictions of [14], [17] and [19]. In general, the comparisons are good. The effects

of stagger angle, rotor steady loading and solidity on the generation of unsteady rotor response are presented.

STATEMENT OF PROBLEM AND SCOPE OF THE WORK

The purpose of this study was to investigate the unsteady response of a stator blade row to the wakes shed by an upstream rotor. A major effort required in this program was the development of an instrumented stator blade to permit the measurement of the unsteady pressures on the stator. Employing this instrumentation, experiments were conducted to determine the unsteady pressures on the stator as a function of stator solidity, stator mean angle of incidence and rotor/stator spacing.

The unsteady response of the stator blades to the wakes shed by an upstream rotor was determined by measuring the unsteady pressure at various locations along the chord, at the midspan of the blade. These measurements were conducted at the blade midspan to minimize the effects of the annulus wall boundary layer and provide a nearly two-dimensional flow. A hot-film anemometer was used to measure the velocity field at the midspan of the stator blades.

The unsteady response of the rotor to the presence of the stator blades was determined by measuring the unsteady lift and moment at the midspan of a rotor blade. These measurements were obtained by instrumenting an independently supported section of a rotor blade with strain gauges. This blade was developed under the sponsorship of Project SQUID [29] and was available for use in this program.

The unsteady response of both the rotor and stator was determined for two values of rotor-to-stator spacing, 2.0 and 0.5 rotor chord

lengths, two values of stator solidity, 0.493 and 0.986, three values of rotor incidence angle, 0.5°, 5.1°, and 10.1° and three corresponding values of stator incidence angle, -2.0°, 5.0° and 17.0°.

The unsteady pressure measurements were compared with the results of the analysis by Lefcort [13] of the pressure distribution on an isolated airfoil interacting with a local velocity perturbation caused by viscous wake.

This investigation does not consider all the aspects of unsteady turbomachinery flow. Specifically, the effects of rotor and stator camber, rotor and stator stagger angle, rotor solidity, and blade thickness are excluded. All measurements were made at the midspan of the blades. Although the flow at several conditions tested was three-dimensional, the flow in the radial direction was assumed to be zero. The effect of this radial flow is assumed small; however, this assumption was not verified experimentally. The variation of the unsteady performance at other spanwise locations was not examined.

DESCRIPTION OF THE FLOWS STUDIED

As discussed above, only the flow and unsteady response at the blade midspan was considered in this study. This means that the flow in the radial direction is ignored. In addition, the flow is considered to be incompressible since the velocities relative to the blades were less than 45.72 mps. The development of a cylindrical surface with the radius of the blade midspan, r_m, gives the flow depicted in Figure 1 for a rotor operated downstream of a stator row. In this study the configuration considered is a rotor and a downstream stator. In this case the rotor will shed wakes which will

interact with the downstream stators row. While the wakes relative to the rotor blades will appear similar to those shed from the upstream stator, Figure 2, the rotor wakes when viewed relative to the casing or downstream stator have a different appearance.

The rotor row has a linear velocity U at the mean radius due to the rotation of the rotor. The rotor inlet and exit flow can be expressed in a frame of reference moving with the rotor speed U, or in a frame of reference fixed to the machine casing. Figure 3 shows inlet and exit velocities in both moving and fixed coordinates. When viewed in moving coordinates, Figure 4, the rotor wake flow has a uniform direction but exhibits a local region of decreased velocity. The difference between the local velocity and the velocity outside the viscous wake is the velocity deficit, w. This velocity deficit can also be viewed as a fluid jet in a direction opposite the main flow. The total flow is then the sum of an idealized uniform flow and a fluid jet, which can be considered as a perturbation to the uniform flow.

When the wake velocity profile is transformed to stationary or fixed coordinates, the velocity deficit becomes skewed and is at an angle with the main flow, Figure 4. The flow outside the region of the wake is at an angle α while the angle of the flow varies in the wake. When this flow impinges on a downstream blade, the velocity deficit causes the blade to experience a changing angle of incidence.

The flow interacting with the downstream stator is unsteady due to several factors. The turbulence in the flow causes random fluctuations and, hence, unsteadiness in the flow. As a consequence of the relative motion between the wake and the stator, the angle

of incidence of the flow changes, giving an unsteadiness or time variation. Although the wakes from each rotor blade are considered identical, small differences in the rotor blades cause differences in their wakes. This causes an additional spatial difference in the flow field in the circumferential direction.

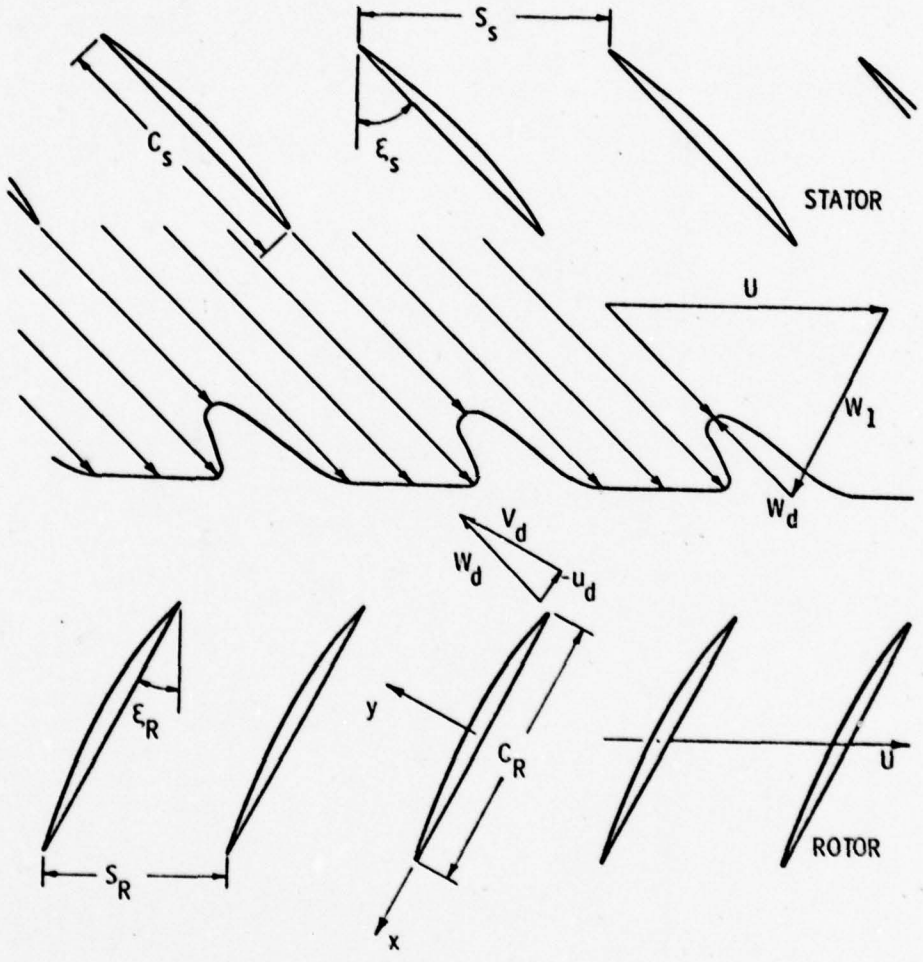


Figure 1 - General Disturbance Flow in a Cascade

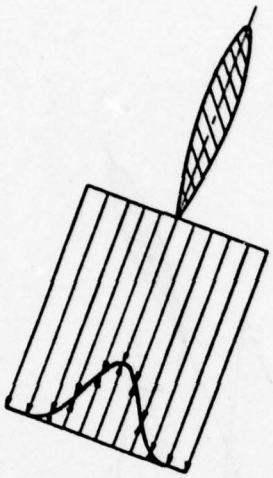


Figure 2 - Rotor Wake Flow Relative to the Rotor Blade

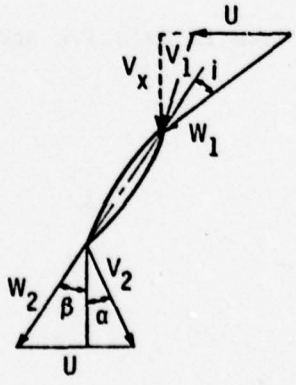


Figure 3 - Rotor Velocity Diagram at Inlet and Exit

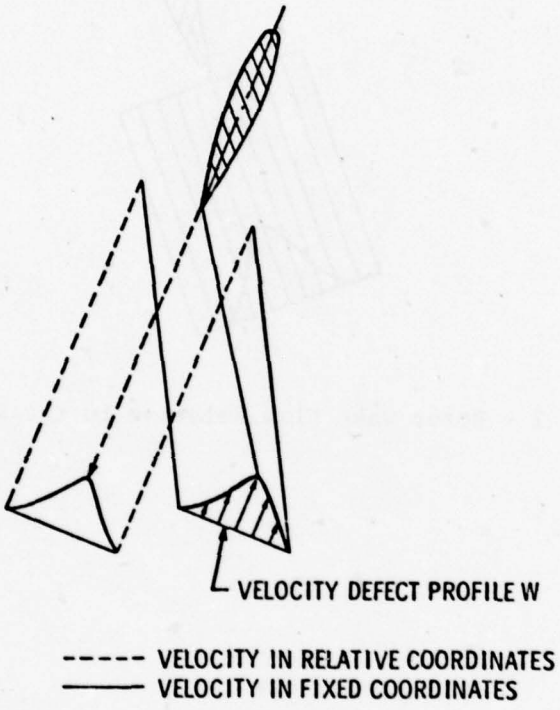


Figure 4 - Rotor Wake in Relative and Fixed Coordinates

EXPERIMENTAL APPARATUS AND TEST PROCEDURE

EXPERIMENTAL APPARATUS

Axial Flow Research Fan

The Axial Flow Research Fan (AFRF), Figure 5, consists of a bellmouth inlet leading to an annular flow passage with a 54.61 cm outer diameter and a 24.13 cm diameter center hub. The annular flow passage contains a rotor, stator and auxiliary fan. The rotor and stator comprise the test section and the auxiliary fan provides the air flow through the annulus.

The rotor consists of 12 aluminum blades including one blade instrumented to measure unsteady lift and moment ($\tilde{L}$ and $\tilde{M}$). The blades have a 10% thick uncambered C1 profile [30] with a chord length of 15.24 cm and span of 14.99 cm. The rotor was designed to produce zero lift at the design condition, i.e., zero angle of incidence at all blade radii. This feature simplifies the analysis of unsteady flows by eliminating steady rotor lift when operated at this condition. The rotor can produce steady lift when operated with the flow at a nonzero angle of incidence. The design stagger angle, ξ, equals 45° at the mean radius. The rotor is driven by a 14.9 kw motor contained in the center hub and located downstream of the stator.

Input power and signal transmission lines from the instrumented rotor blade run through the rotor hub to the hollow rotor shaft, to a downstream 14 channel coin silver slip-ring unit, and then out through the aft support fins.

The stator consists of 4 or 8 blades having the same cross-sectional shape as the rotor blades which can be positioned by

changing the outer casing and hub configuration to give rotor/stator spacings of 0.5 to 2.0 rotor chord lengths. This spacing is measured as the axial distance from the rotor trailing edge to stator leading edge. The stator blades are untwisted and have a stagger angle of 0°. Two of the stator blades are instrumented to measure the unsteady pressure ($\tilde{p}$) on the blade surface. A photograph of the AFRF showing the stators installed is shown in Figure 6.

The auxiliary fan, located between the rotor drive motor and and exit throttle, delivers 4.25×10^8 cubic centimeters of air per minute at a pressure of 8.9 cm of water gauge. The auxiliary fan drive motor and the rotor drive motor operational characteristics can be independently controlled by two adjustable frequency drive inverter units.

A once-per-rotor revolution voltage spike is produced to indicate the position of the rotor in each revolution. A disk with an open radial slot rotates with the rotor shaft. When the open portion of the disk passes in front of a light beam, a photocell is activated. The resulting voltage spike permits the accurate syncronization of data produced during different rotor revolutions.

A wooden enclosure covered with a thin layer of foam and screen encloses the bellmouth of the AFRF to remove any rotation in the inlet flow and to reduce inlet turbulence.

A more extensive description of the AFRF is contained in Reference [31].

Instrumented Stator

Two of the stator blades are instrumented to measure the unsteady pressures resulting from the interaction of the stators and upstream

disturbances. One blade, fabricated from aluminum, contains six transducers located at 5%, 15%, 30%, 40%, 50% and 75% of the chord. A second, brass blade contains transducers at 2%, 40% and 95% chord locations. Each blade has a transducer at 40% chord to check whether the flow over the two blades is similar.

Each instrumented blade consists of two sections that fit together to form internal cavities in which pressure transducers can be mounted. A photograph of a disassembled blade and transducer is shown in Figure 7. The transducers are mounted between a pair of o-rings which form a pressure tight seal and permit assembly and disassembly with relative ease. Each cavity is connected to the surface of the blade by holes perpendicular to the blade surface. A blade cross-section and details of the Pitran mounting arrangement are shown in Figure 8. The dimensions of the internal cavities and surface taps are shown in Figure 9. The surface taps are staggered about the mean radius in a manner which covers a spanwise extent of approximately 2.5 cm. This staggering is intended to minimize spurious pressure fluctuations caused by flow in the vicinity of an upstream surface tap on downstream transducers.

To measure pressures on only one side of a blade, the holes on the opposite side are covered with tape. Each blade also contains passages that lead from the transducer to the outside casing of the AFRF. These passages contain electrical leads and supply atmospheric pressure to the reference side of the transducer (see description of transducer below).

The transducers employed are Pitran model PT-M2 differential pressure transducers manufactured by Stow Laboratories. The Pitran is a silicon NPN planar transistor with the emitter-base junction

mechanically coupled to a diaphram as shown schematically in Figure 10. Displacement of the diaphram produces a large, reversible change in the gain of the transistor.

The Pitran transducers measure differential pressures. When installed in the stator, the unknown blade surface pressure is applied to the face of the diaphram and atmospheric pressure to the reference side of the transducer.

The advantages of the Pitran include:

1. linear output over the rated pressure range (0.25 PSID for model PT-M2);
2. high level of output signal (on the order of 1 volt per cm of water);
3. resonant frequency greater than 100,000 Hz;
4. small size (0.5 cm);
5. large overload capability (700% of rated pressure can be tolerated without damage).

The overload capability is important as the exact magnitude of the unsteady pressures on the blade is unknown. Included with the Pitran is a signal conditioner which is shown schematically in Figure 11.

Instrumented Rotor

One rotor blade is instrumented to measure unsteady force ($\tilde{L}$) and unsteady moment ($\tilde{M}$). As shown in Figure 12, a 2.540 cm span blade segment is cantilevered from the blade hub at the mid-chord position by means of a beam that has the lower portion of its length machined as a torque tube and the upper portion as a forced cube. The center section of the blade segment is located at the mean radius. The torque tube and force cube have been

instrumented using miniature strain gauges. The 2.540 cm span segment is made of magnesium to minimize its mass and moment of inertia and is structurally independent of the rotor blade except for the cantilever mount. The aluminum tip portion of the blade attaches to posts on the aluminum hub section which pass through slots in the instrumented section. A minimum clearance of 0.0127 cm is maintained at each mating surface. The magnesium segment has been mass-balanced to preclude uneven displacement. A more detailed description of this blade is presented in Reference [31].

Flow Field Measurement

Measurements were made of pertinent flow parameters in the vicinity of the stators. The axial velocity, V_x, the resultant velocity upstream of the stator, V, the angle of incidence, i, between V and the stator chord and w, the velocity defect caused by the viscous rotor wakes were determined.

The axial velocity, V_x, was determined from the static pressure (p_s) measured by a pressure tap in the fan annulus 13.5 cm downstream of the inlet bellmouth from the following relation, where p_{atm} is the atmospheric pressure

$$V_x = \sqrt{\frac{2(p_{atm}-p_s)}{\rho}} \quad .$$

A differential pressure transducer was used to measure $(p_{atm}-p_s)$ and ρ is calculated from the Perfect Gas Law. The static pressure transducer used is a variable reluctance type manufactured by Validyne Engineering Corporation. The transducer was calibrated by comparing the output voltage to the pressure indicated by a micromanometer with an identical pressure applied to each instrument.

A three-hole probe was positioned at the mean radius, approximately 3 cm upstream of the stator. The two static taps of the three-hole probe are symmetrically located on opposite sides of a wedge so that the probe can be aligned with the flow by making the static pressure at each static tap equal. An indicator on the probe and a protractor fixed to the AFRF outer casing were used to measure the angle between the wedge and an axial reference line.

A hot-film anemometer probe was located at the mean radius and equipped with a pointer and protractor to permit alignment with the flow as determined from the three-hole probe. The average velocity upstream of the stator was determined from the dc voltage output of the anemometer. The velocity profile of the rotor wake was determined from total anemometer voltage. The hot-film was a commercially available type with sensor dimensions 0.00254 cm in diameter and 0.0528 cm long.

Both the three-hole and hot-film probes were circumferentially located between the stator blades to minimize the effect of the probe wake on the flow field on the blades, Figure 13. Because of the location of probe mounting holes in the outer casing of the AFRF, it was desirable to change the probe circumferential positions when the relative postions of the rotor and stator were changed in order to mount the hot-film probe as close as possible to the leading edge of the stator. With the axial location of the hot-film probe as close as possible to the leading edge of the stator, the probe will record the rotor wake characteristics that more nearly represent the rotor wake at the stator leading edge. The hot-film probe was 2 cm upstream of the stator leading edge when the stator was positioned at rotor/stator

spacing of 2.0 chord lengths, and 2.5 cm upstream when the rotor/stator spacing equaled 0.5 chord length.

DATA ACQUISTION

Instrumentation of Signal Conditioning

Figure 14 shows a schematic of the instrumentation and signal conditioning used to obtain the measurements. The Pitran signal conditioning was performed by a Stow Laboratories model 861 Signal Conditioner. The 861 includes a Pitran biasing section with a dynamic bias stabilization loop and a variable gain isolation amplifier, shown in Figure 11. The bias current to the Pitran is continuously adjusted to cancel the response of "slow" changes. These "slow" changes are caused by variation in the pressure on the reference side Pitran diaphram and temperature effects. Thus, there is no need for zero adjustment since the stabilization circuit has a time constant of about 1 sec. With the 861 Signal Conditioner, the Pitran will respond to pressure changes that occur on the order of 1 second or faster and are, thus, well suited for measuring unsteady pressures in a turbomachine. Both the steady state pressure and voltage drift due to the Pitran and the signal conditioning electronics are ignored. The variable gain isolation amplifier permits the 861 output to be used directly with a recording device.

The output of the hot-film anemometer was conditioned to enable the tape recorder to reproduce the rotor wake characteristics with suitable accuracy. The anemometer output contains a dc voltage corresponding to the average velocity encountered and an ac portion corresponding to the fluctuating velocity in the wake of the upstream rotor blades. Since the ac signal is considerably smaller than the dc portion, the tape recorder could not reproduce the rotor

wake signal with the desired accuracy. An amplifier was designed to enhance the ac portion of the signal. A schematic of the ac amplifier is shown in Figure 15.

The amplifier consists of two operational amplifier (op-amp) circuits. In the first op-amp circuit, a resistor is adjusted manually to control a "bucking" voltage to cancel the dc portion of the signal leaving only the ac signal as the input to the second op-amp circuit. A resistor in the second op-amp circuit can be adjusted to determine the gain of the circuit. The output of the signal conditioning circuit is the amplified ac portion of the anemometer signal. The circuit gain was set at 15.00. This gain was found suitable for preparing the hot-film signal for recording.

The strain gauge signals from the instrumented rotor blade were obtained using the strain gauges as one element in a standard Wheatstone bridge. The bridge output was then amplified with a gain of 1000. A capacitor was used in the amplifier output to block the steady voltage caused by steady loading on the rotor blade and by signal drift in the electronics.

The signal of several of the Pitrans was contaminated by a large 60 Hz component. Since the Pitran output contained no significant information near this frequency (the lowest rotor blade passing frequency is 200 Hz), a high-pass filter set at 80 Hz was used to eliminate the 60 Hz signal. The output of all Pitrans and the hot-film anemometer signal were filtered at this setting.

The output of the strain gauges were filtered with a high pass filter set at 30 Hz as the lowest frequency of interest was 67 Hz. The once-per-revolution pulse was filtered with a low pass filter set at 8000 Hz which has no significant effect on the pulse. The

original purpose of filtering all the data, instead of filtering only the Pitrans having the 60 Hz contamination, was to minimize the effect of the phase shift introduced by the filter. With all data having the same phase shift it was expected that relative timing of the transducer response would be maintained.

However, the filters do introduce a phase shift as a function of input frequency. Figure 16 shows this phase shift as a function of the ratio of input frequency to the cutoff frequency of the filter as given by Reference [32]. This phase shift had a significant effect on the data. Figure 17 shows a hot-film signal that was recorded after being filtered and the same hot-film signal that was recorded unfiltered. Each signal has been ensemble averaged using 100 sums. The dramatic difference between the two signals is caused by the phase relation of the constituent frequencies and made it necessary, therefore, to correct the data. Each signal was Fourier analyzed, that is decomposed into the form,

$$\sum_{N=1}^{\infty} C_N \cos(N\theta - \phi_N) \quad .$$

The Fourier analysis of the unfiltered signal considered the first 60 terms of the Fourier series and the filtered signal calculated from the first 60 terms with the phase angle ϕ was adjusted to compensate for the filter. Figures 18 and 19 show the magnitude and phase of these signals. Since these two signals are virtually identical, it is feasible to use the Fourier analyses and phase shift compensation technique to correct the data.

The tape recorder used was a Bell and Howell seven channel FM data tape recorder. The recorder was operated at 4.76 cm/s

resulting in a cutoff frequency of 1250 Hz. This was sufficient to record four times the highest blade passage frequency encountered. Subsequent frequency analysis of all the signals showed this frequency limit to be adequate. Frequencies greater than 1250 Hz were present in several hot-film signals; however, their magnitude was not sufficient to influence the results. Only four of the tape recorder channels were used, these channels were on the same recording head, to eliminate the phase shift introduced by using different recording heads. To record the twelve channels of information (nine Pitrans, two strain gauges and the hot-film anemometer), 3 channels plus the syncronization pulse were recorded, then 3 different channels were recorded, while the operating condition of the AFRF remained unchanged. This process was repeated until all the data was recorded. The four channels being recorded were monitored on an oscilloscope at the tape recorder input and at the tape recorder reproduce terminal to assure that all signals were being recorded properly.

As the data was being recorded, the signal from each reproduce terminal of the tape recorder was analyzed with a Spectral Dynamics Real Time Analyzer Model SD301C. The analyzer determined the signal output as a function of frequency. The frequency spectrum was averaged sixteen times; then the average frequency spectrum was plotted. In this way, the frequency content of the "raw" data is known and provided a useful check that the data acquisition system was functioning properly as well as providing a means for gaining insight into the physical situation on-line.

A to D Conversion and Ensemble Averaging

The data were analyzed with an IBM System 7 real-time computer. The system 7 was programmed to perform an ensemble averaging technique. This technique enhances the portion of the signal that is periodic with respect to the syncronization pulse. Each signal, whether from a pressure transducer, anemometer or strain gauge, can be considered to be the sum of a response to the phenomena of interest that is periodic with respect to the rotor period, e.g., the velocity fluctuation due to the rotor wake, plus a signal that is not periodic with respect to the rotor period. The nonperiodic signal could consist of turbulent fluctuations, electronic noise, or a response to events not related to the rotor/stator interaction. Since the Pitrans respond to pressure fluctuations, they not only respond to fluctuations caused by the interaction with the rotor, but also to acoustic noise generated inside and outside of the fan. As discussed later, there is a significant level of acoustic noise in the Pitran output.

Ensemble-averaging consists of pointwise addition of a signal during one rotor period to the signal obtained during the previous rotor period. A signal periodic with the rotor period will have its amplitude doubled, thus preserving the signal, while a random or nonperiodic signal from one period will not correspond pointwise with another period and its sum will tend to diminish. To obtain the periodic signal, the summed value is then divided by the number of sums used. If a sufficiently large number of sums are used, the nonperiodic portion becomes negligible compared to the periodic portion. Figure 20 shows the effect of taking different number of sums of the output of a typical Pitran.

The three channels of data and the once-per-revolution syncronization pulse from the tape recorder were used as the input to system 7. The computer program used had a minimum sampling rate of 500 μ sec. That is, it could digitize a point of the input signal every 500 μ sec. This rate was too low to give sufficient resolution of the signal. To increase the resolution, the tape recorder play-back-speed was halved, from 4.76 cm/s to 0.94 cm/s. The system 7 then digitized and ensembled-average the data channels sequentially, one channel at a time, storing the results from the previous channel then switching to the next channel until the analysis of all three channels was completed. The ensemble-averaged data were then punched on cards.

INSTRUMENT CALIBRATION

Instrumented Stator

Static Calibration

A static calibration was performed to determine the sensitivity of the Pitran transducers. This sensitivity is then used to convert the voltage output of the transducers to a pressure. A schematic representation of the calibration procedure is shown in Figure 21. A known steady-state pressure, determined by a Validyne pressure transducer, was supplied to a test chamber containing the instrumented stator. The reference side of the Pitrans were connected to atmospheric pressure through the bottom wall of the test chamber. The pressure in the test chamber was not constant, but fell slowly with time, indicating a small amount of leakage along the o-ring seal holding the Pitran. The amount of leakage that would occur during a test, with the blade installed in the AFRF, is not believed to have any effect on the Pitran time-dependent output.

The small leakage flow would be vented to atmospheric pressure and should not affect the pressure on the reference side of the Pitran. A photograph of the stator mounted in the test chamber is shown in Figure 22.

The difference in the output of the Pitran before the pressure was applied and after the pressure was applied, and the output of the Validyne were compared to obtain the Pitran calibration constant. This procedure was performed for a range of static pressures and the results found to be repeatable.

The 861 Signal Conditioners were modified per the manufacturers instructions to eliminate the active feedback portion of the circuit that cancelled long term variations in the Pitran output. This permitted the Pitrans to respond to steady static pressure. In this mode, the Pitran output tended to drift. This effect was minimal during the calibration because the Pitran signal was recorded immediately before and after the pressure was applied. The signal drift during this time was negligible.

The data from a typical static calibration are shown in Figure 23.

Dynamic Calibration

The fluid in the tube-cavity system connecting the Pitran to the surface of the instrumented stator, Figure 8, can influence the pressure in the interior cavity due to the fluid friction and inertia. As discussed in greater detail in Appendix A, the pressure in the interior cavity varies in magnitude and phase as a function of tube-cavity geometry, frequency of pressure fluctuations, and fluid properties.

To determine the influence of the tube-cavity arrangement, as well as to determine the Pitran dynamic sensitivity, a dynamic calibration was performed. Sound waves were used as a pressure source. A schematic representation of the calibration set up and instrumentation employed is shown in Figure 24. The amplified output of an oscillator drives a three-way speaker which contains a woofer, mid-range and tweeter speakers with an electrical crossover network that functions to supply the input to the appropriate speaker as a function of frequency. A 0.635 cm Bruel and Kjaer condenser microphone, Type 4136, and the instrumented stator were positioned equidistance, approximately 200 cm, from the speaker in an anechoic chamber. The sound pressure sensed by the microphone was assumed equal to the pressure on the surface of the instrumented stator. This assumption is only valid at frequencies low enough for the pressure increase caused by the reflection of sound waves from the stator blade and microphone to be negligible.

The output of the Pitran with the 861 Signal Conditioner was analyzed with a Spectral Dynamics Corporation model SD301C real time analyzer. The analyzer displayed on an oscilloscope the signal output vs frequency. The output of the Pitran at the frequency of the incident sound waves could be read from the oscilloscope.

Using the microphone calibration (a constant value from 150 to 15,000 Hz per the manufacturers calibration), the microphone output and the output of each Pitran, the sensitivity of each Pitran can be determined as follows:

$$\text{Pitran Sensitivity}\left[\frac{\text{VOLTS}}{\mu\text{ bar}}\right] = \text{Microphone Sensitivity}\left[\frac{\text{VOLTS}}{\mu\text{ bar}}\right] \times \frac{\text{Pitran Output [VOLTS]}}{\text{Microphone Output [VOLTS]}} .$$

As the microphone and the instrumented stator are equidistance from the speaker, the phase meter between the B & K amplifier output and the 861 Signal Conditioner output measures the phase difference between the pressure on the surface on the blade and the pressure in the interior cavity.

Sample calibrations showing Pitran sensitivity and phase angle vs frequency are shown in Figures 25 and 26. The effects of a resonance can be seen. The sensitivities shown for frequencies greater than about 500-600 Hz may not be accurate due to wave reflection effects. The frequency where wave reflection effects become significant are specified in Reference [33] and a correction for the pressure increase on a microphone diaphram caused by the reflection of sound waves is given. A 2 db change in the microphone sensitivity occurs when the incident wavelength is 25% of the microphone diameter. Assuming geometrical similarity, a wavelength of 25% of the stator blade dimension (a square approximately 15 cm on each side) corresponds to a frequency of 550 Hz.

The dynamic Pitran sensitivity at low frequencies agreed well with sensitivity from the static calibration. The measured tube-cavity resonance frequencies are compared with predicted values in Figure 9.

Instrumented Rotor

The sensor portion of the instrumented rotor was statically calibrated by supporting varying masses and recording the strain gauge output. This resulted in a sensitivity to a normal force of 4.198×10^{-3} volts/gm and a sensitivity to a moment of 7.929×10^{-7} volts/dyne cm.

The mechanical resonance of the sensor was also investigated using electromagnetic shakers to apply time varying forces and moments. The segment of the rotor was replaced by a metal bar with a mass and moment of inertia equal to the rotor segment. The dynamic response of the sensor to forces is shown in Figure 27.

Hot-Film Anemometer

The hot-film anemometer was calibrated in a small wind tunnel shown schematically in Figure 28. The wind tunnel consists of a centrifugal fan, connecting ducting, a constricted area test section, a large area expansion section, a heater and associated electrical controls. The hot-film probe is inserted in a probe holder in the constricted test area which also contains a temperature sensor. The velocity in the test section sensed by the hot film is computed by measuring the pressure drop across the inlet nozzle and by determining the density of the flow. The pressure differential Δp between the large area and the constricted area section is sensed by the Validyne pressure transducer and the density is computed from the Perfect Gas Law, knowing the temperature and atmospheric pressure. Atmospheric pressure was measured with a mercury barometer. The calibration consists of recording the hot-film output as a function of velocity. A family of curves for different air temperatures

is obtained by using the heater to raise the air temperature. A typical calibration is shown in Figure 29.

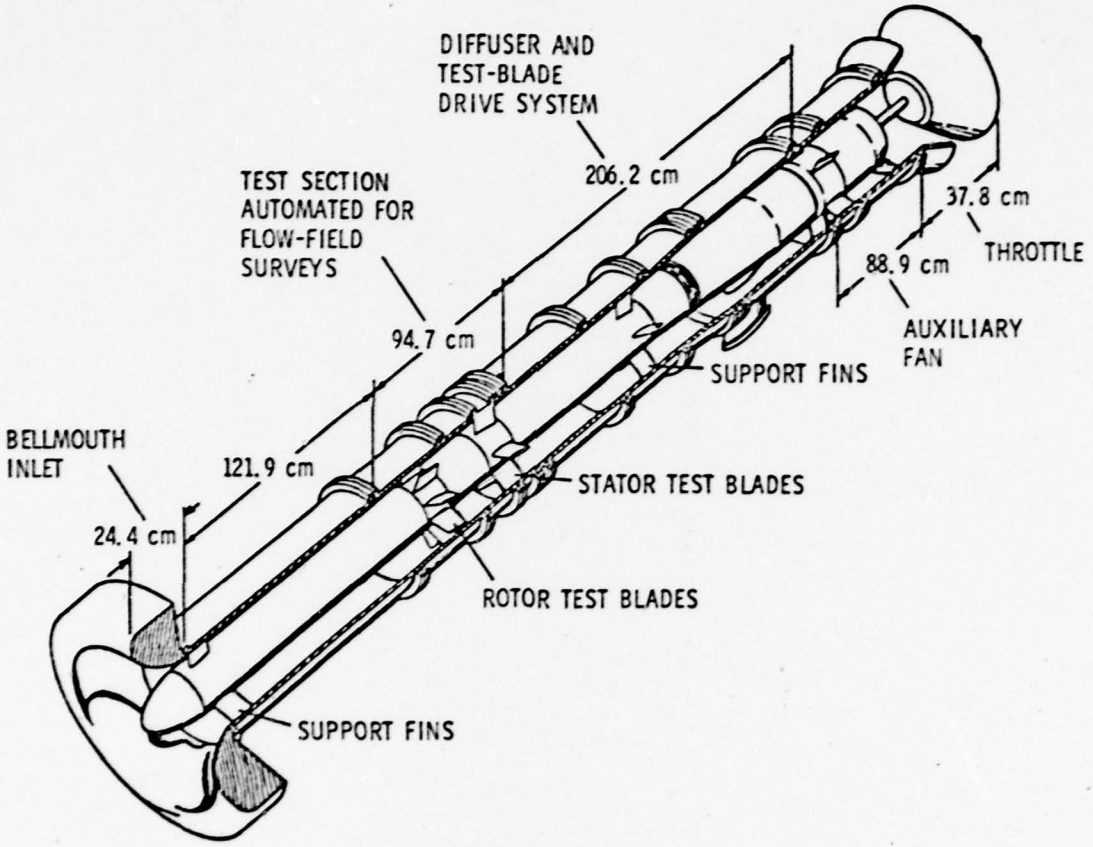


Figure 5 - Axial Flow Research Fan

14 March 1978
REH:GFF:jep

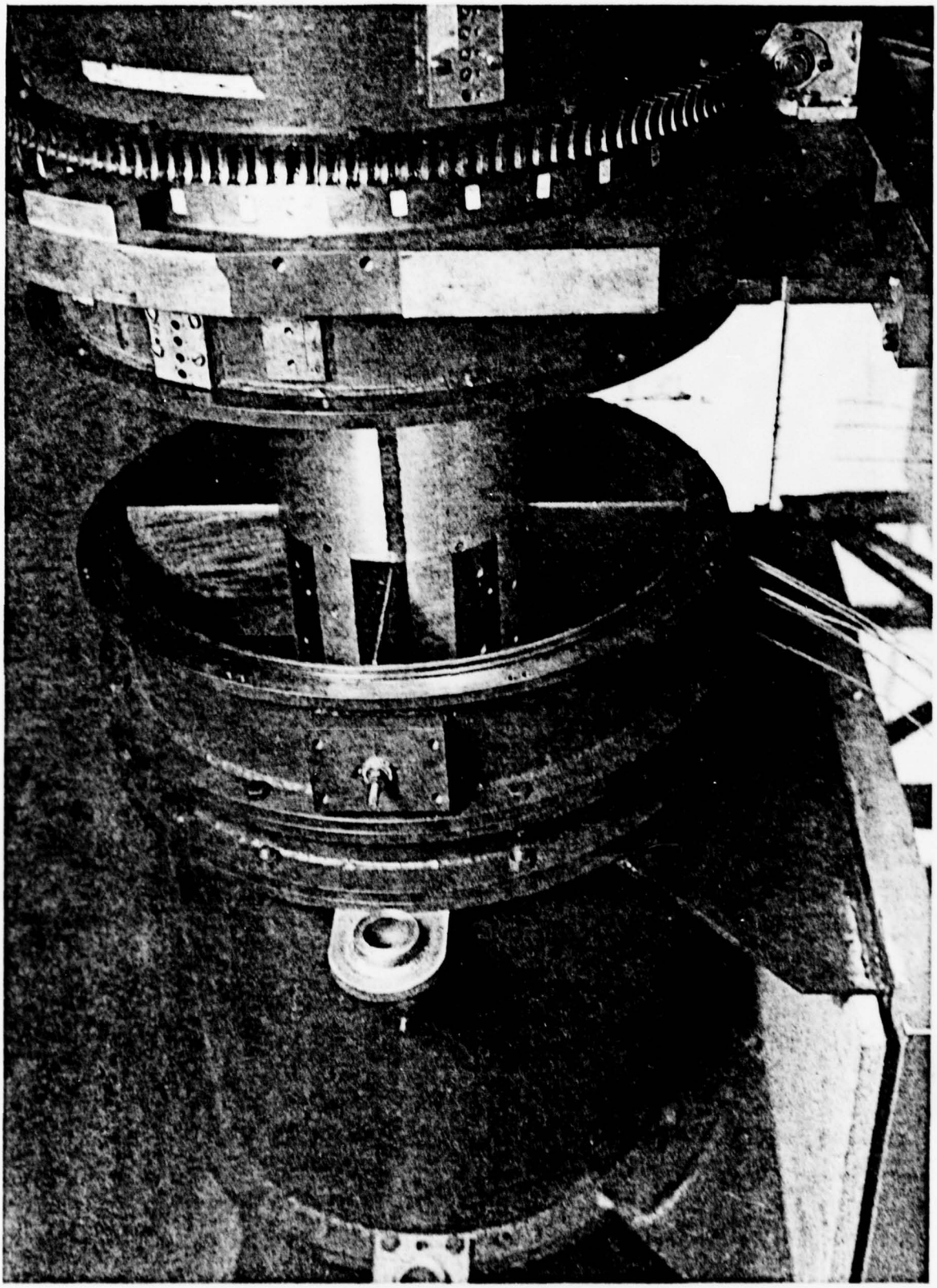


Figure 6 - Installation of Stators in AFRP

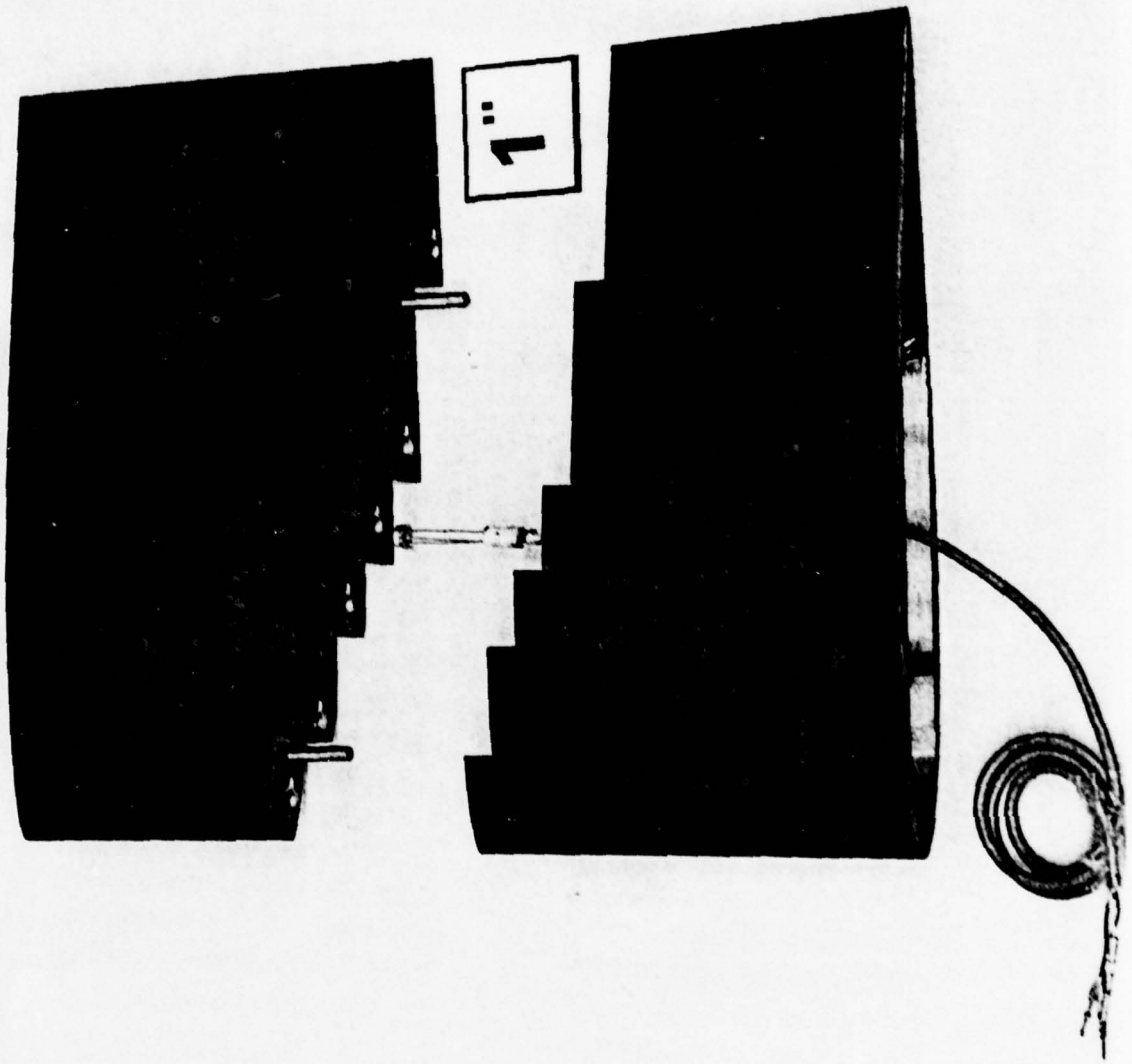


Figure 7 - Instrumented Stator Blade

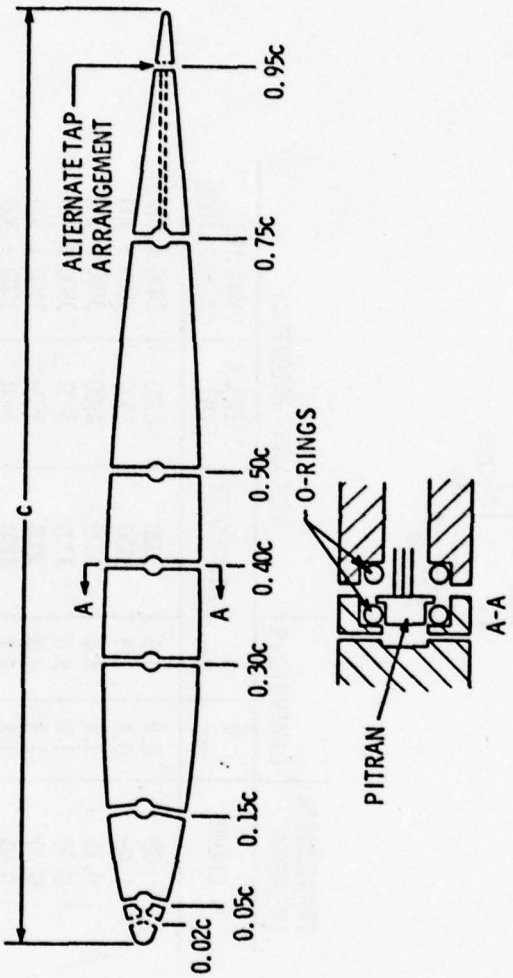
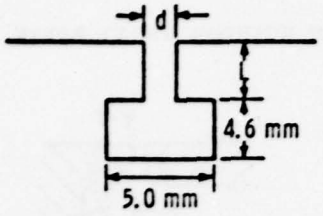


Figure 8 - Instrumented Stator Blade Cross Section and Transducer Mounting Arrangement



TRANSDUCER LOCATION	DIMENSIONS		RESONANT FREQUENCY		
% CHORD	d mm	L mm	HELMHOLTZ	IBERALL [40]	DYNAMIC CALIBRATION
0.02	0.9	0.5	5000	6100	2400 ± 300
0.05	0.9	1.5	3300	3500	3500 ± 300
0.15	1.8	3.8	4200	4900	3500 ± 300
0.30	1.8	5.0	3700	3800	3500 ± 300
0.40	1.8	4.8	3800	3900	3500 ± 300
0.50	1.8	4.1	4100	4300	3500 ± 300
0.75	1.8	1.3	6500	7700	> 5000
0.95	1.2	28.	1100	1000	1100 ± 200

Figure 9 - Dimensions of Transducer Cavities and Predicted Resonant Frequencies

14 March 1978
REH:GFF:jep

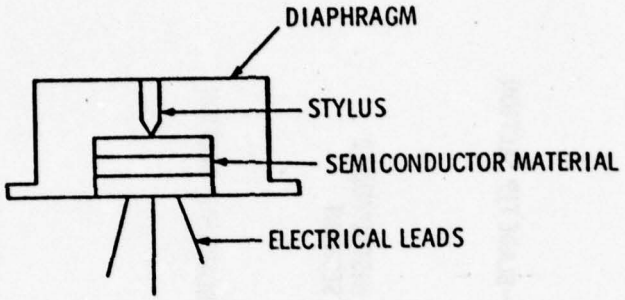


Figure 10 - Schematic of Pitran Transducer

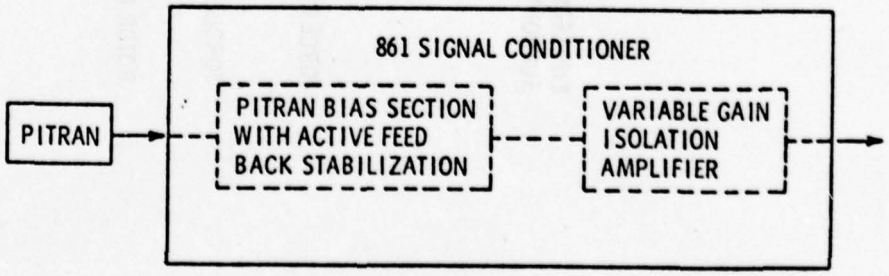


Figure 11 - Pitran Signal Conditioner

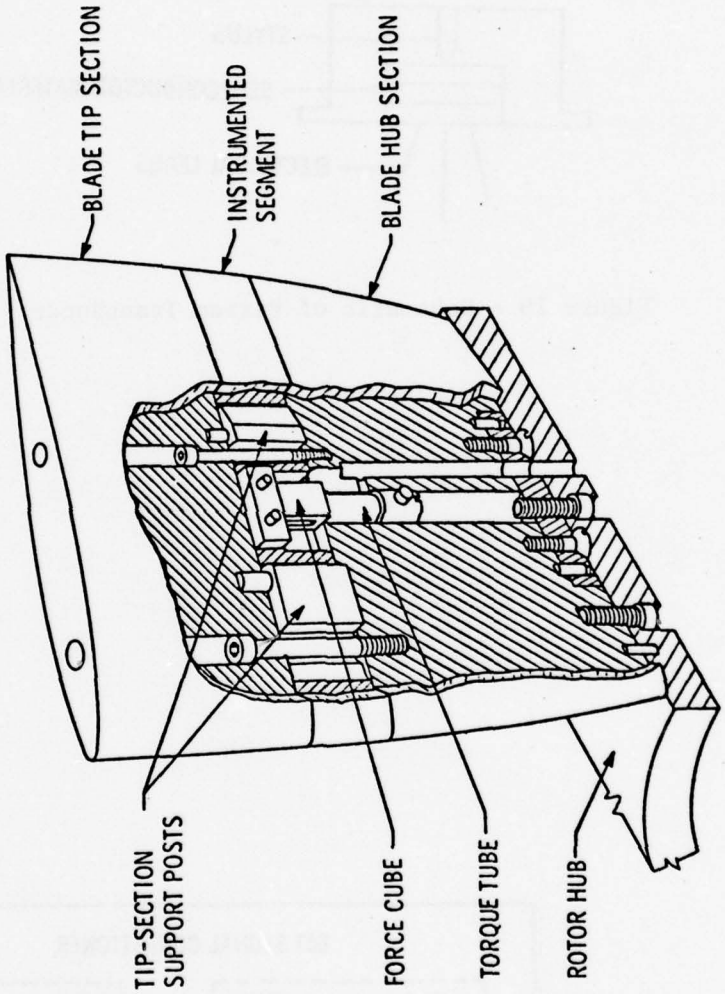


Figure 12 - Instrumented Rotor Blade

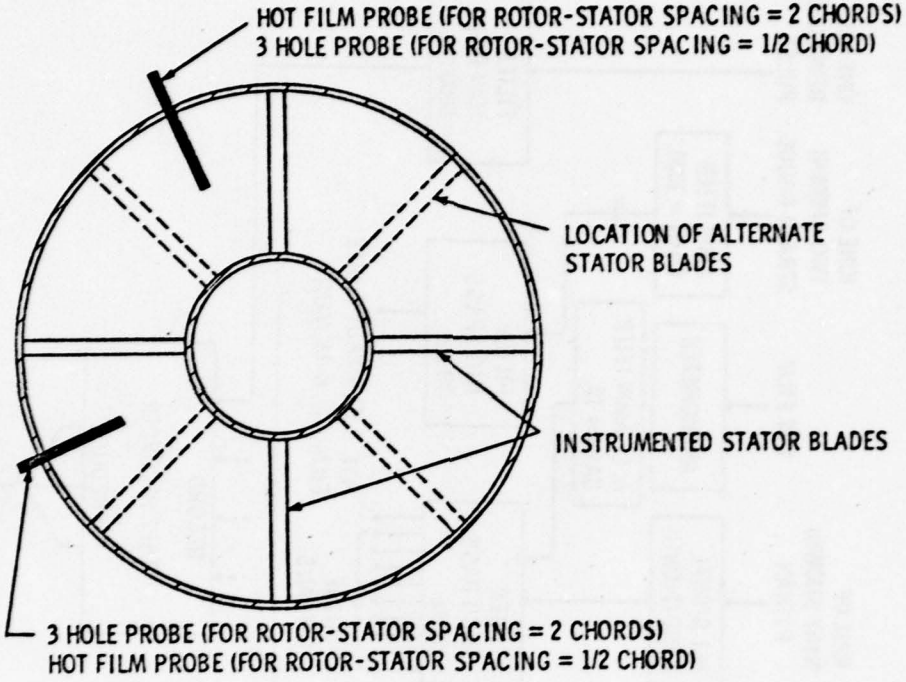


Figure 13 - Circumferential Location of Probes and Instrumented Stators

14 March 1978
REH:GFF:jep

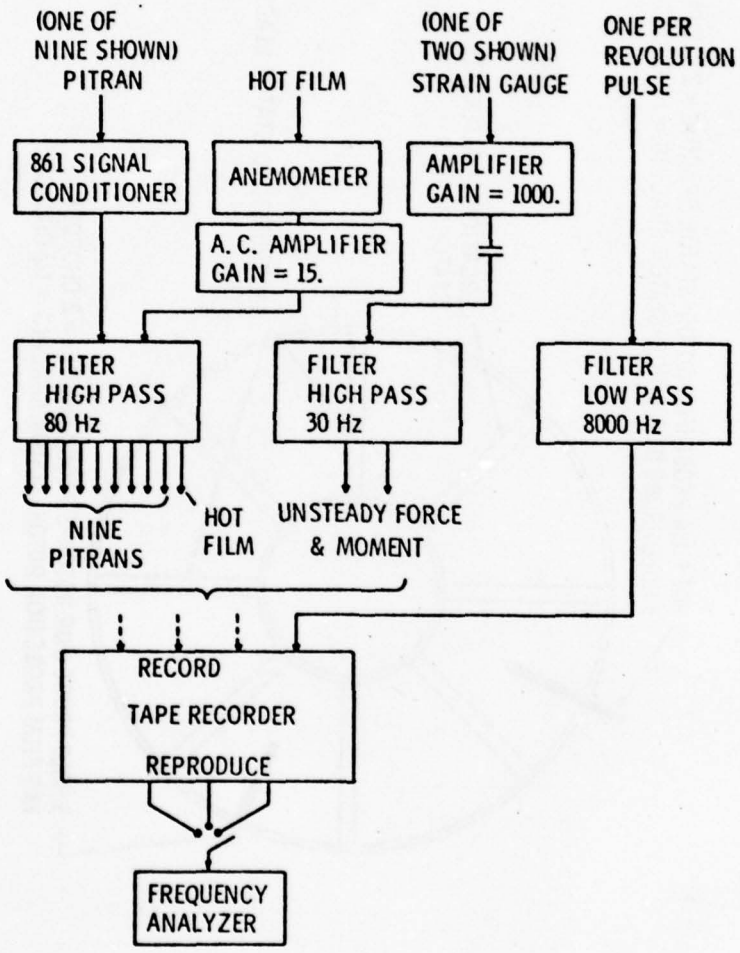


Figure 14 - Instrumentation and Data Acquisition Schematic

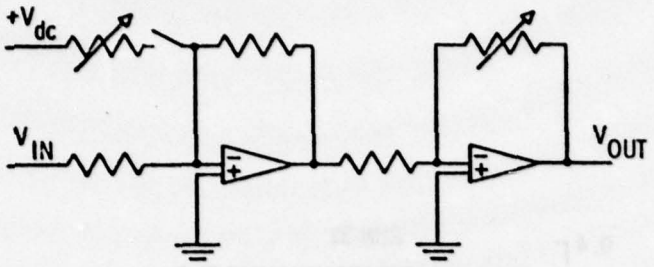


Figure 15 - Schematic of Hot-Film Anemometer Signal Conditioner

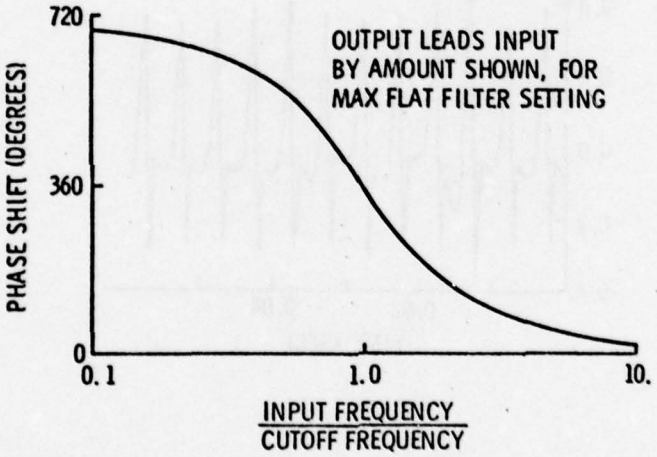


Figure 16 - Phase Shift Introduced by Krohn-Hite Filter

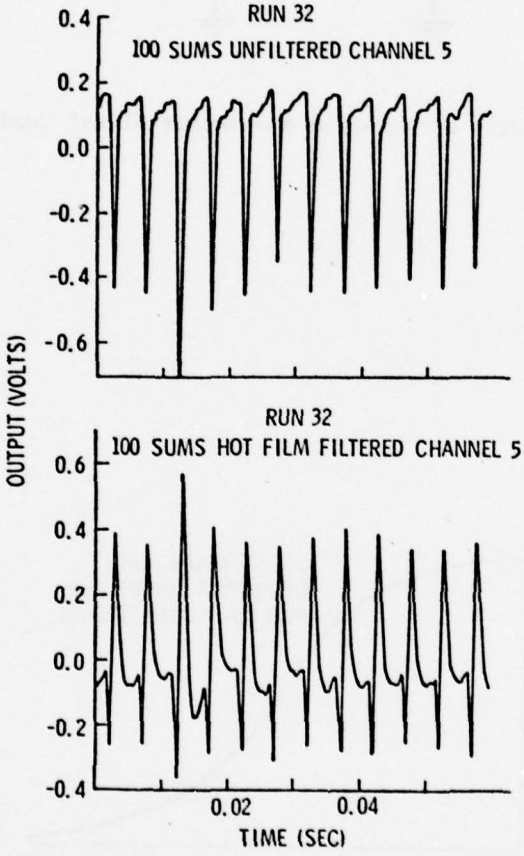


Figure 17 - Unfiltered and Filtered Hot-Film Output

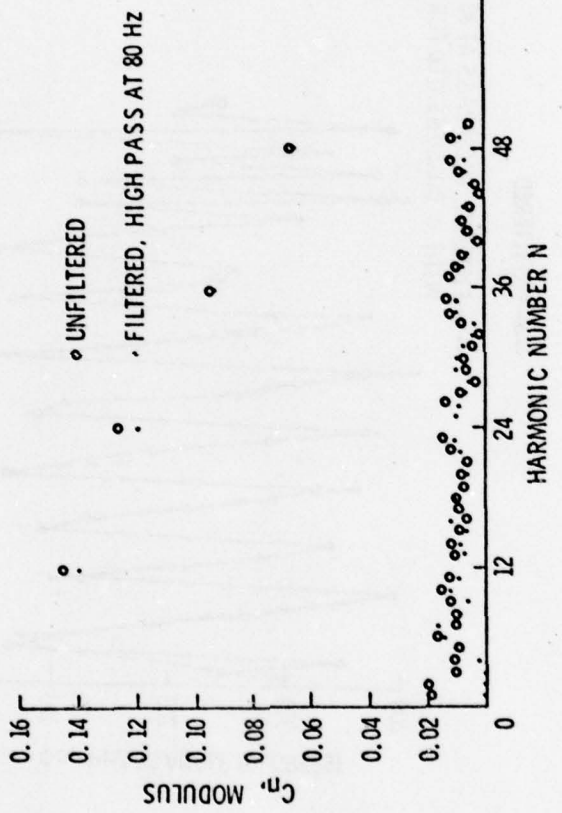


Figure 18 - Comparison of Fourier Modulus of Unfiltered and Corrected Filtered Hot-Film Data

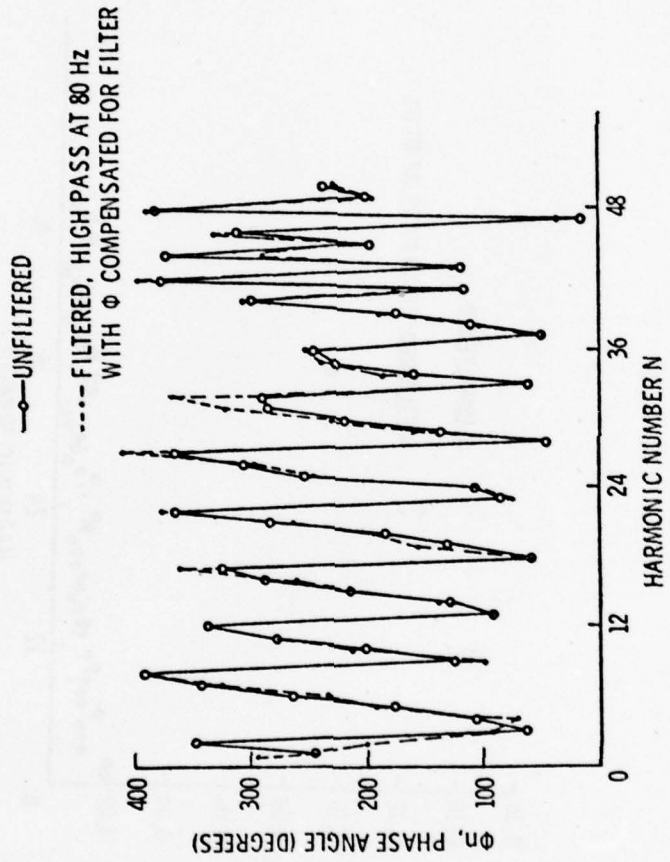


Figure 19 - Comparison of Phase Angle of Unfiltered and Corrected Filtered Hot-Film Data

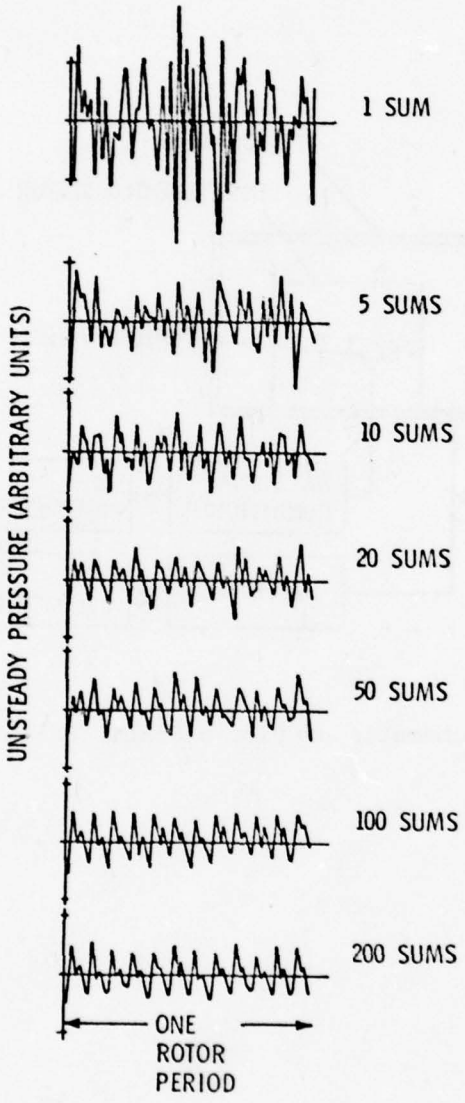


Figure 20 - The Effect of the Number of Ensemble-Averaging Sums on Typical Pitran Output

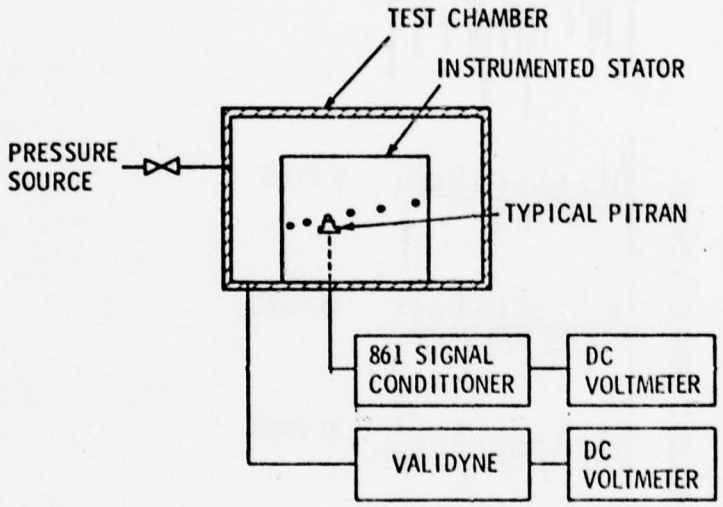


Figure 21 - Schematic of Pitran Static Calibration Setup

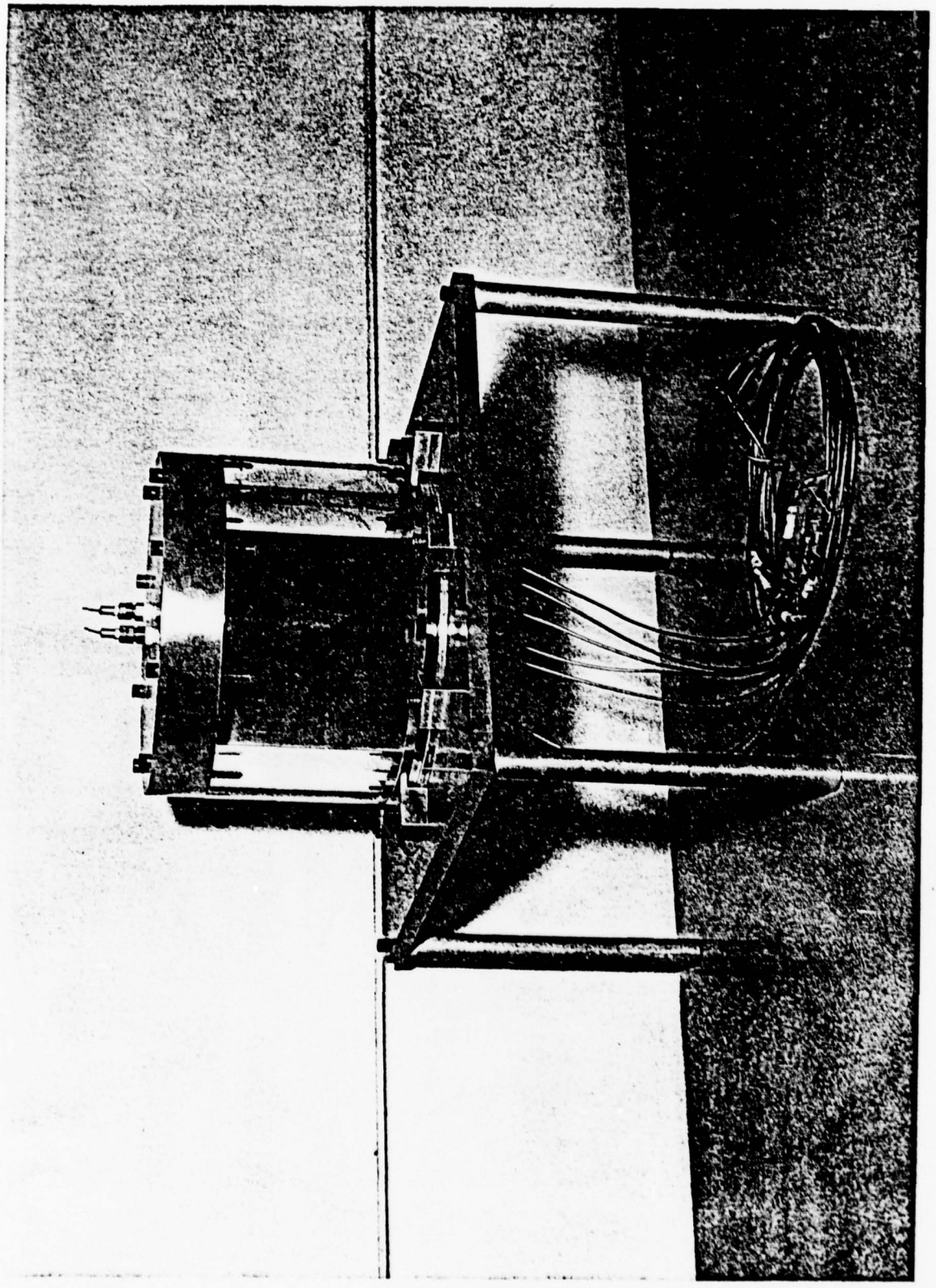


Figure 22 - Pitran Static Calibration Apparatus

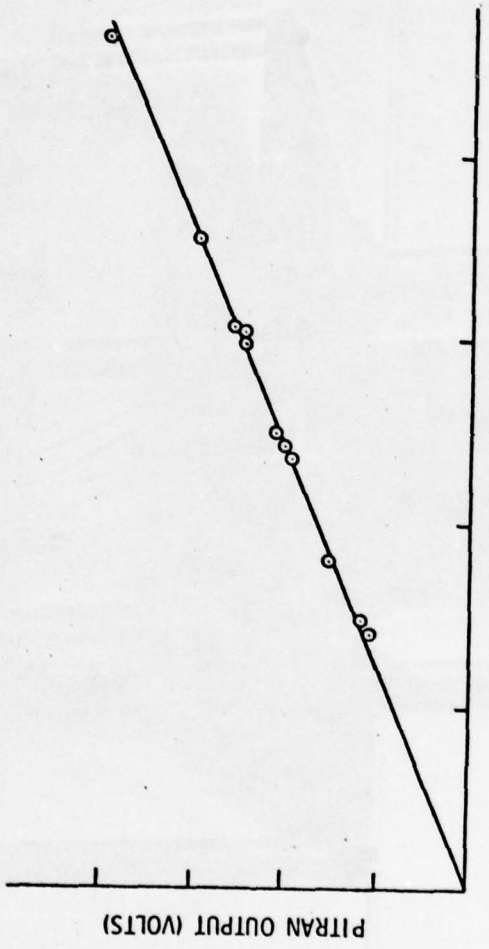


Figure 23 - Typical Pitran Static Calibration Data

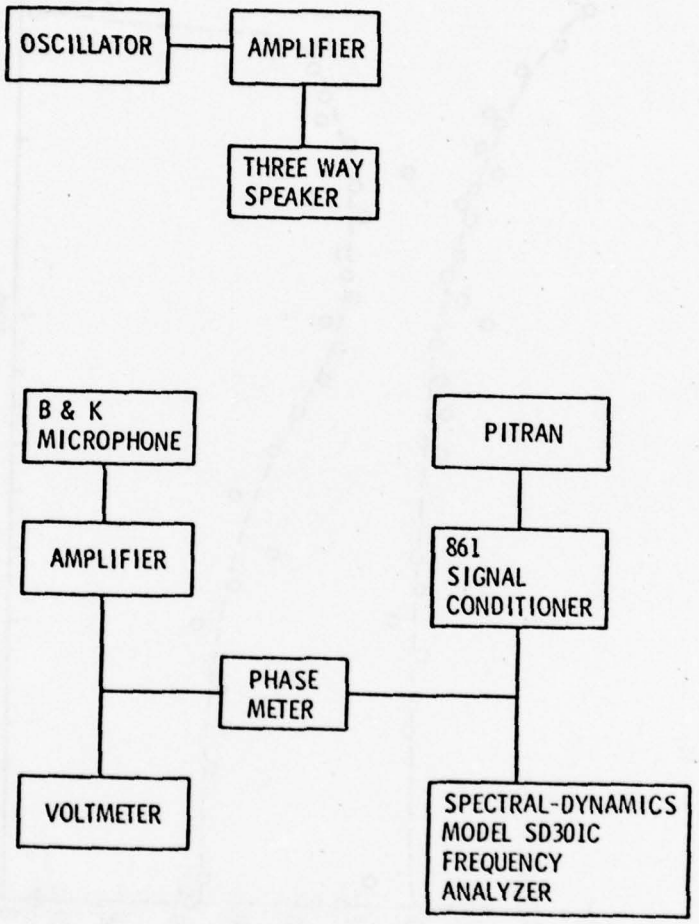


Figure 24 - Schematic of Pitran Dynamic Calibration Setup

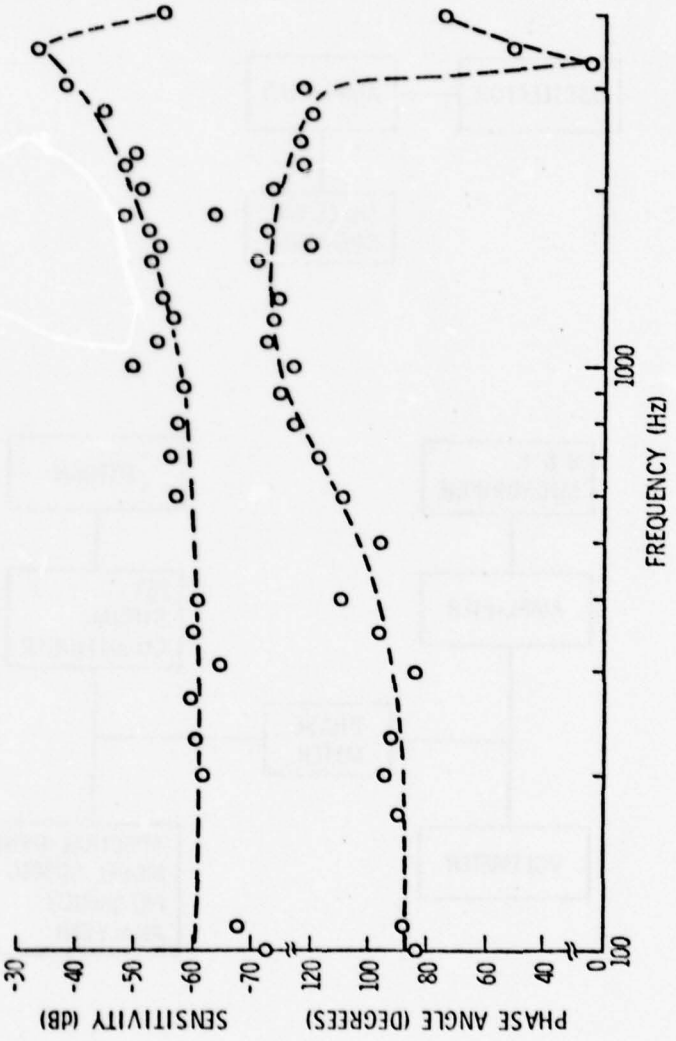


Figure 25 - Results of Dynamic Calibration of Pitran at x/c=0.15

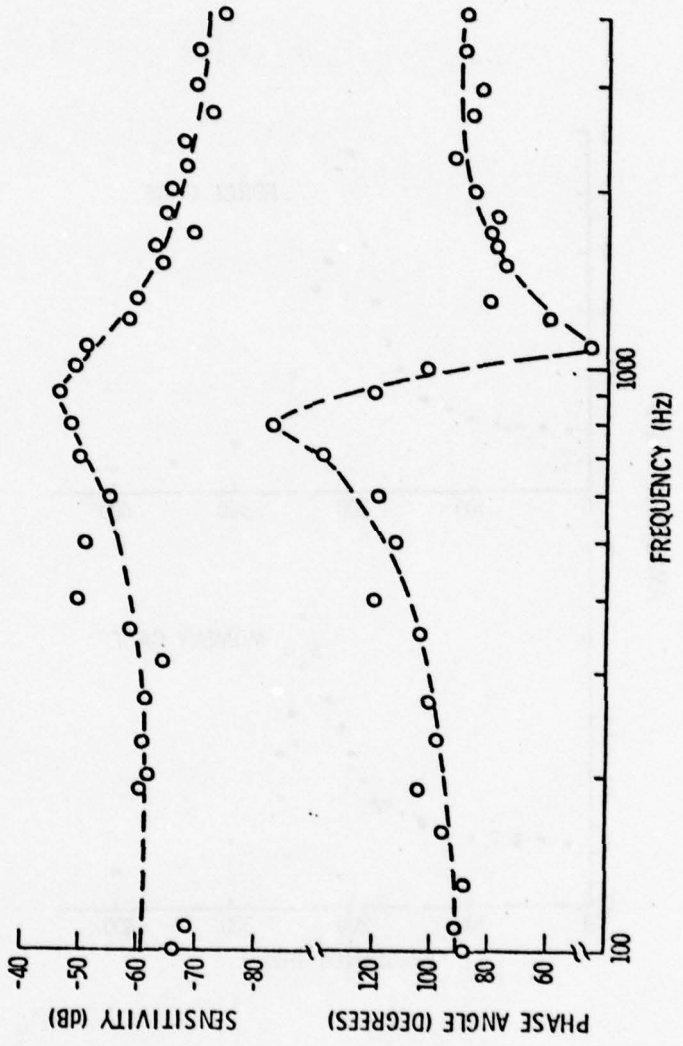


Figure 26 - Results of Dynamic Calibration of Pitran at x/c=0.95

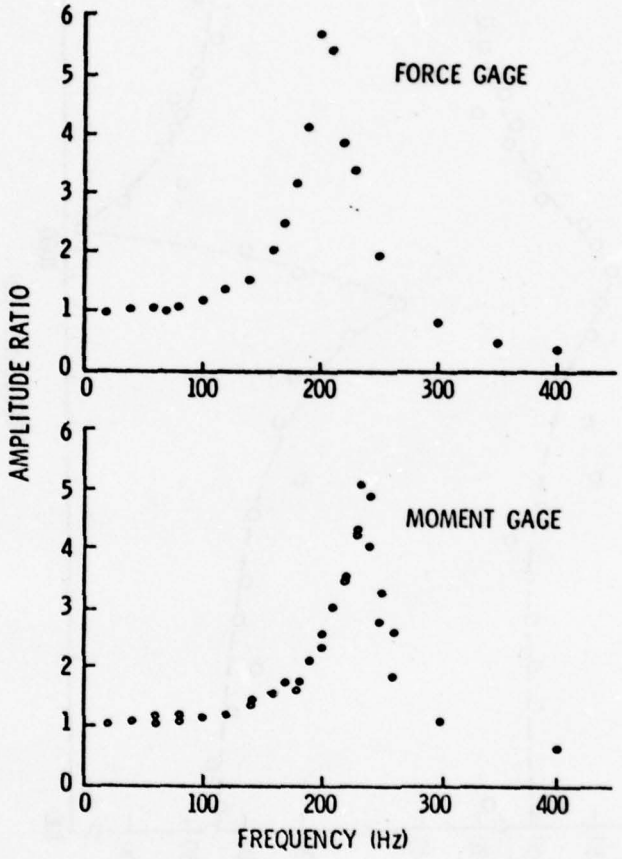


Figure 27 - Dynamic Response of Instrumented Rotor Blade

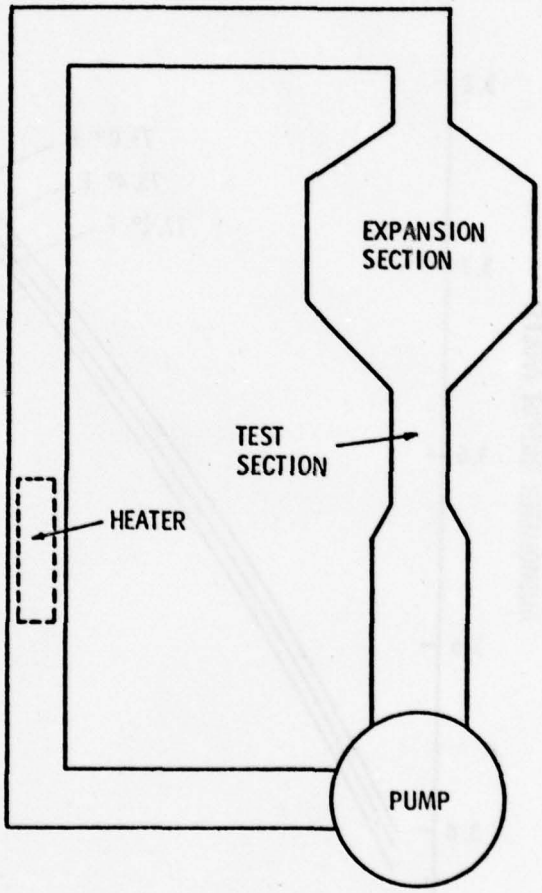


Figure 28 - Schematic of Hot-Film Calibration Tunnel

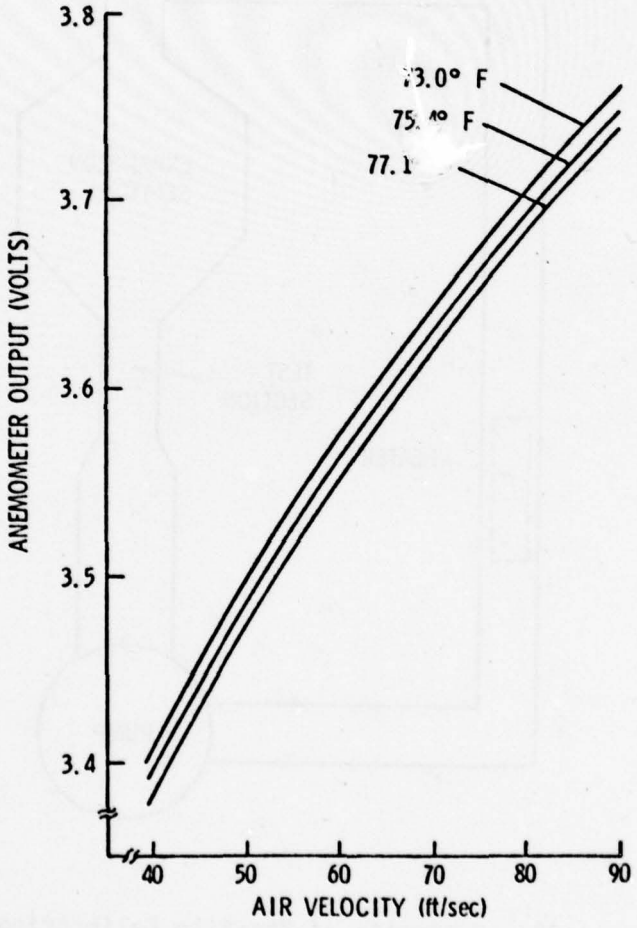


Figure 29 - Typical Hot-Film Calibration Data

PRESENTATION AND DISCUSSION OF EXPERIMENTAL RESULTS

Using the instrumentation described above, measurements were conducted of the wakes shed by the rotor, the unsteady pressures on the stator blades and the unsteady lift and moment on the instrumented rotor blade. These measurements were conducted as a function of stator steady incidence, rotor/stator spacing and stator solidity, or space-to-chord ratio. The test variables were:

stator incidence: - 2, 5, 17 degrees,
rotor/stator spacing: 0.5 and 2.0 rotor chords,
stator solidity: 0.493 and 0.986.

In the following sections the data obtained with each of the different forms of instrumentation employed are presented and discussed.

ROTOR WAKES

The unsteady pressures on the stator blades are generated in this experimental setup, Figure 5, by the interaction of the stator blades and the wakes shed by the upstream rotor. These rotor wakes were measured using a hot-film anemometer as previously described. The anemometer was placed with its sensing element perpendicular to the flow, by first measuring the absolute time-mean flow direction exiting from the rotor with a three-hole wedge probe. With the anemometer so positioned, the velocity variation as a function of time was determined. Knowing the position of the anemometer and the absolute flow angle, it is possible to determine the velocity variation due to the rotor wakes at the leading edge of the instrumented stator blades.

An important element in obtaining these time varying data is to reference the time from a given spatial location as the rotor blades move past the hot-film anemometer. This was accomplished by employing the one-per-revolution pulse from the rotor shaft mounted photoelectric device described above. With this once-per-revolution pulse it is possible to ensemble average the output of the hot-film anemometer to remove the random variations in the flow.

Figures 30 (a) and (b) show the Fourier reconstruction of the ensemble-averaged velocity variations at the instrumented stator leading edge as a function of time for each of the rotor/stator spacings, stator solidities and incidence angles investigated. This velocity is nondimensionalized by the time-mean circumferential averaged velocity which is given by the dc voltage output of the anemometer. Shown in Figure 31 are the wakes for one revolution of the twelve bladed rotor, i.e., between consecutive trigger pulses. The rotor shaft speed (1000 RPM) was identical for stator incidences of -2 and 5 degrees. The RPM was increased to 1428 RPM to obtain the stator incidence condition of 17 degrees as evidenced by the shorter lapsed time for one rotor revolution.

At a rotor/stator spacing of 0.5 rotor chord lengths, Figure 30 (a), the wakes are observed to have a sharper deficit in velocity than observed at a rotor/stator spacing of 2.0. This is caused by the mixing and diffusion of the wake as the distance from the rotor trailing edge is increased. It is also evident that the blades are not all geometrically similar. One blade in particular has a greater velocity defect, which is presumably caused by a slight misalignment of the blade in the rotor hub.

To describe the response of the stator blades to the wakes of the rotor blades, an averaged wake was constructed from those measured in one rotor revolution. This was accomplished by breaking the measurements, Figure 30, into twelve equal time intervals which were then averaged. This effectively gives an average wake defect for describing the response of the stator-blade. This averaged defect will change for each stator incidence angle, and rotor/stator spacing.

Figure 31 shows the frequency analysis of typical hot-film signals performed by the Spectral Dynamics SD301C. The signal can be seen to contain strong responses at rotor blade passing frequency (BPF) and higher multiples of BPF which decreases in magnitude. At a rotor-stator spacing of 2.0, the higher harmonics decrease rapidly such that the third harmonic is approximately 14 dB less than the signal at rotor BPF and fourth harmonic is not visible above background noise. At a rotor-stator spacing of 0.5, the decrease in magnitude of each harmonic is more gradual, for example the fourth harmonic is approximately 10 dB less than the response at rotor BPF.

The wake velocity can be used to calculate the variation of the instantaneous angle of incidence around the time-mean incidence as the wake reaches the leading edge. Figure 32 shows typical variations in the instantaneous angle of incidence during the interaction with a single viscous wake. This single wake was obtained by averaging the wakes experienced over one rotor revolution. This variation will decrease at a rotor/ stator spacing of 2.0 chord length since the wake is diffused and mixed out.

14 March 1978
REH:GFF:jep

UNSTEADY STATOR BLADE PRESSURES

The wakes shed from the upstream rotor blades interact with the downstream stator blades to generate unsteady pressures and lift on the stator blades. Using the instrumented stators previously discussed, measurements were made of the unsteady static pressures on both the suction and pressure sides of the blades. In this experiment the pressure side of the stator was defined as that surface facing the rotor as the rotor moved toward the stator. The suction surface is then the opposite surface. This definition is consistent with the circumferential-mean steady flow which impinges on the pressure surface at a positive value of stator incidence.

The spectral analyses performed by the Spectral Dynamics Model SD301C real-time analyzer were used as a means of assuring that the data acquisition system was functioning properly and as an aide in understanding the nature of the unsteady pressures recorded by the Pitrans. At each chordwise location the signal consists of a broadband background response, presumably from turbulence in the flow, and strong responses at discrete frequencies. These discrete frequencies correspond to the rotor blade passing frequency, it's multiples, and the downstream auxiliary fan blade passing frequency and it's multiples. Figure 33 shows a typical Pitran response in the frequency domain. Also shown is the magnitude of the Fourier coefficients of the same data after being ensemble averaged using 100 sums. Quite striking is the absence of the auxiliary fan blade passing frequency in the ensemble averaged data. Since it is not a harmonic of the rotor period, the ensemble averaging eliminated this response.

As discussed above, these unsteady static pressures were obtained at two values of rotor/stator spacing (0.5 and 2.0 rotor chord lengths), three stator incidences (-2, 5 and 17 degrees), and two stator solidities (0.493 and 0.986). As a result of this large number of variables, there was a considerable volume of data obtained. The presentation of all of these data is prohibitive. Therefore, a presentation will be made of some typical data to demonstrate the type of data obtained and the trends observed. These data will then be summarized to show the effects of the various test variables on the unsteady surface pressures.

One method of presenting these data is to show the variation of static pressure on both the suction and pressure surfaces as a function of time. These measurements were obtained by taping one side of the transducer cavity, Figure 8, closed. The pressures observed are then referenced to the atmospheric pressure, p_{atm}, acting on the back of the transducer. The resulting signals from the Pitran transducers were then ensemble-averaged and converted to a pressure using the calibration constants obtained during the calibration of the Pitrans. These data were nondimensionalized by the fluid mass density, ρ, the time-mean circumferentially averaged velocity at the stator inlet, V, and the maximum defect in the rotor wake, W_{max}. This results in an unsteady pressure coefficient for both the suction and pressure sides of the stator blade. Examples of these data are presented in Figures 34 and 35 for a stator incidence of 2 degrees and Figures 36 and 37 for a stator incidence of 17 degrees. In these figures the time t=0 is referenced to the one-per-revolution pulse. The presented data are for a rotor/stator spacing of 2.0 rotor chords and a stator

solidity, at the mean radius, of 0.986, and show the response of the transducers located at the various chordwise positions. Similar data were obtained for a rotor/stator spacing of 0.5 and a stator solidity of 0.493. These data are similar to those obtained by other investigators, Lefcort [13], Satyanarayana [25], and Ostdiek [34], in that large amplitude variations are observed near the leading edge of the blade which decrease rapidly with distance along the chord.

Large angles of incidence produce much larger pressure amplitude variations on the suction surface near the leading edge than are produced at smaller angles of incidence, Figure 36 versus Figure 34. Furthermore, the pressure coefficient on the suction surface for i=17 degrees at locations aft of the x/c=0.05 position shows some degree of flattening near the pressure peaks. This type of response resembles those obtained by Satyanarayana [25] for a fixed cascade and by Carter and St. Hilaire [35] on an oscillating airfoil. In both cases this flattening is attributed to local flow separation. However, a more detailed experimental study is necessary to precisely pinpoint the existence of separation.

An alternative method for viewing the pressure fluctuations is to expand the time axis to encompass the time required for the passage of a single wake across the blades. This period of time can be computed from a knowledge of the velocity over the stator and the stator chord length. At $T'_o = -1.0$, the wake centerline is at the blade leading edge; when $T'_o = 1.0$ the centerline is at the trailing edge. During the time required for the passage of a single

rotor wake over the blade, a second wake interacts with the blade. Thus, two wakes are lying on the stator blade at once.

A composite of the variation of the unsteady pressure coefficient as a function of the nondimensional time T'_o is shown in Figures 38, 39 and 40. These plots permit the examination of the variation of the suction and pressure surface pressure coefficients as a function of chordwise position, time, and incidence angle for rotor/stator spacing of 2.0 and a solidity of 0.986.

One significant feature of these data is shown in Figure 40. There is an obvious phase shift in the pressure on the suction surface between locations x/c=0.02 and x/c=0.05 when the stator blade was operated at 17.0 degrees of incidence. The results of the Fourier analysis can be used to quantify such phase shift observations. Each pressure signal is decomposed into the form

$$\tilde{p}(t) = \sum_{N=1}^{\infty} C_N \cos (Nt - \phi_N) \quad ,$$

where one period of the signal (360°) is defined as one rotor revolution. Thus, N=12 is the first harmonic of the blade passing frequency, and N=24 is the second harmonic of blade passing frequency. The phase angle of the unsteady pressures on the suction and pressure surfaces of the blade are presented in Figures 41 through 44 as a function of x/c for different values of rotor/stator spacing, solidity and incidence angle. These phase angles are referenced to the signal from the once-per-revolution timing signal. Thus, these data indicate the relative behavior of the pressures on the suction and pressure sides of the blade.

They do not, however, indicate the absolute value of the phase angle of the pressure fluctuations with respect to the wake as it interacts with the blade.

Of major interest in these data is the observation that the phase angle is nearly constant on the pressure surface of the blade, while it undergoes significant changes on the suction surface. This behavior is similar to that observed by Satyanarayana [25] for a cascade of airfoils operated in a sinusoidal low frequency, nonconvected disturbance flow. However, the variations observed by Satyanarayana were continuous compared to the erratic behavior observed in these tests. Further, Satyanarayana showed his variations in phase angle to be a function of the stagger angle of the blade. Since the stagger angle is zero in the subject tests, it is suspected that these large variations in phase angle are associated with local flow separation. This is supported by the fact that at -2.0 degrees incidence the variations of phase angle are much less than at 17.0 degrees incidence.

The phase angle ϕ for N=12 and N=24 can be used to compute the difference in phase angle between the pressure and suction surfaces of the blade. This phase angle difference, defined as

$$\phi_N(\text{suction}) - \phi_N(\text{pressure}) \quad ,$$

is shown in Figures 45 and 46 as a function of incidence angle at constant values of x/c. Considering the response when N=12, this phase angle difference exhibits a definite trend with incidence angle in which the phase angle difference decreases with increasing

incidence angle. This means that the pressure fluctuations on the suction and pressure surface are tending toward a condition where they are in phase with each other.

At a stator incidence of -2 degrees, the phase angle difference is near 180 degrees for locations nearer the leading edge. At stator incidence of 5 degrees, phase angle difference deviations from 180 degrees become more apparent, especially at x/c=0.15. Finally, a stator at incidence of 17 degrees, the phase angle difference differs from 180 degrees by a larger amount, with large variations between positions along the blade. At R/S=2 and a solidity of 0.986, for example, ϕ_{12}(suction)-ϕ_{12}(pressure)=3 degrees at x/c=0.15 indicating that the pressures on opposite sides of the blade are nearly in phase. The phase angle between the suction and pressure surfaces for N=24, two times blade passing frequency, exhibits the same trends as the phase angle as when N=12.

As shown in Figure 45 and 46, the phase angle difference consistently decreases with increasing incidence and also decreases with distance from the leading edge. While it is not plotted in Figures 45 and 46, examination of Figures 41 through 44 indicates that the phase angle difference between the suction and pressure surfaces approaches zero at the trailing edge for some geometrical configurations. This demonstrates the manner in which the Kutta condition that the pressure difference at the trailing edge, $\Delta p(TE)=0$, is satisfied. If the pressures on the suction and pressure surfaces are in phase, then a pressure can exist on both surfaces but their difference is zero. On the other hand, if the pressures are 180 degrees out of phase the pressure on each surface

must be zero for the Kutta condition to hold. Theoretical models predict that this latter approach is realized.

Figure 47 shows the change which occurs in phase angle between x/c=0.02 and x/c=0.05 and 0.15 for the suction side of the blade as a function of incidence angle. A clear trend with incidence is observed; the pressures are in phase for an incidence of -2 degrees and becoming increasingly out of phase as the incidence increases. For an incidence of 17 degrees, the phase shift between x/c=0.02 and x/c=0.05 is nearly 180 degrees at a solidity of 0.986, but is quite small at solidity = 0.493. The phase shift between x/c=0.02 and x/c=0.15 is not appreciably affected by solidity. There are no apparent effects due to rotor/stator spacing.

Because of the large number of variables in this test program, it is necessary to summarize the response of the stator blades to these variables. Since the pressure traces described above indicate that the major contribution of the wakes to the unsteady pressure on the stator occurs at the leading edge of the blades, those variations at x/c=0.02 have been used to characterize the behavior of the entire blade. The trend of the unsteady pressures at x/c=0.05 and 0.15 are similar.

Rather than considering the variation of pressure on each surface, the difference in pressure between the suction and pressure surfaces is used. This quantity is related to the magnitude of the unsteady lift, or the pressure dipole, at the blade leading edge. Since the phase angles of the pressures on the suction and pressure surfaces are known from the Fourier analysis, the instantaneous peak-to-peak pressure difference can be computed. Thus,

a pressure coefficient, $C_{p_{rms}}$, is defined as:

$$C_{p_{rms}} = \frac{\Delta P_{rms}}{\rho W_{max} V} = \frac{0.707}{\rho W_{max} V} \left\{ \frac{1}{2} (\tilde{p}_{suction} - \tilde{p}_{pressure})_{peak\text{-}to\text{-}peak} \right\} \quad . \quad (1)$$

Figures 48, 49, 50 and 51 present the variation of $C_{p_{rms}}$ as a function of rotor/stator spacing, solidity, incidence angle and chordwise location, respectively. As previously mentioned, the unsteady pressure response decreases rapidly with location along the chord. At x/c=0.15, $C_{p_{rms}}$ is generally about 1/4 the value of $C_{p_{rms}}$ at x/c=0.02. The following discussions are based on the trends of $C_{p_{rms}}$ at x/c=0.02. These data indicate that a major effect on $C_{p_{rms}}$ is due to the solidity of the stator blade row. For example, at a low stator solidity, σ=0.493, there is little effect of incidence angle and rotor/stator spacing on $C_{p_{rms}}$. However, at σ=0.986, there are large effects, particularly at high values of incidence. These data should be considered with caution, however, since only two values of rotor/stator spacing and solidity were evaluated. The data do indicate trends, however. Further, there is a significant increase in $C_{p_{rms}}$ at 17 degrees incidence for a solidity of 0.986. There appears to be a trend with incidence, Figure 50, which indicates a positive value of incidence angle at a minimum value of $C_{p_{rms}}$ is experienced. This effect is similar to that observed both experimentally and analytically with the unsteady lift on a cascade [36] for values of incidence less than 8 degrees. In this case, the unsteady lift decreases with positive incidence due to the existance of a chordwise component of the disturbance velocity. The increase in $C_{p_{rms}}$ at an incidence of

17 degrees is due to the fact that only the pressure at the leading edge (x/c=0.02) is being shown. At other chordwise positions the unsteady pressure and presumably the unsteady lift is greatly reduced.

UNSTEADY ROTOR LIFT

The potential interaction between the moving rotor blades and the stationary stator blades generates an unsteady force and moment on each blade row. Using the instrumented rotor blade discussed above, measurements of the rotor unsteady lift and moment were made. The test variables were identical to those in previously described measurements of the unsteady pressures on the stator blades. Measurements of the unsteady lift and moment were first made in the absence of unsteady potential flow effects by operating the rotor with the stator blades removed. In this condition, the output from the strain gauge instrumented rotor would correspond to: structural vibration, viscous wakes from three center shaft support struts located far upstream of the rotor, turbulence in the rotor inflow and any unsteadiness or steady circumferential flow distortion in the supposed uniform inlet flow. These data are used as a background reference, to be subtracted from data measured with the stator blades installed thus establishing potential flow interactions.

All of the unsteady lift and moment data were ensemble averaged using 100 sums and then Fourier analyzed. The strongest potential interaction would be obtained with the smallest rotor/stator spacing and highest steady loading [5]. The magnitude of the Fourier coefficients of the unsteady lift, or normal force for this

condition (rotor/stator spacing of 0.5 and stator incidence of 17 degrees) and the coefficients of the background are shown in Figure 52. These coefficients are shown as the gauge output voltage; the sensitivity of the gauge (static as well as dynamic characteristics) has not been included to give a force level. The magnitude of the 4th coefficient, with four stator blades installed and the magnitude of the 8th coefficient with 8 stators installed are only slightly larger than the background levels. The magnitude of other coefficients, such as the 12th, are sometimes greater than, sometimes less than the background. This indicates the magnitude of the unsteady lift, and similarly the unsteady moment, is not sufficient to be resolved from the background. The magnitude of the unsteady lift and moment at other rotor/stator spacings and incidence was also too small to be meaningfully measured.

These data indicate that the potential interaction is very small and indeed, negligible as compared with the unsteady interactions caused by wake interactions. This is based on the fact that this strain gauge system has successfully measured the unsteady lift and moment in a spatially varying inflow [29].

14 March 1978
REH:GFF:jep

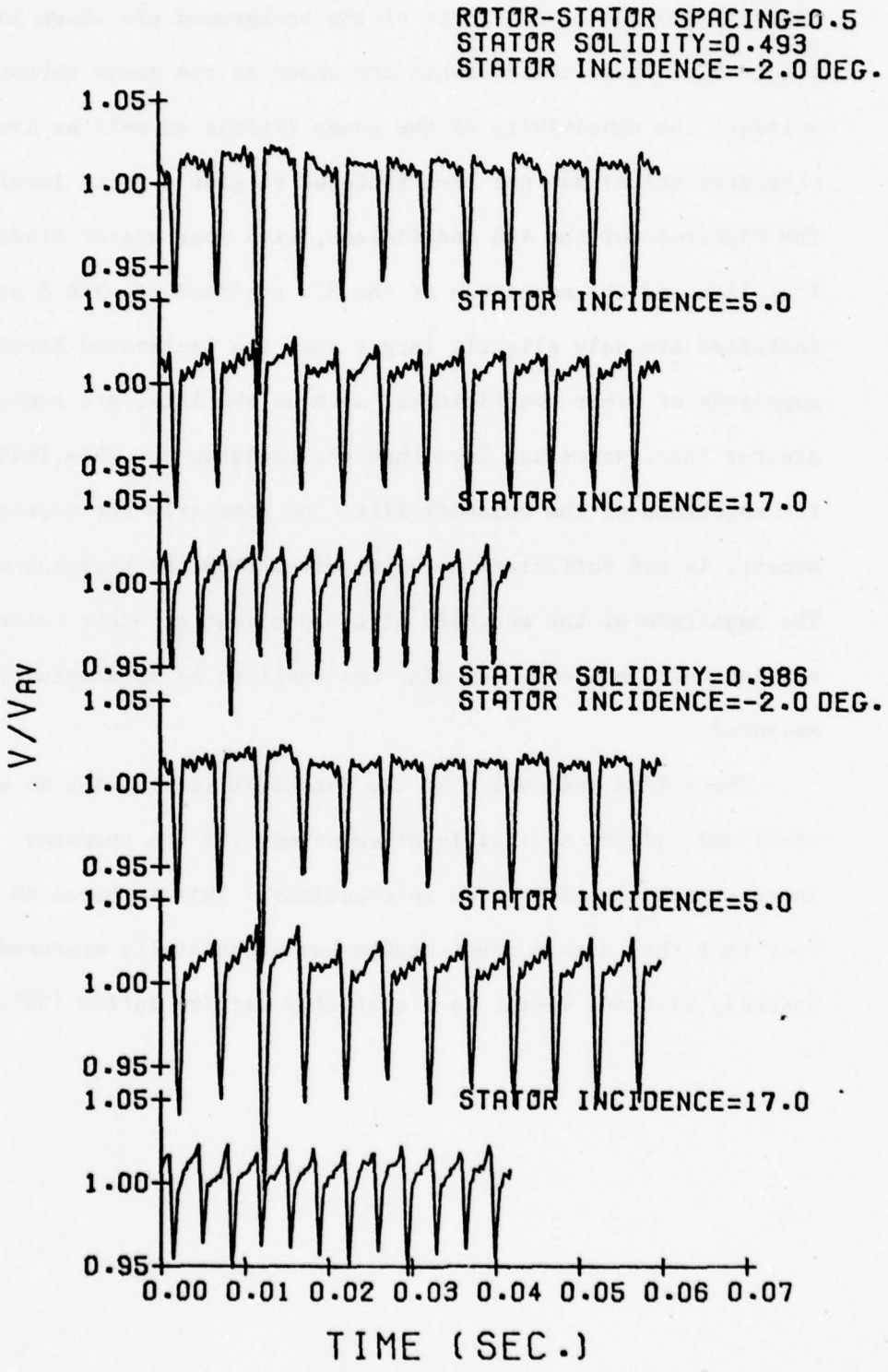


Figure 30 (a) - Rotor Wake at the Stator Leading Edge

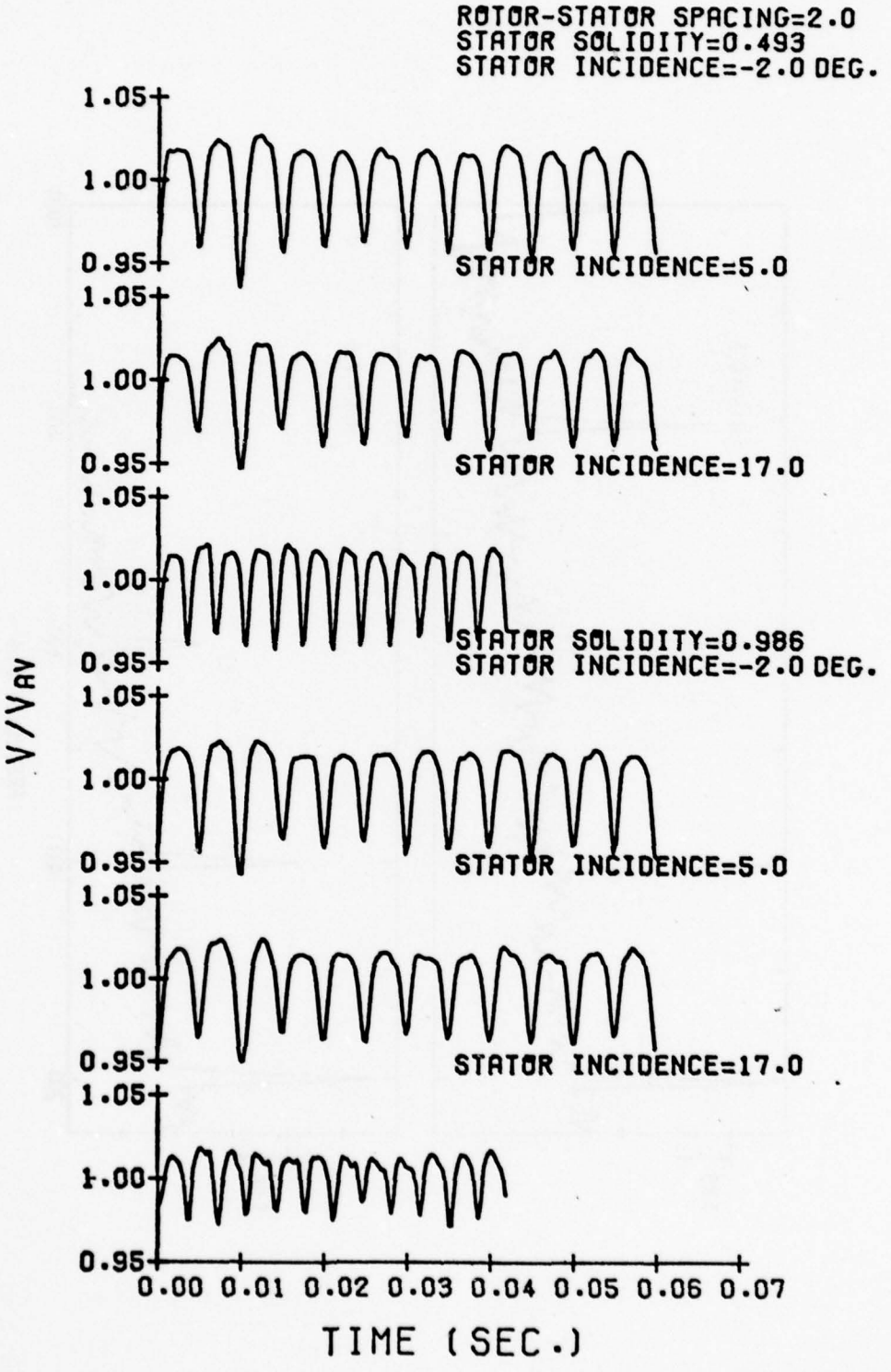


Figure 30 (b) - Rotor Wake at the Stator Leading Edge

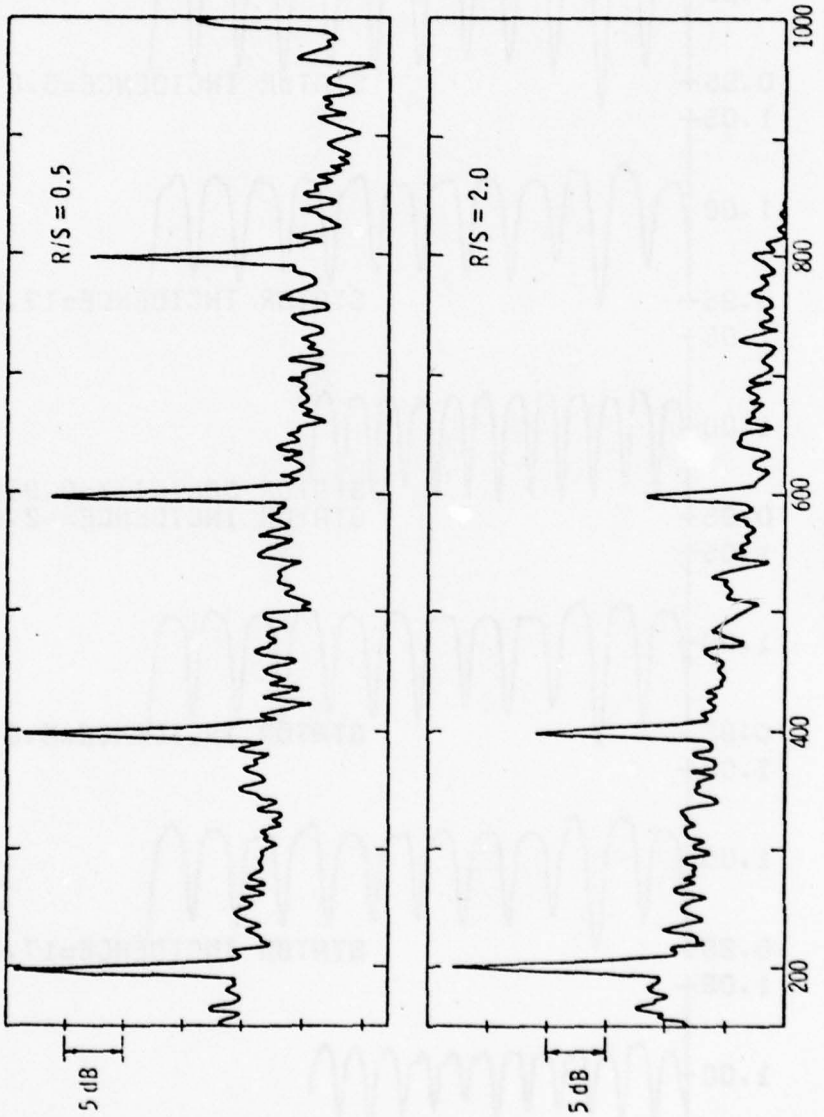


Figure 31 - Spectral Analysis of Typical Hot-Film Output

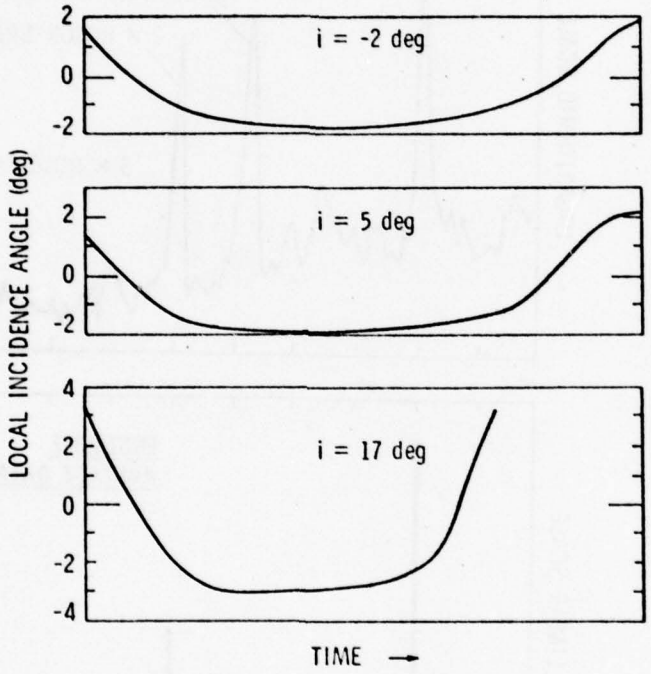


Figure 32 - Variation of Instantaneous Angle of Incidence About Time-Mean Incidence Angle, R/S=0.5

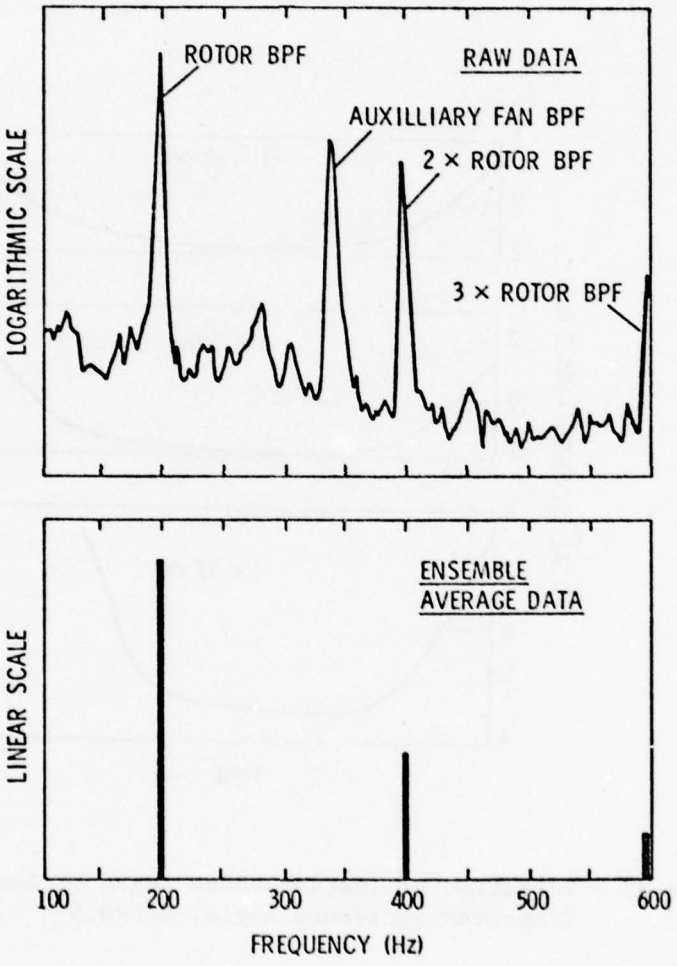


Figure 33 - Typical Spectral Representation of Pitran Output

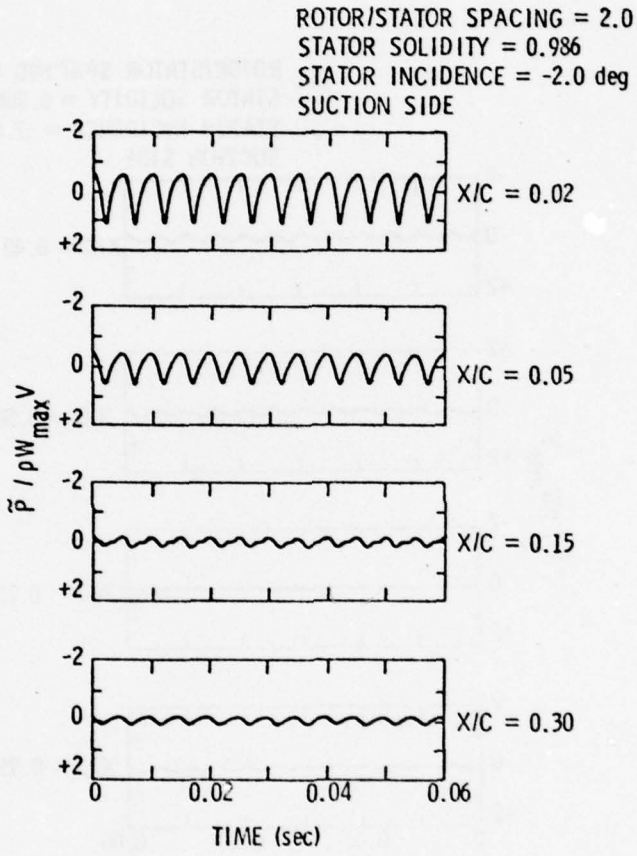


Figure 34 - Unsteady Pressure Coefficient versus Real Time-Suction Surface, i = -2.0 deg

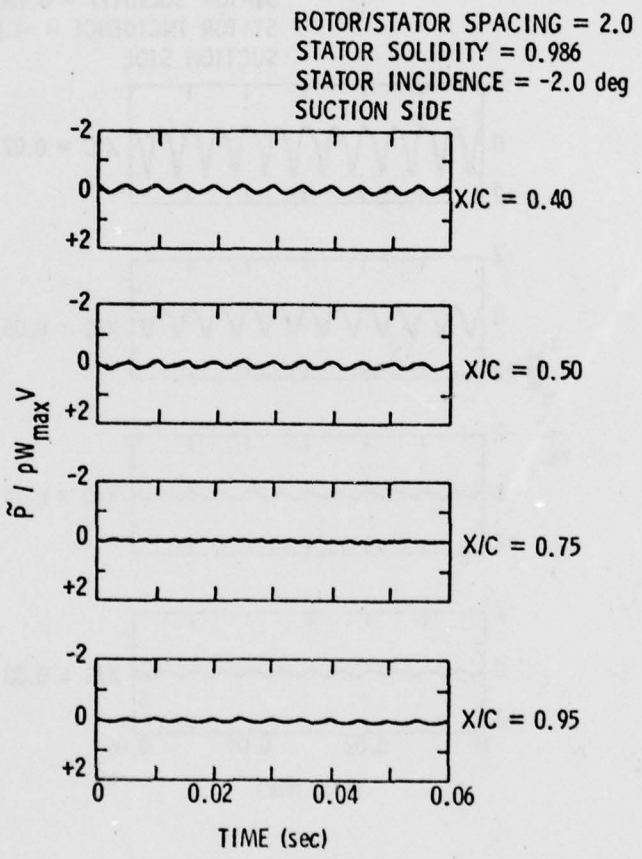


Figure 34 (Cont.)

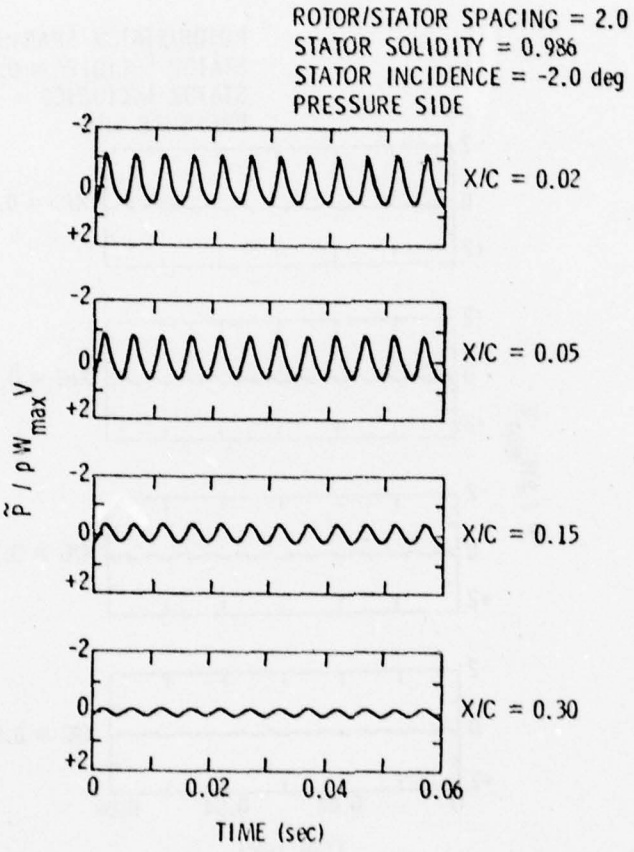


Figure 35 - Unsteady Pressure Coefficient versus Real Time-Pressure Surface, i = -2.0 deg

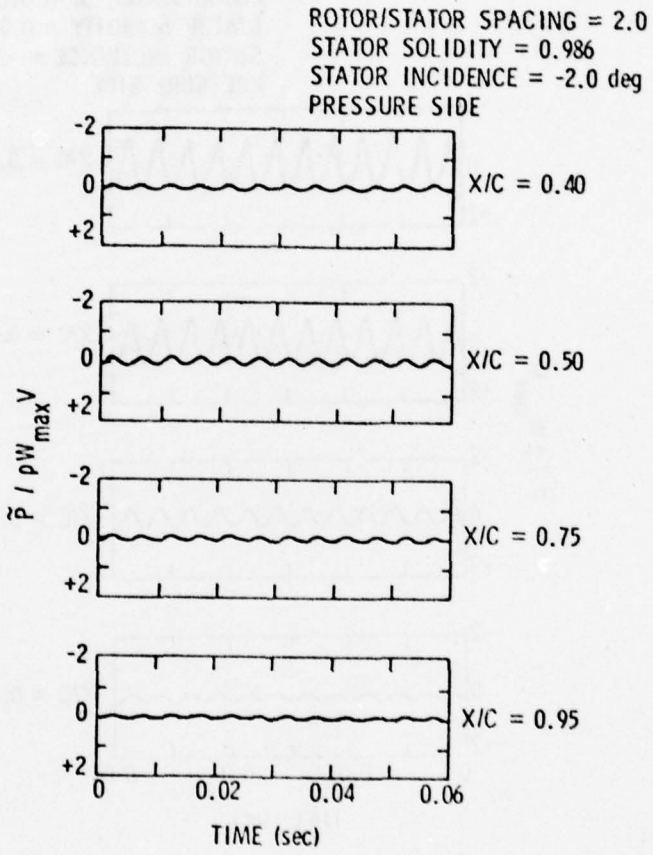


Figure 35 (Cont.)

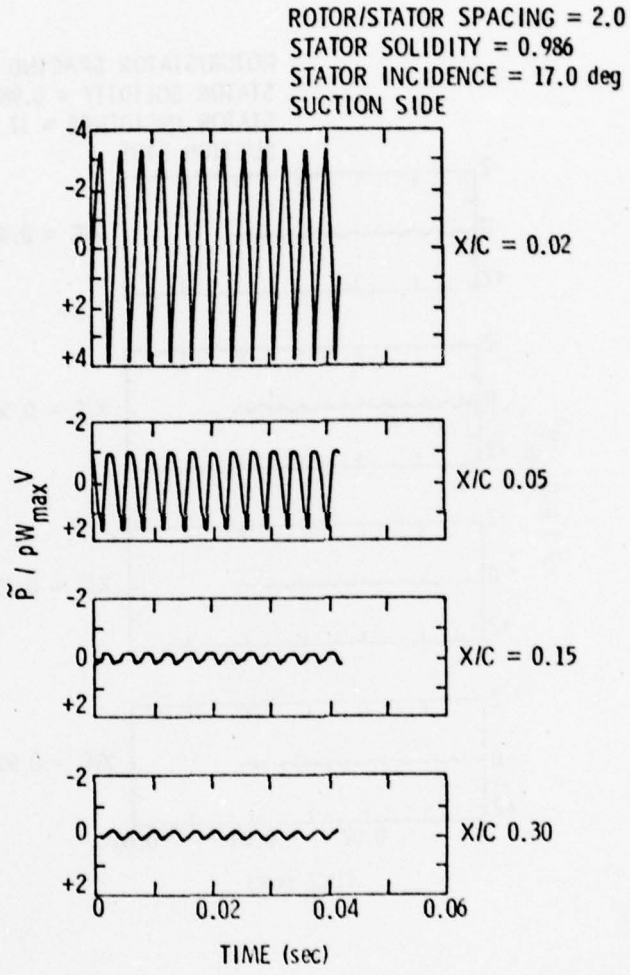


Figure 36 - Unsteady Pressure Coefficient versus Real Time-Suction Surface, i = 17.0 deg

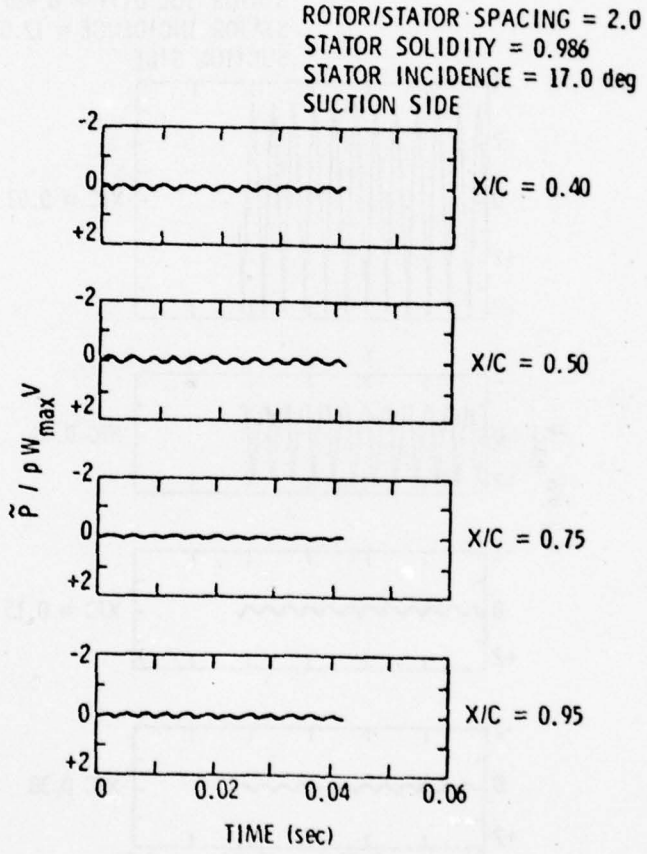


Figure 36 (Cont.)

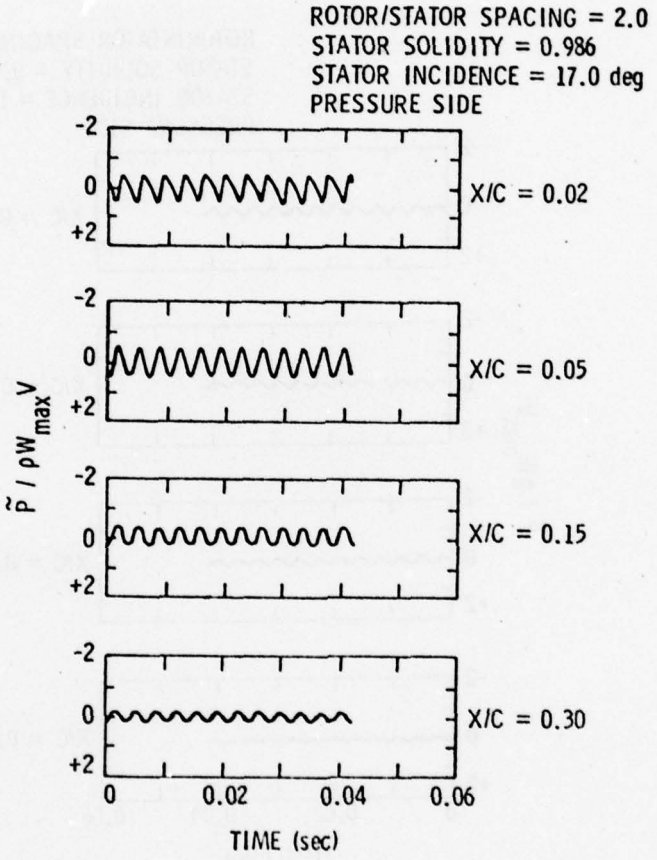


Figure 37 - Unsteady Pressure Coefficient versus Real Time-Pressure Surface, i = 17.0 deg

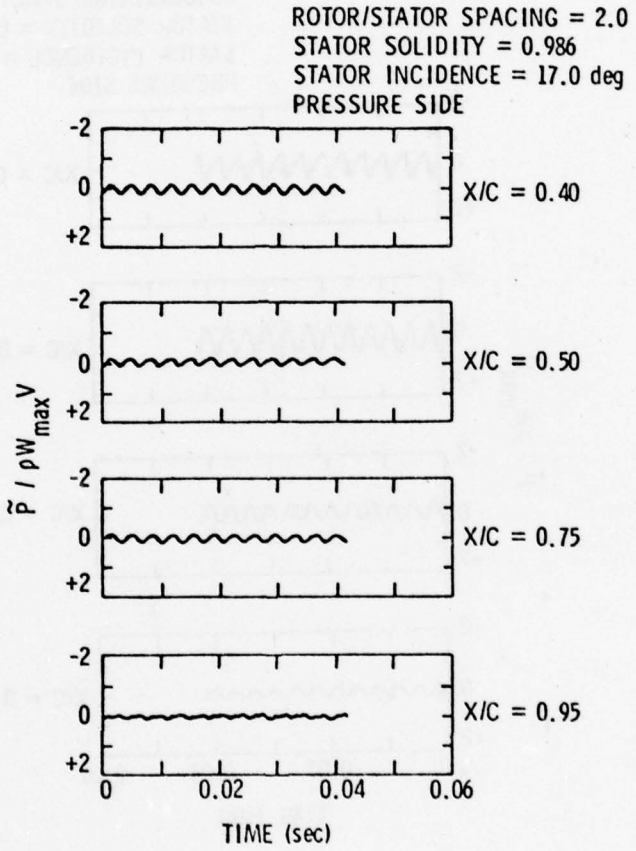
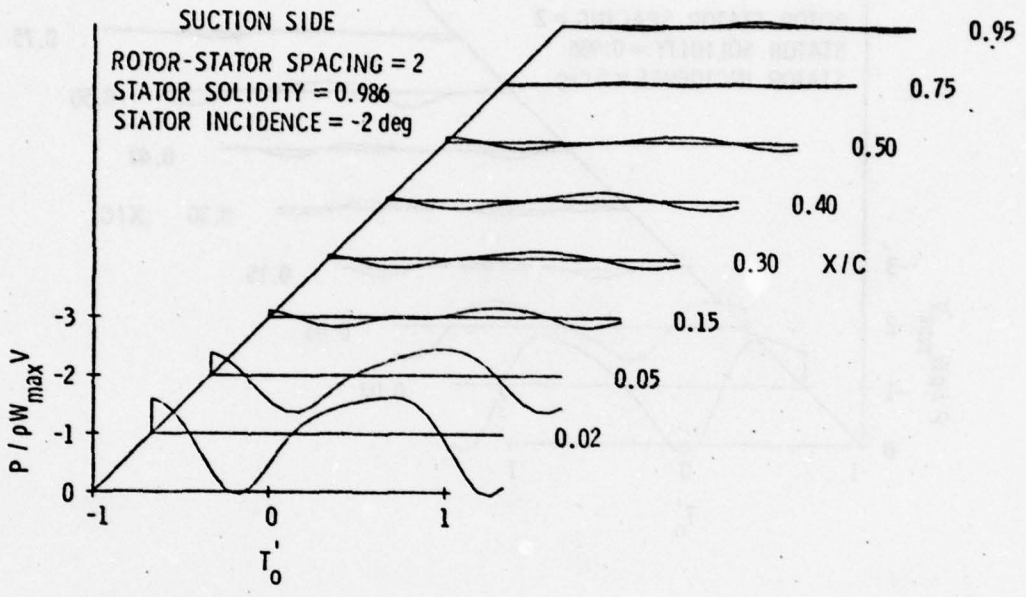


Figure 37 (Cont.)



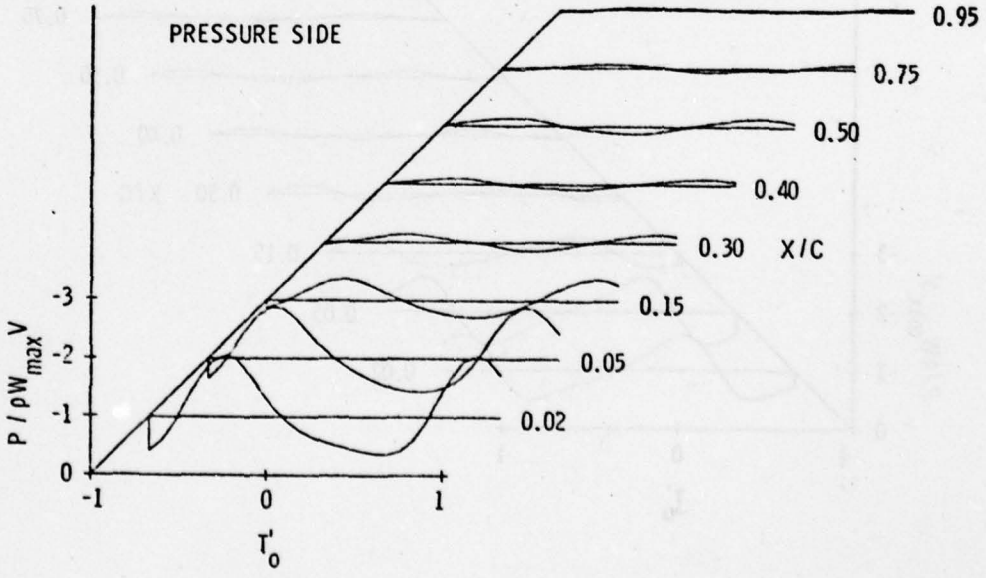


Figure 38 - Unsteady Pressure Coefficient During the Passage of a Single Rotor Wake, i = -2.0 deg

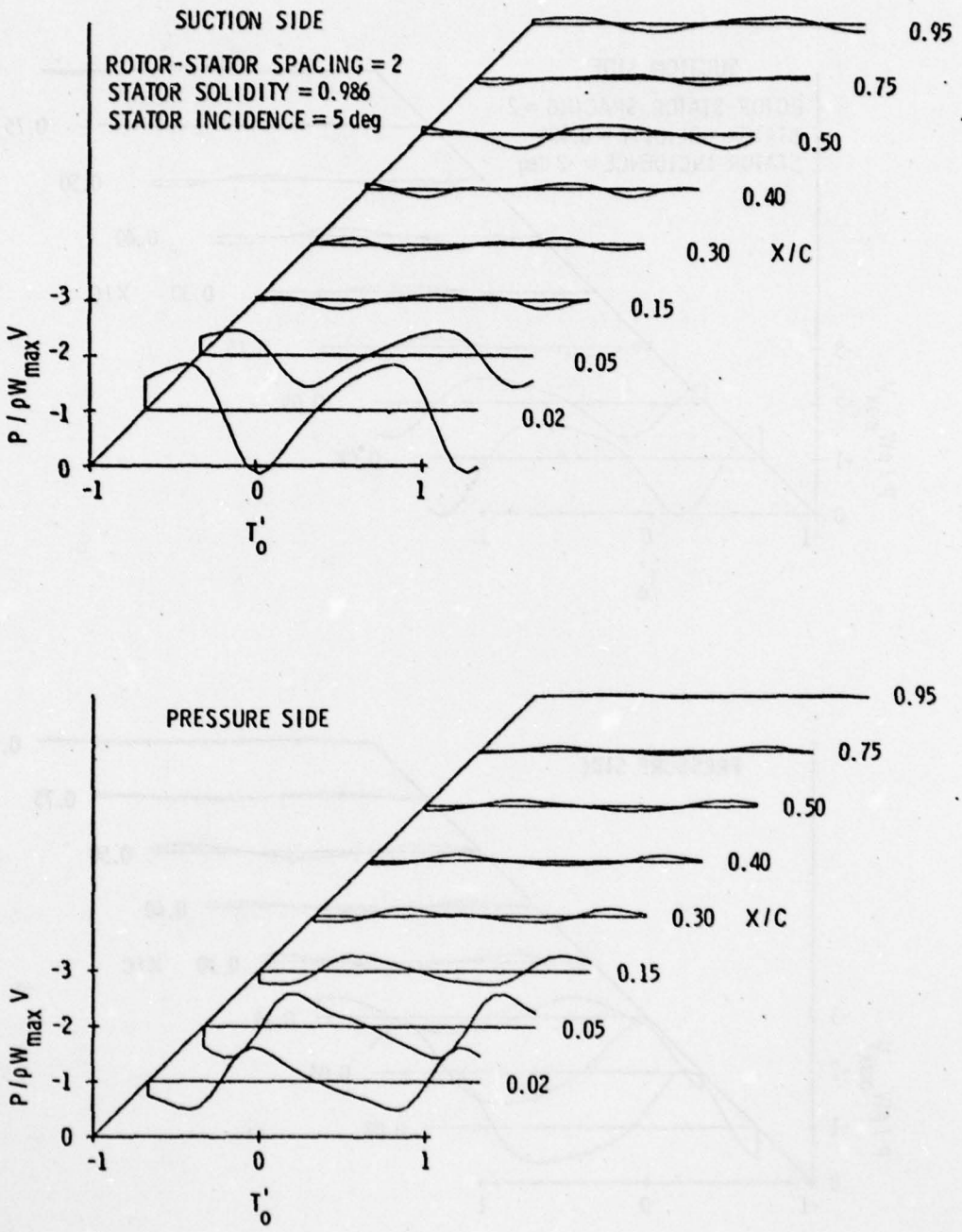


Figure 39 - Unsteady Pressure Coefficient During the Passage of a Single Rotor Wake, i = 5.0 deg

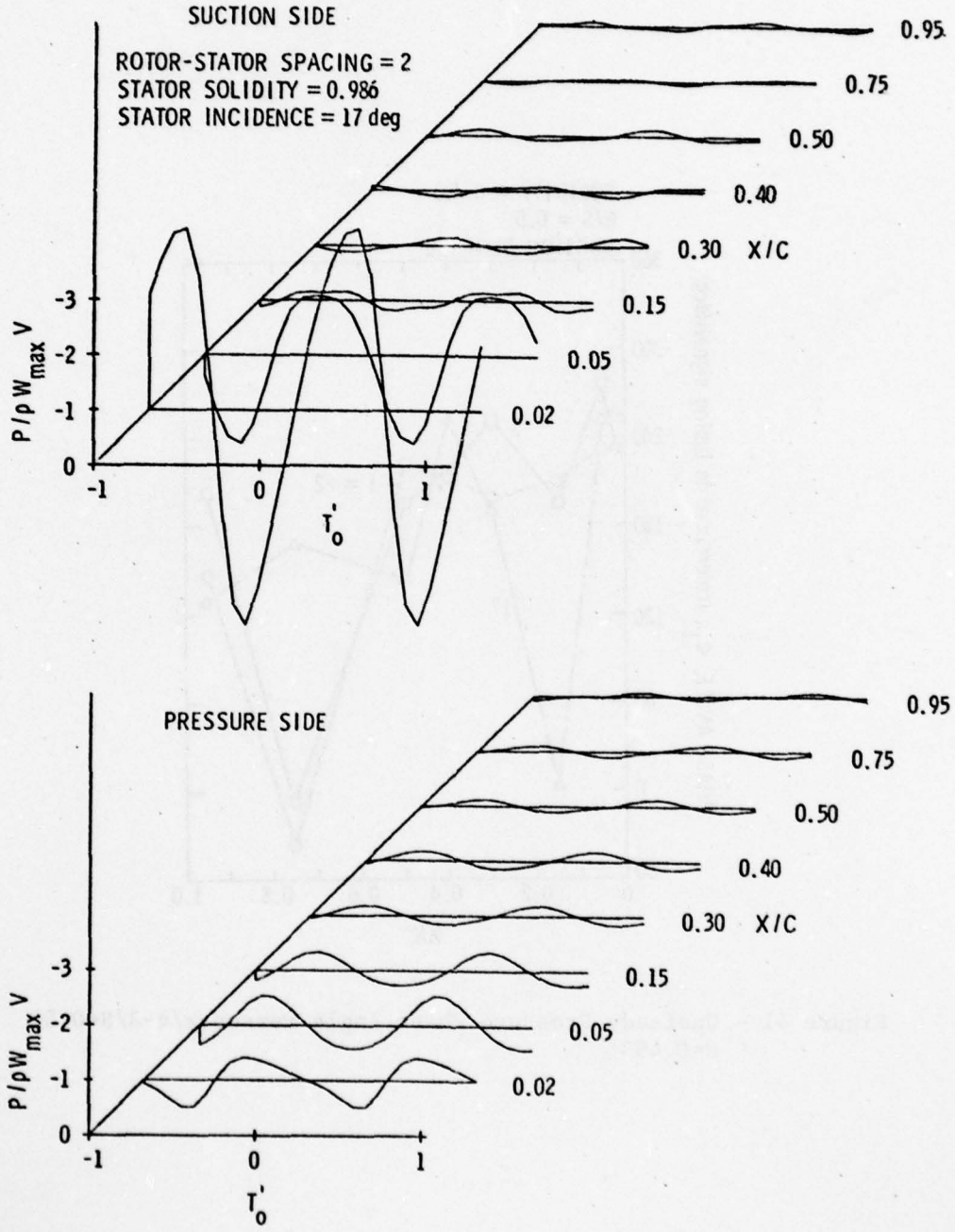


Figure 40 - Unsteady Pressure Coefficient During the Passage of a Single Rotor Wake, i = 17.0 deg

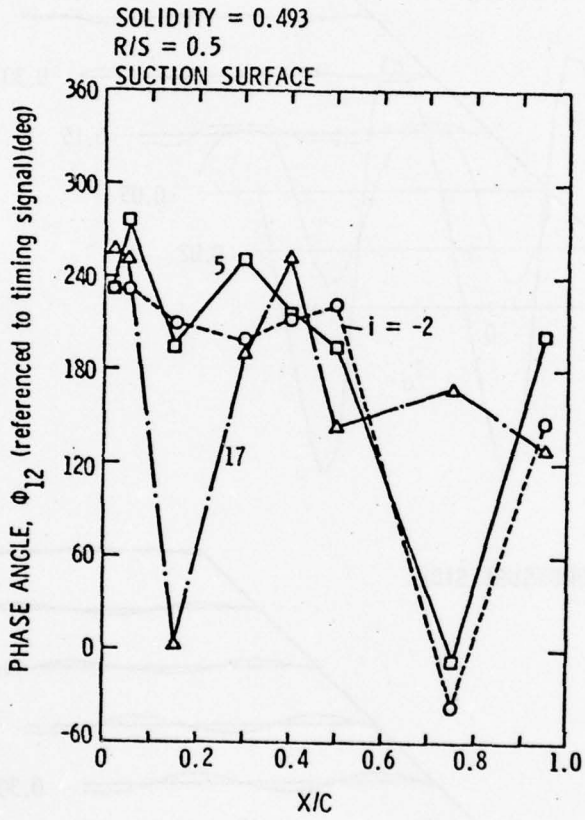


Figure 41 - Unsteady Pressure Phase Angle versus x/c-R/S=0.5, σ=0.493

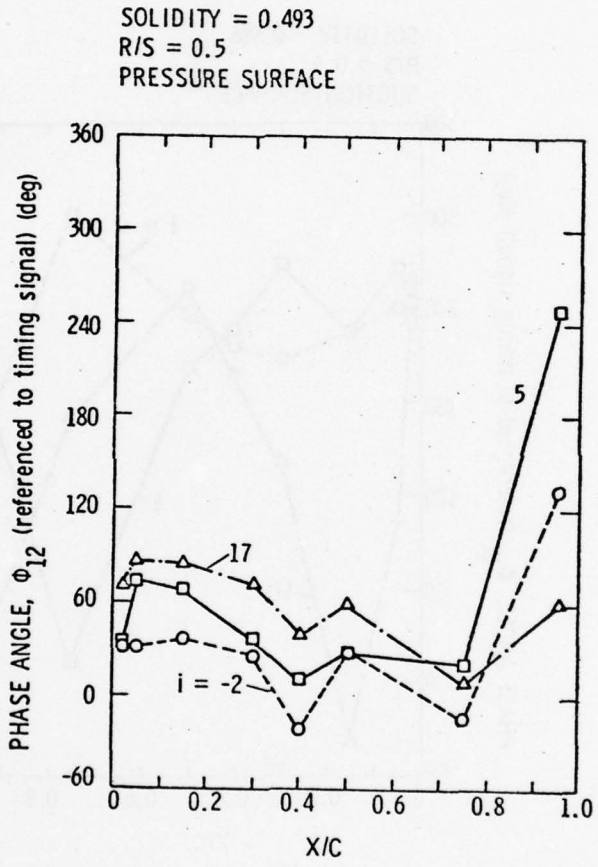


Figure 41 (Cont.)

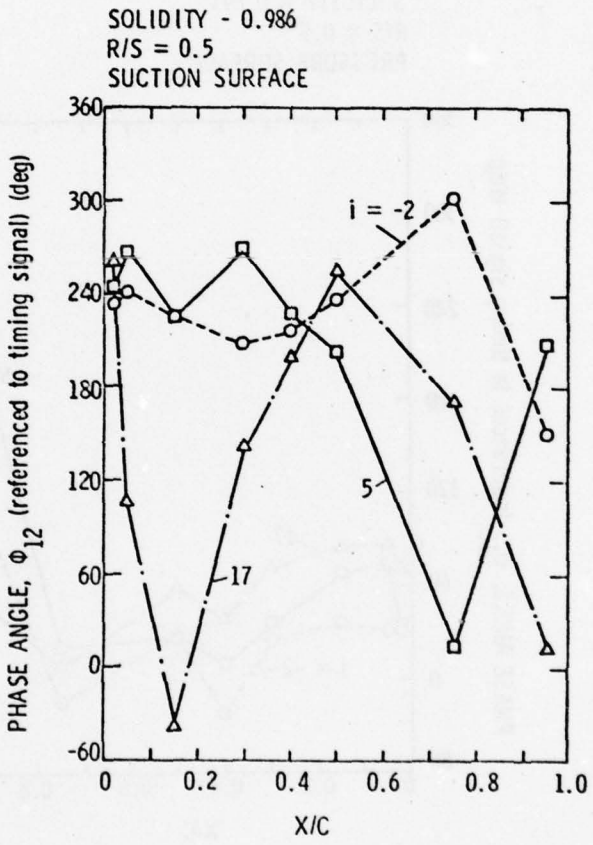


Figure 42 - Unsteady Pressure Phase Angle versus x/c-R/S=0.5, σ=0.986

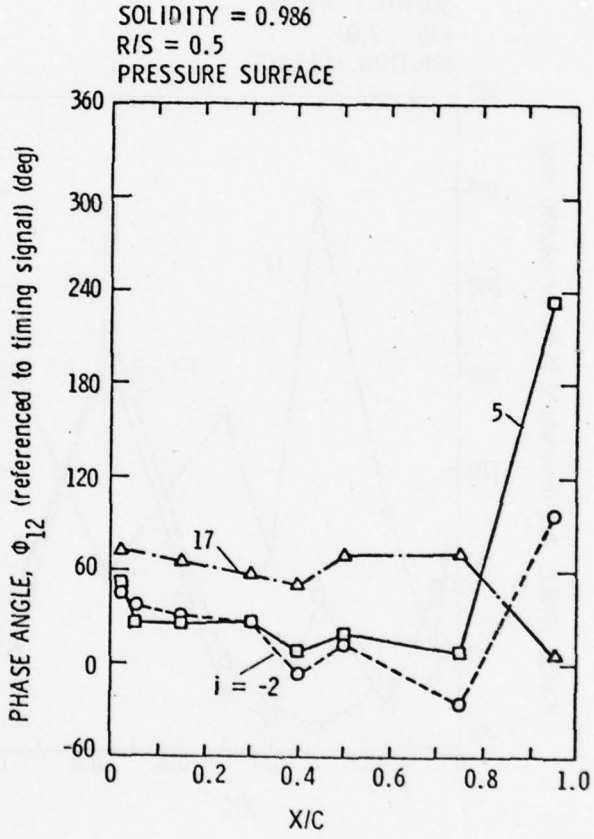


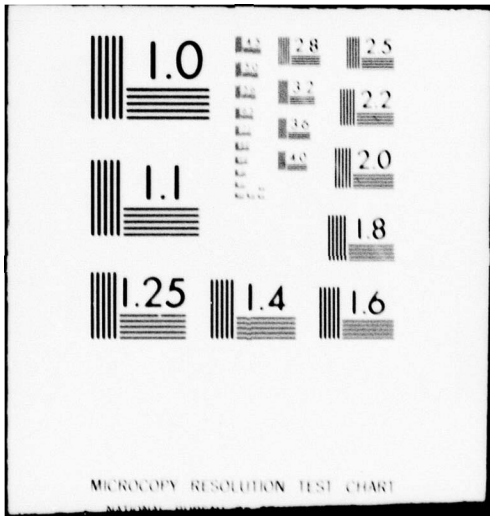
Figure 42 (Cont.)

AD-A060 892 PENNSYLVANIA STATE UNIV UNIVERSITY PARK APPLIED RESE--ETC F/G 21/5
INVESTIGATION OF THE UNSTEADY PRESSURE DISTRIBUTION ON THE BLAD--ETC(U)
MAR 78 R E HENDERSON, G F FRANKE N00017-73-C-1418
UNCLASSIFIED ARL/PSU/TM-78-54 NL

2 OF 2
AD
A060 892



END
DATE
FILMED
1-79
DDC


1.0
1.1
1.25
1.4
1.6
2.8
2.5
2.2
2.0
1.8
MICROCOPY RESOLUTION TEST CHART

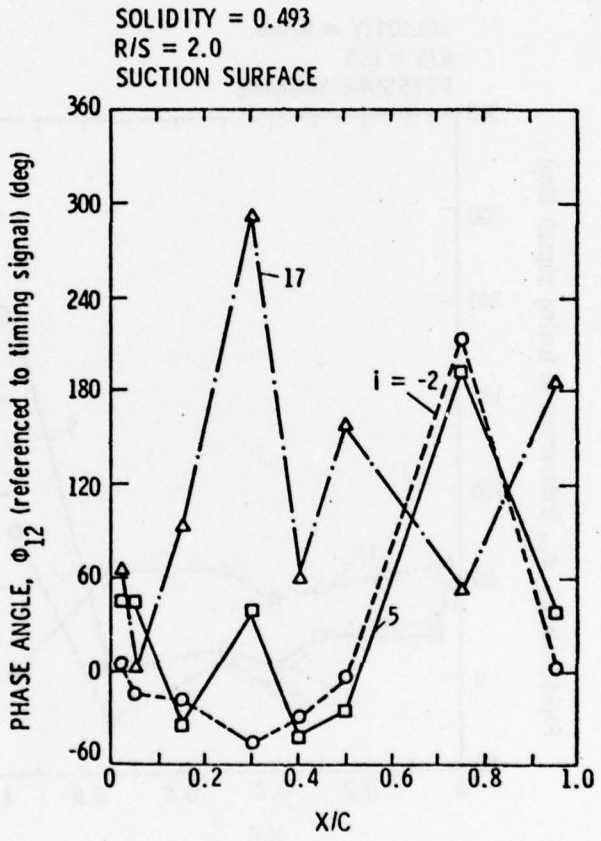


Figure 43 - Unsteady Pressure Phase Angle versus x/c-R/S=2.0, σ=0.493

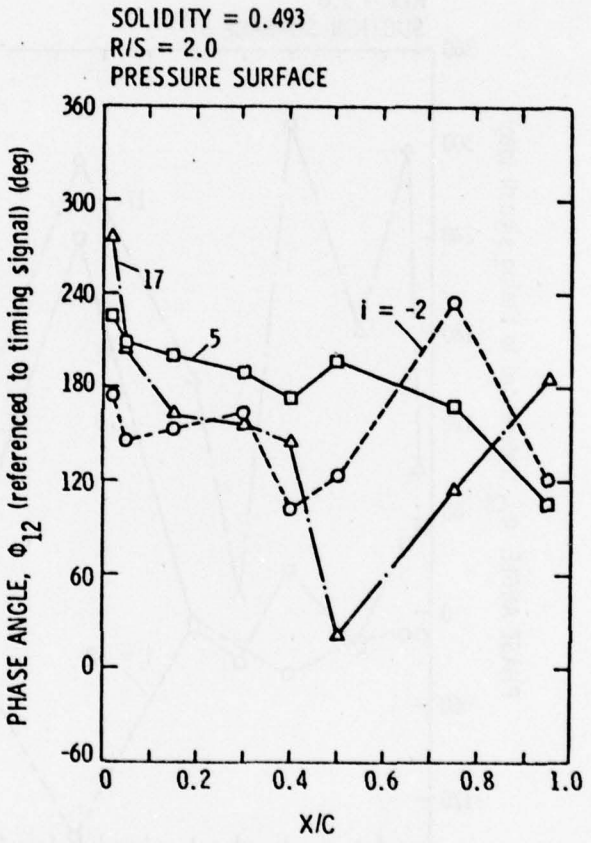


Figure 43 (Cont.)

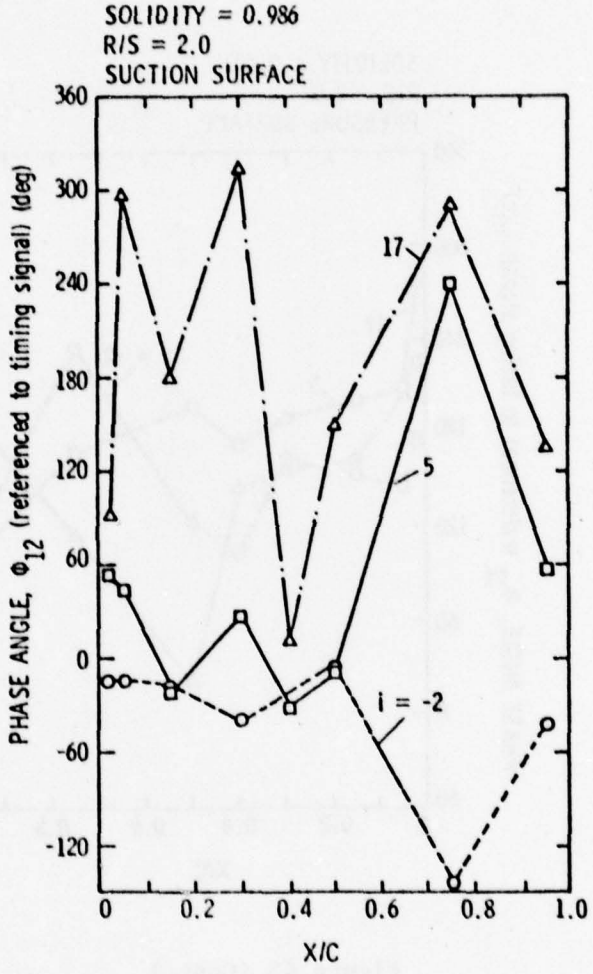


Figure 44 - Unsteady Pressure Phase Angle versus x/c-R/S=2.0, σ=0.986

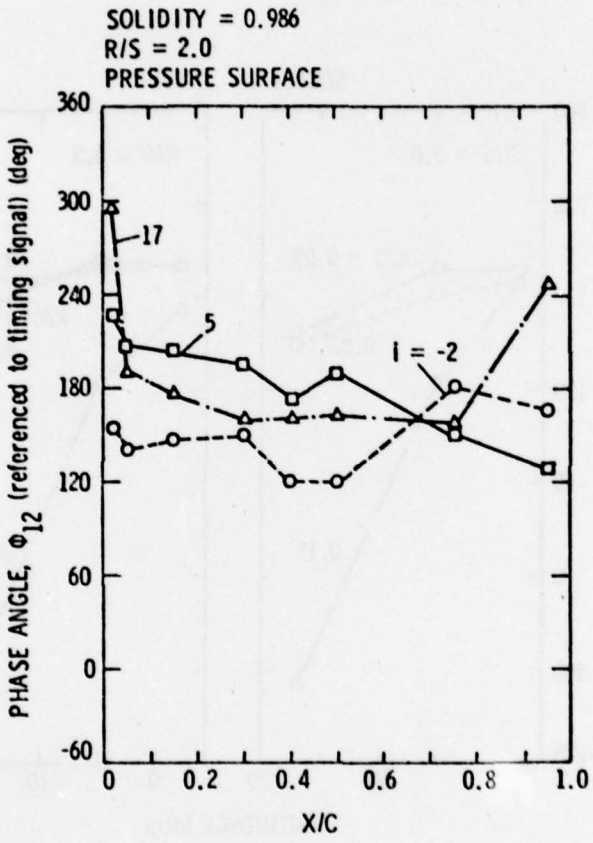


Figure 44 (Cont.)

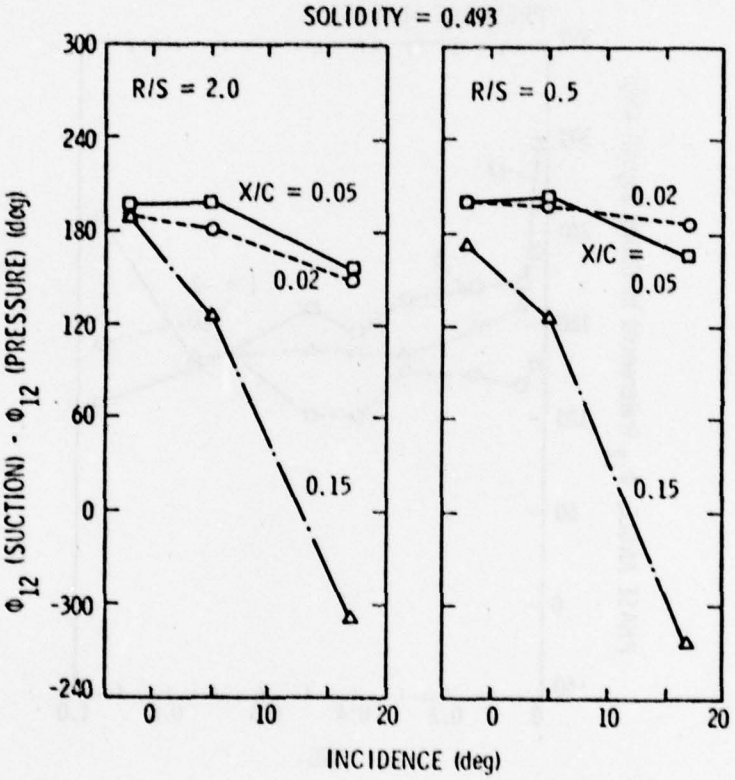


Figure 45 - Suction and Pressure Surface Phase Angle Difference versus Incidence Angle - Blade Passing Harmonic

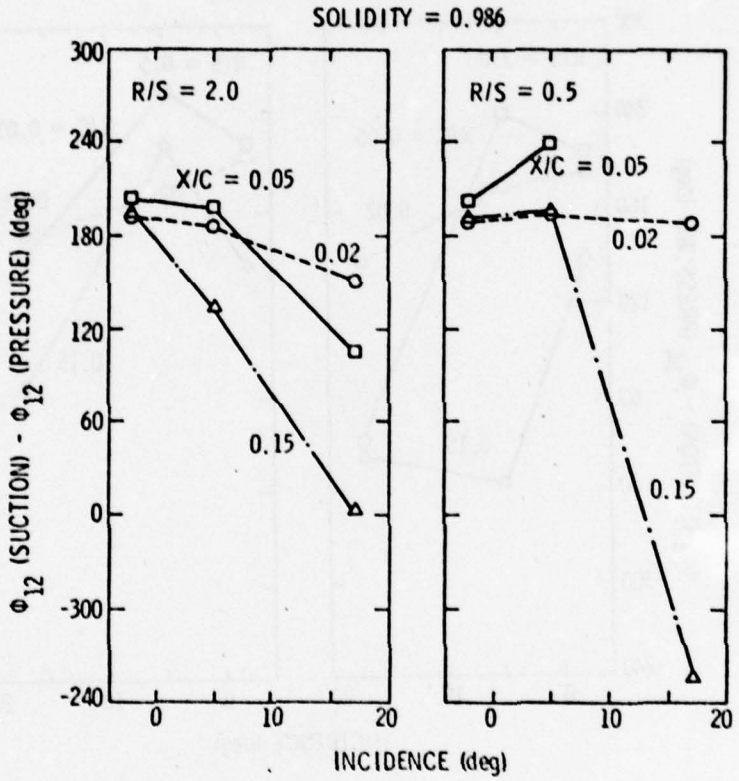


Figure 45 (Cont.)

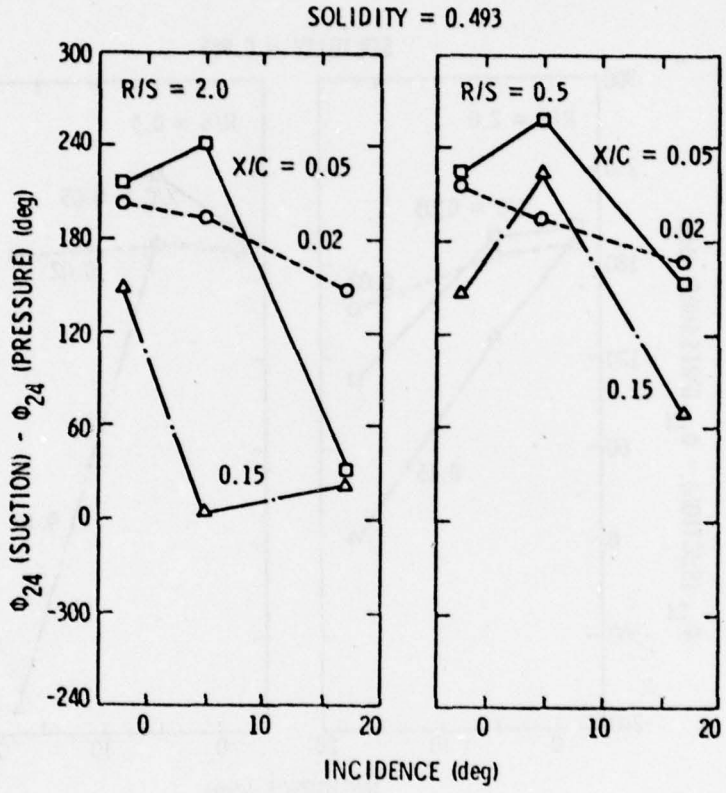


Figure 46 - Suction and Pressure Surface Phase Angle Difference versus Incidence Angle - Twice Blade Passing Harmonic

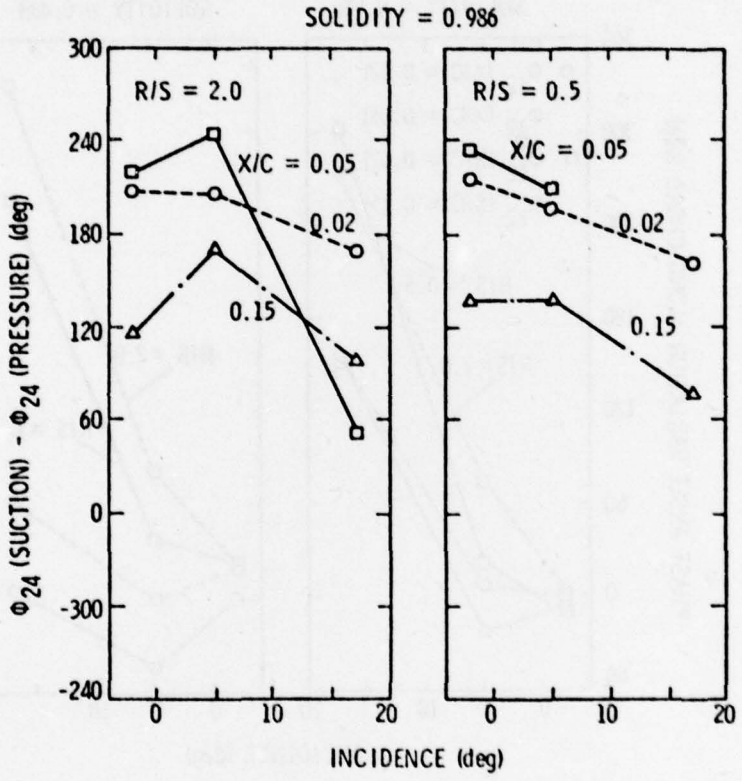


Figure 46 (Cont.)

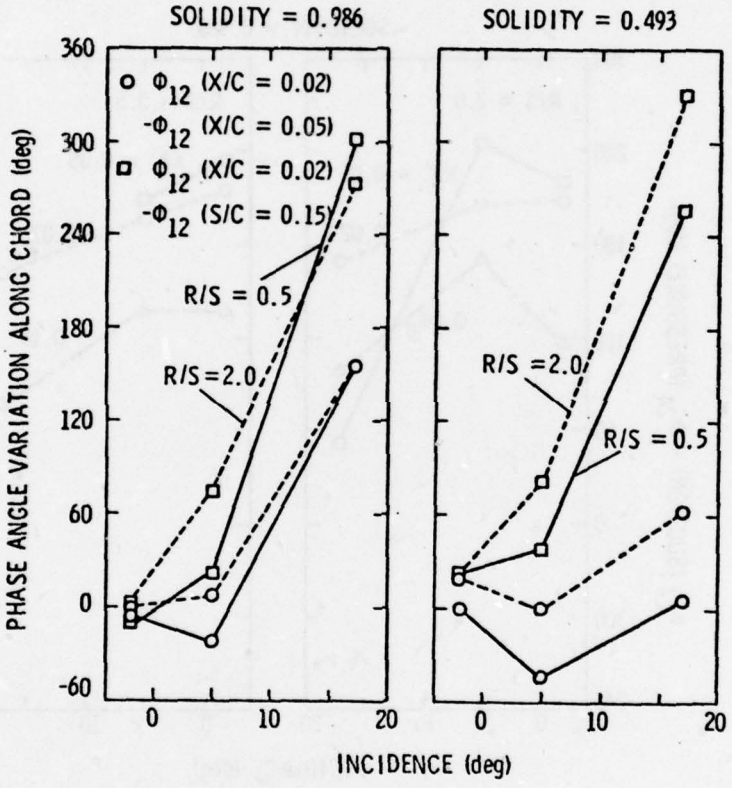


Figure 47 - Relative Phase Angle Along Suction Surface with Incidence Angle - Blade Passing Harmonic

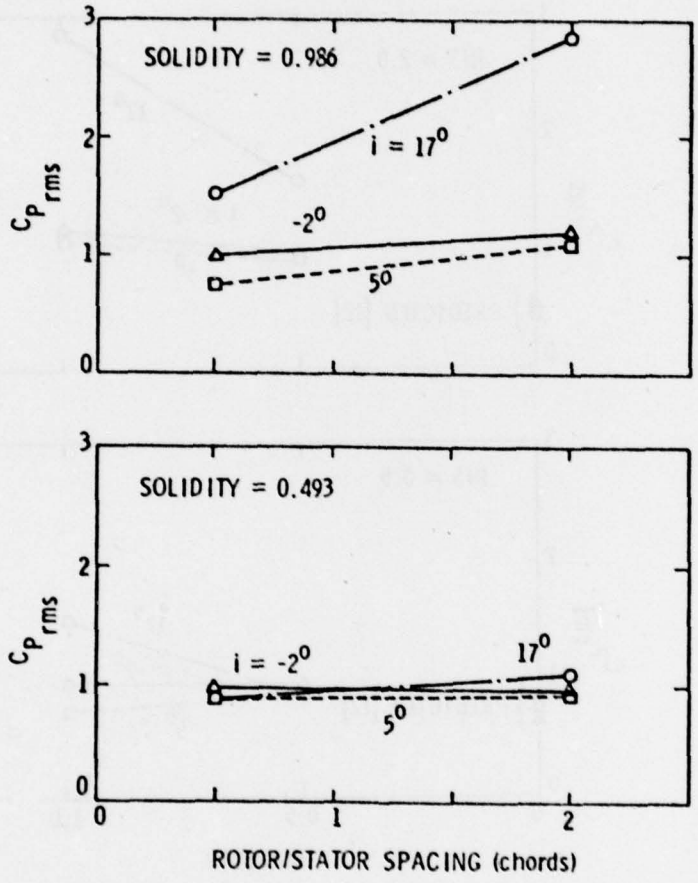


Figure 48 - Variation of $C_{p_{rms}}$ with Rotor/Stator Spacing at x/c=0.02

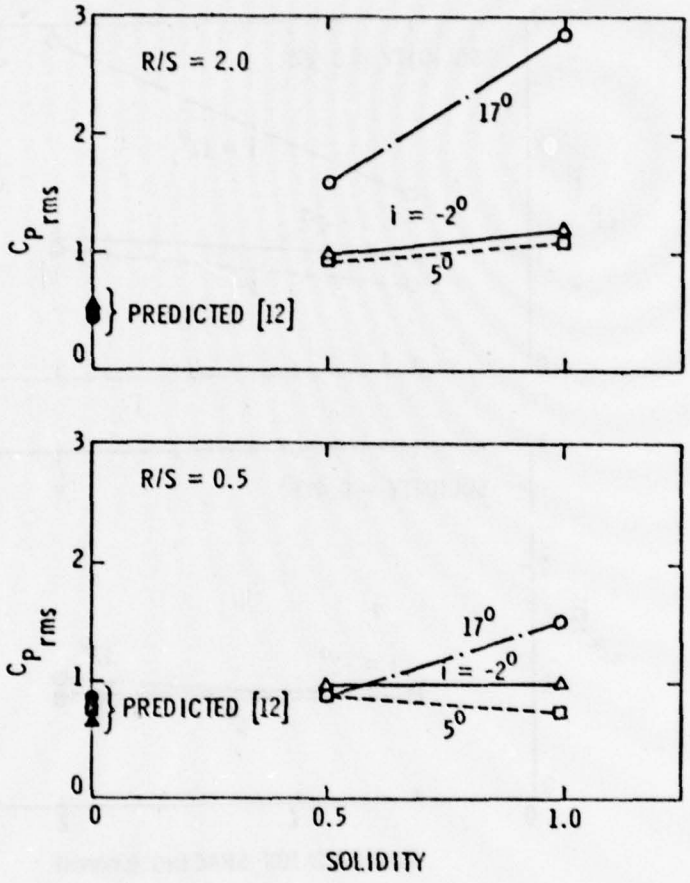


Figure 49 - Variation of $C_{p_{rms}}$ with Solidity at x/c=0.02

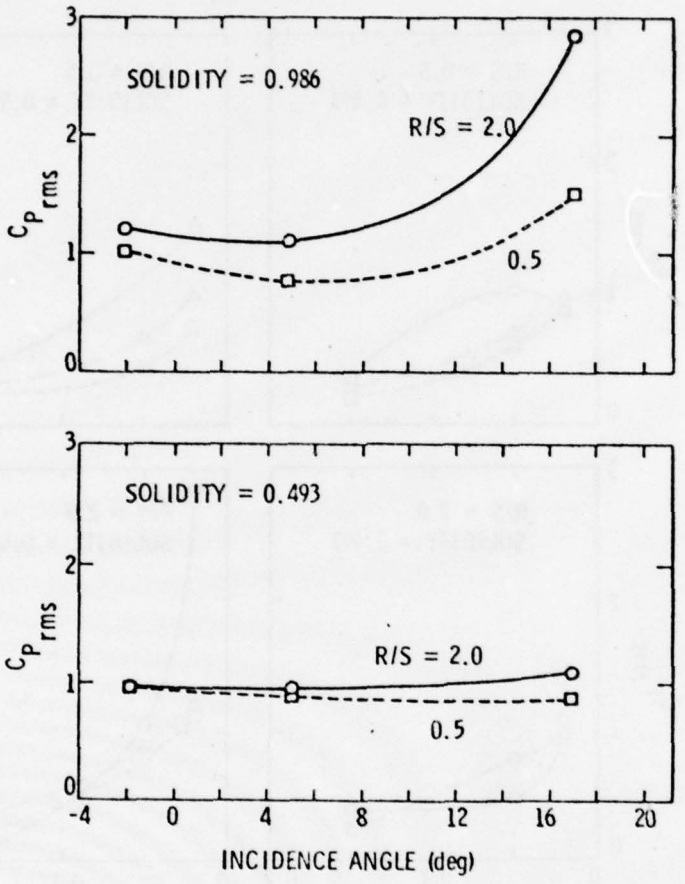


Figure 50 - Variation of $C_{p_{rms}}$ with Incidence Angle at x/c=0.02

14 March 1978
REH:GFF:jep

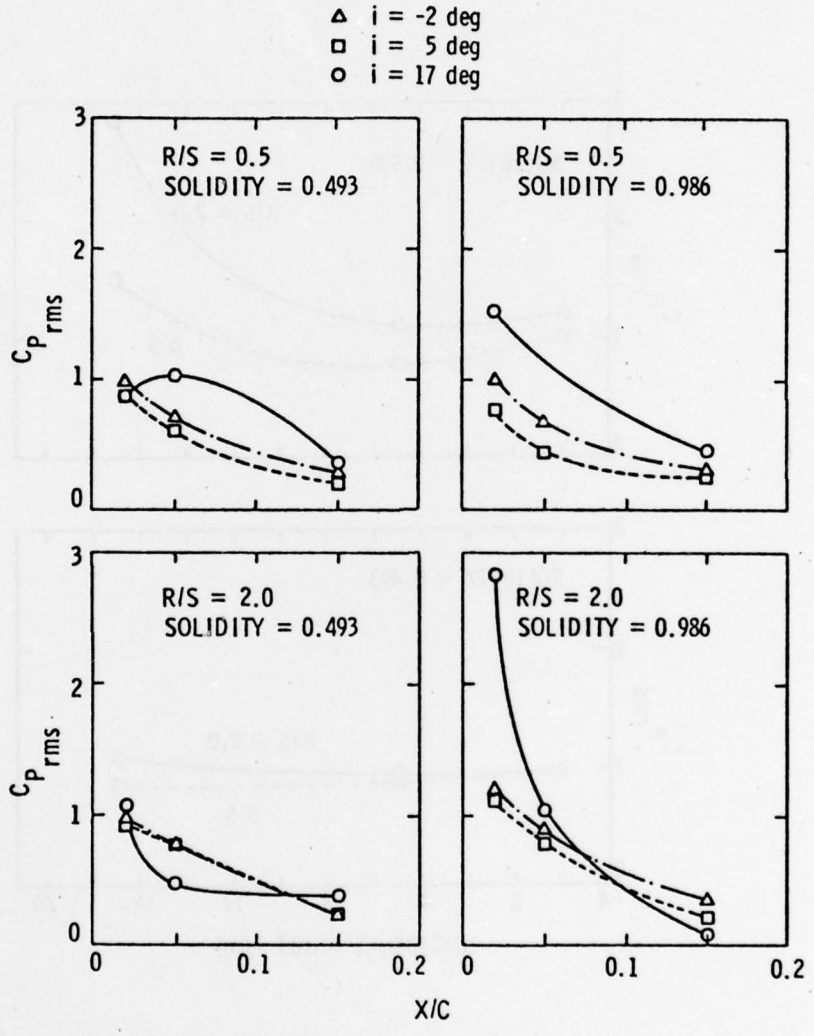


Figure 51 - Variation of $C_{p_{rms}}$ with Chordwise Position

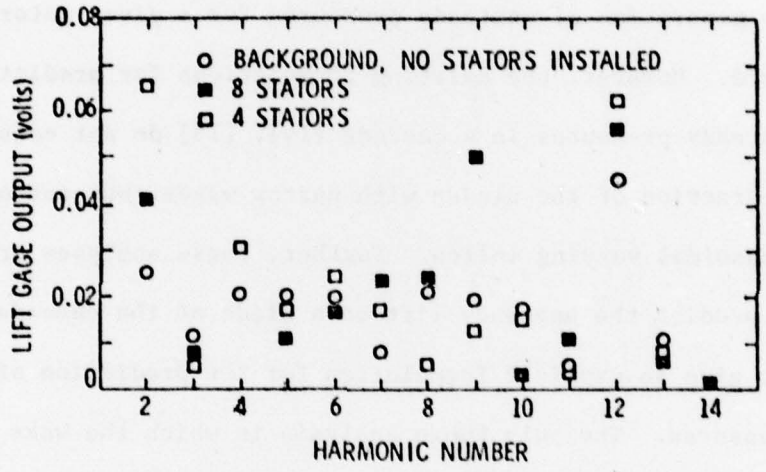


Figure 52 - Magnitude of Unsteady Lift Gauge Output versus Harmonic Number, R/S=0.5 and i = 17.0 degrees

COMPARISON OF THEORETICAL AND EXPERIMENTAL RESULTS

Ideally, the data measured in this study should be compared with an existing theoretical analysis which predicts the unsteady pressures resulting from the interaction of the wakes of an upstream rotor on the stator blades. If such a comparison should result in a favorable comparison, the theoretical analysis could then be employed to determine the influence of the various stator geometrical parameters -- solidity, stagger angle, camber -- or the generation of unsteady pressures for a given rotor wake flow field. However, the existing formulations for predicting the unsteady pressures in a cascade [14], [19] do not consider the interaction of the blades with narrow wakes, but rather a sinusoidal varying inflow. Further, these analyses are written to predict the unsteady lift on a blade of the cascade and do not give an explicit formulation for the prediction of the unsteady pressures. The only known analysis in which the wake interaction is considered is by Meyer [12]. However, it considers only an isolated, two-dimensional airfoil. While there are many dissimilarities between a stator cascade and an isolated airfoil, the data obtained in this study were compared with Meyers analysis.

Meyer was able to obtain the unsteady pressure distribution of an isolated flat plate airfoil moving through a viscous wake when the flow is assumed to be two-dimensional, incompressible and inviscid. Since perfect fluid theory (zero viscosity) cannot account for the formation of viscous wakes or their dissipation, a description of the wakes must be supplied from another source. The wake is analyzed as a region containing vorticity, but governed by the vortex laws of perfect fluids theory.

Meyer, however, considered a flat plate at zero angle of attack with the geometry shown in Figure 53. Meyer's configuration with an upstream stator can be applied to a downstream stator arrangement by a careful interchange of velocities. The wake axis, a line connecting the points of maximum velocity in the jet, is at an angle β to the airfoil or blade under consideration. The velocity defect can then be expressed as components parallel and perpendicular to the blade:

$$u_d = -w(\xi) \cos \beta$$

$$v_d = w(\xi) \cos \beta \quad .$$

It is also assumed that the wake maintains a constant velocity profile and is not distorted by the blade. Using the approximation that the velocity defect is small compared to the velocity relative to the blade outside of the wake, V, and neglecting terms of higher order, Meyer simplified the momentum equation to obtain

$$(\frac{\partial}{\partial t} + V \frac{\partial}{\partial x})\zeta = 0$$

where ζ is the total vorticity. The analysis is also restricted to thin wakes, i.e., if

$$\lambda = \frac{2b}{c \sin \beta}$$

where 2b is the wake thickness where the wake velocity defect is one half of the maximum defect, the analysis requires that $\lambda << 1$.

Meyer developed the following expression for the unsteady pressure assuming infinitely thin wakes

$$\tilde{p}(\theta, t') = \pm\rho V \overline{W} T(t') \tan(\theta/2) \quad , \tag{2}$$

where ± refer to the pressure and suction side of the blade, respectively. This expression uses the nondimensional quantities:

$$x' = \frac{2}{c} x \quad ,$$

$$\theta = \cos^{-1}(x') \quad ,$$

$$t' = \frac{2}{c} V t \quad ,$$

$$\overline{W} = \frac{1}{c} \int_{-\infty}^{\infty} w(\xi) d\xi \quad ,$$

and

$$T(t') = \frac{1}{\pi} \int_{-\infty}^{\infty} S(\omega) e^{i\omega t'} \, dw \quad , \tag{3}$$

where $\overline{W}$ is the integrated velocity defect per blade chord and represents the effect of the wake, $w(\xi)$, where the variable ξ is the distance measured from the wake centerline. The component of the wake profile, $w(\xi)$, parallel to the blade is ignored and the function $S(\omega)$ is the familar Sears function. The nondimensional time t' has the value -1 when the wake is at the leading edge of the airfoil and +1 when the wake reaches the trailing edge. The function $T(t')$ has the value zero for $t' < -1$. At $t' = -1$, $T(t')$ has a singular point similar to the pressure distribution at the leading edge in steady flow. For $-1 < t' < \infty$, $T(t')$ decreases

monotonically to zero at ∞, indicating the wake has a decreasing influence as it passes the leading edge and travels downstream.

Lefort [13] extended Meyer's analysis for wakes of finite but small thickness by superimposing the solutions of many infinitely thin wakes and determined that

$$\tilde{p}(\theta, t_0') = \pm\rho V \tilde{W}(t_0')\tan(\theta/2) \quad , \tag{4}$$

where

$$\tilde{W}(t_0') = \frac{1}{2} \int_{-\infty}^{\infty} w(\xi')T(t_0' + \xi')d\xi' \quad . \tag{5}$$

The nondimensional time t_0' is similar to the previously used t' but refers to the centerline of the wake. The nondimensional distance ξ' is defined as

$$\xi' = \frac{2}{c} \xi \quad .$$

The equations for $\tilde{p}$ state that the pressure distribution on a flat plate remains similar at all times and does not depend on the shape of the wake. The function $T(t')$ is tabulated by Meyer [12] and more extensively by Lefort [13].

Several aspects of the theory will be considered; the magnitude of the unsteady pressures and the shape of the pressure distribution, specifically, the decrease in magnitude with location along the chord. The expression for $\tilde{p}$, Equation (4), states the chordwise variation of the unsteady pressure depends only on $\tan(\theta/2)$ and the time variation depends only on $T(t_0')$. Therefore, the

unsteady pressure at any location on the blade is similar, but different in magnitude, to all other locations at each instance in time.

The unsteady pressures on the pressure and suction side of the blade at a constant value of x/c are predicted to be opposite in signs, i.e., 180 degrees out of phase and equal in magnitude. The validity of the prediction that pressures on opposite sides of the blade are 180 degrees out of phase has been previously discussed. At locations near the leading edge, the pressures are nearly 180 degrees out of phase. The difference in phase angle changes at other locations on the blade. This deviation from 180 degrees increases with increasing incidence angle.

The peak-to-peak magnitude of the measured pressure coefficient, $\tilde{p}/\rho W_{MAX}$ V, summarized in Table 1, shows the magnitude of the pressure coefficient on the suction and pressure sides of the blade to be equal only at an incidence of -2 degrees, at the position x/c = 0.02 and with a solidity of 0.986. The pressure coefficients are within 10% of each other for these conditions with a solidity of 0.493. At all other positions on the blade and all other incidences, the magnitude of the coefficients are not equal. This demonstrates, as would be expected, that the influence on angle of incidence is to make the pressures on the suction and pressure surfaces unequal. If Meyer's analysis were altered to include the effects of angle of incidence, at best it would predict the difference in pressure between the suction and pressure surfaces.

A comparison of the chordwise variation of the measured and predicted pressure difference across the blade, Cp_{rms} (defined by Equation (1), is shown in Figure 54 for a rotor/stator spacing of 2 chordlengths, a solidity of 0.986 and an incidence of -2 degrees. This comparison indicates that the shape of the variation of Cp_{rms} along the chord from both the theory and the experiment are similar. The magnitude of the unsteady pressure difference, Cp_{rms}, at x/c = 0.02 predicted by theory is less than the measured value and are compared in Table 2. The predicted value generally is about one half the measured value. However, the predicted values are for an isolated airfoil, zero solidity. When these predicted values are compared with the variation of Cp_{rms} with solidity at x/c=0.02 (see Figure 49), it appears that the measured data are tending to the predicted value at σ=0.

The parameter λ, which is required to be much less than one in the development of the theory, varies from 0.15 at rotor/stator spacing of 2.0 to 0.07 at rotor/stator spacing of 0.5. Thus, the condition that $\lambda \ll 1$ has been fulfilled by the experimental data.

In general, the comparison of the measured unsteady pressures in a cascade with the isolated airfoil analysis by Meyer [12] is poor. The variation in measured data with rotor/stator spacing is a function of the wake flow interacting with the blades and represents the data which must be input to either a cascade or isolated airfoil analysis. On the other hand, the influence of solidity and the chordwise component of the wake are not included in Meyer's analysis. The present data indicate that (1) at large angles of incidences which give an appreciable chordwise wake

component, the chordwise component does indeed contribute, Figure 50, and (2) the solidity of the cascade does influence the unsteady pressures on the blades, Figure 49. Additionally, although not investigated in this study, there will be an influence of stagger angle as demonstrated by Satynarayana's data [25]. Thus, a better theoretical model should be developed for the interaction of thin wakes with a cascade of airfoils which includes the effects of the chordwise wake component, blade-to-blade interactions (solidity) and stagger angle.

Rotor/ Stator Spacing	Stator Solidity	Stator Incidence	$(\tilde{p}/\rho W_{MAX} V)_{peak-to-peak}$ x/c = 0.02 Suction	x/c = 0.02 Pressure	x/c = 0.05 Suction	x/c = 0.05 Pressure	x/c = 0.15 Suction	x/c = 0.15 Pressure
2.0	0.986	-2	1.67	1.69	1.07	1.44	0.33	0.68
2.0	0.986	5	1.97	1.14	1.02	1.15	0.26	0.53
2.0	0.986	17	7.17	0.90	2.67	0.96	0.35	0.60
0.5	0.986	-2	1.43	1.40	0.78	1.14	0.28	0.60
0.5	0.986	5	1.38	0.77	0.93	0.48	0.37	0.35
0.5	0.986	17	3.46	0.84	2.38	----	0.75	0.89
2.0	0.493	-2	1.43	1.29	0.95	1.25	0.23	0.52
2.0	0.493	5	1.65	1.00	1.16	1.00	0.41	0.48
2.0	0.493	17	2.47	0.62	0.85	0.46	1.13	0.27
0.5	0.493	-2	1.31	1.43	0.82	1.17	0.27	0.52
0.5	0.493	5	1.64	0.85	1.09	0.65	0.39	0.28
0.5	0.493	17	1.83	0.63	1.98	0.95	0.95	-.47

Table 1 - Summary of Measured Peak-to-Peak Pressure Coefficients for x/c = 0.02, 0.05, 0.15

14 March 1978
REH:GFF:jep

Rotor/ Stator Spacing	Incidence	Solidity	Cp_{rms} Measured	Cp_{rms} Predicted
2.0	-2	0.986	1.19	0.59
2.0	5	0.986	1.10	0.56
2.0	17	0.986	2.85	0.45
2.0	-2	0.493	0.96	0.55
2.0	5	0.493	0.94	0.54
2.0	17	0.493	1.10	0.48
0.5	-2	0.986	1.00	0.66
0.5	5	0.986	0.76	0.72
0.5	17	0.986	1.52	0.84
0.5	-2	0.493	0.97	----
0.5	5	0.493	0.68	----
0.5	17	0.493	0.87	0.76

Table 2 - Comparison of Cp_{rms} Measured and Predicted at x/c = 0.02

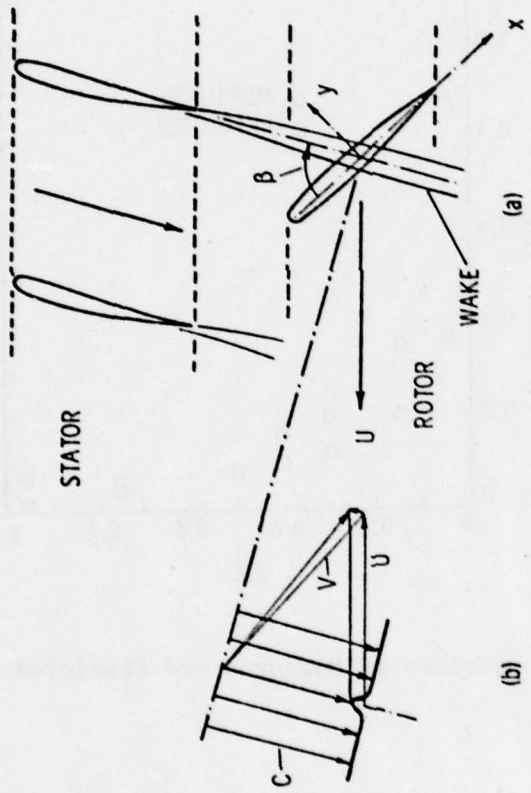


Figure 53 - Compressor Blade Wake Interaction Considered by Meyer [12]

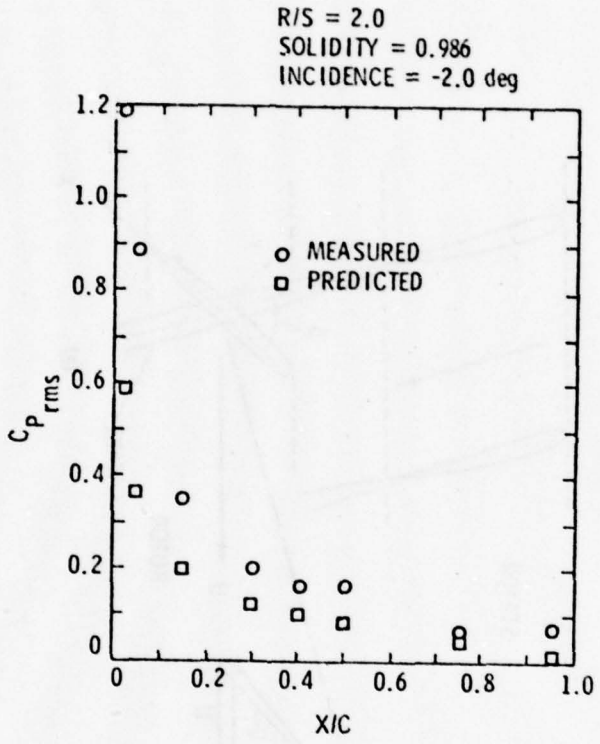


Figure 54 - Comparison of Measured and Predicted $C_{P_{rms}}$

SUMMARY AND CONCLUSIONS

The purpose of this study was to investigate the unsteady response of a stator blade caused by the interaction of the stator with the wakes of an upstream rotor. A major portion of this effort was the development of an instrumented stator to allow the measurement of the unsteady pressures on both its pressure and suction sides during such an interaction. This development was successfully completed and a series of measurements were conducted to demonstrate the effects of (1) rotor/stator spacing, (2) stator solidity and (3) circumferential time-mean incidence angle on the unsteady pressures on the stator surfaces.

The following conclusions are drawn regarding the instrumentation employed in this study:

1. The range of pressure transducers used in this study was adequate to measure unsteady pressures on the blades of the Axial Flow Research Fan. The largest peak-to-peak pressure generated by a viscous wake was $\tilde{p}/\rho W_{MAX}\, V = 7.25$ which corresponds to a value to $\tilde{p}$ equal to 2.75 cm of water. The pressures actually experienced by the transducer were larger than this value due to the presence of perturbations which were not periodic with the rotor rpm. These perturbation pressures were eliminated by ensemble averaging. Peak-to-peak pressures as small as $\tilde{p}/\rho W_{MAX}\, V = 0.25$, which corresponds to a value of $\tilde{p}$ equal to approximately 0.095 cm of water, could be discerned in the plotted output.

2. The Pitran pressure transducers were adequate to conduct the required measurements. Several disadvantages, however, indicate the desirability of continuing to investigate alternate pressure transducers. The most severe disadvantage was the Pitran's susceptibility to electrical interference. Much effort was spent (unsuccessfully) trying to eliminate 60 Hz interference and high frequency electromagnetic pickup from the SCR's in the rotor and auxiliary fan motor controllers. The Pitrans were also very fragile and susceptible to mechanical damage; the calibration constant could change if the blade were disassembled and reassembled. Additionally, because of their temperature sensitivity the dc output of the Pitran must be electrically cancelled which means that the time-mean pressures cannot be measured.
3. The ensemble averaging technique employed was necessary to permit the analysis of these data. Random fluctuations and unsteady pressures which are not periodic with the rotor can be successfully eliminated by this technique.
4. The strain gauge instrumented rotor blade and associated signal conditioning did not have sufficient sensitivity to measure the rotor/stator potential interaction. Based on earlier measurements with this rotor blade, it is concluded that the potential interaction unsteady lift is significantly less than the blade-wake interaction unsteady lift.

5. The distribution of pressure sensing ports should be more heavily weighted toward the leading edge of the blade since the major changes in unsteady pressure occur at the leading edge.

6. The arrangement of a cavity-surface tap to measure the unsteady pressures is judged to be better than a flush-mounted transducer. The flush mounted transducers, although not employed in this study, are difficult to mount on a curved surface without giving rise to surface irregularities. The cavity-surface tap arrangement can be designed to avoid cavity resonance problems.

From the unsteady pressure measurements obtained, it is concluded that:

(1) A major effect on the unsteady stator pressure is due to the solidity of the stator blade row. At low solidity, 0.493, $C_{p_{rms}}$ was observed to be relatively insensitive to rotor/stator spacing and stator incidence angle. At a solidity of 0.986, however, there are large effects due to the change in rotor/stator spacing and incidence. At the higher solidity, the blade-to-blade interactions have a larger contribution.

(2) There is a positive value of the angle of incidence that minimizes $C_{p_{rms}}$. This agrees with the trends predicted by both unsteady isolated airfoil and cascade analyses in which the effects of angle of attack on the unsteady lift are considered.

(3) The range of rotor/stator spacing investigated has a weak influence on $C_{p_{rms}}$. $C_{p_{rms}}$ was slightly higher at a spacing of two chord lengths. This indicates only a minor change in the wake characteristics in this range of rotor/stator spacing.

(4) The phase angle of the unsteady pressure fluctuations on the blade shows significant variation on the suction surface while being relatively constant on the pressure surface. With increasing angle of incidence the variations on the suction surface become much larger. It is suspected that this is due to local flow separation.

(5) The difference in phase angle between the suction and pressure surfaces of the blades is approximately 180 degrees at the leading edge of the blade and tends toward zero degrees at the trailing edge.

(6) The Kutta condition can be satisfied at the trailing edge of the blade by the existence of a nonzero value of pressure on the suction and pressure surfaces of the blade. In this case, the surface pressures are in phase and equal in magnitude thus giving a zero pressure difference at the trailing edge. This is different than the available theoretical analyses which state that the pressure on each surface is zero and 180 degrees out of phase at the trailing edge.

Several observations are made concerning the theoretical prediction by Meyer [12] (and Lefcort [13]) which were compared with the experimental data. These observations are:

(1) The prediction that the unsteady pressure on opposite sides of the blade are opposite in sign (180 degrees out of phase) is only true at low values of incidence near the leading edge of the blade. The phase angle between pressures on opposite sides of the blade changes significantly with incidence angle.

(2) The predicted unsteady pressure coefficient is approximately one half the measured unsteady pressure coefficient. However, the measured values of unsteady pressure coefficient appear to approach the predicted values at zero solidity.

(3) The prediction that suction side and pressure side unsteady pressures are equal in magnitude was found to be true only at x/c = 0.02 with an incidence of -2 degrees and solidity of 0.986 and approximately true at these conditions and a solidity of 0.493. There were large differences at other values of incidence and x/c.

RECOMMENDATIONS

Based on the experience and results obtained in conducting this study, there are several recommendations which are pertinent to further research conducted regarding the unsteady response of an axial flow fan rotor to spatial inflow distortions. These are:

(1) The investigation of the response of a stator to the wakes of an upstream rotor, while being a very important problem, does not represent a "clean" experimental step-up. As a result, it is difficult to draw hard conclusions regarding the influence of various geometrical and flow characteristics on the unsteady response of the axial flow fan blades. A much "cleaner" experimental step-up is that employed in Reference [35] with a rotating blade row and simplified sinusoidal spatial distortions.

(2) The detailed measurement of unsteady pressures on the blades of an axial flow fan, represent a necessary piece of experimental data to permit the determination of unsteady fan design data. Such data are also important in the development of a knowledge of the boundary layer and wake on a blade which experiences an unsteady interaction. It is necessary then to conduct additional measurements of the unsteady pressures in a test set-up similar to that employed in [35], i.e., a rotor blade interacting with the simple sinusoidal spatial distortion.

(3) The instrumentation development conducted in this study should be extended to provide a rotor blade on which unsteady pressure distribution can be measured. The same basic technique should be employed, except different pressure sensors which are less fragile and temperature sensitive should be employed.

(4) Efforts should be made to develop an unsteady cascade analysis which will predict the unsteady pressure distributions while including the influence of solidity, stagger angle, camber, thickness and angle of incidence. This analysis should not be restricted to the prediction of the pressure difference across the blade, but should provide the pressures on each side. The effects of thin wakes such as studied by Meyer [12] and Lefcort [13] should also be included.

(5) After verification of this advanced analysis by experiment, it should be used to obtain unsteady design data which demonstrate the influence of blade geometry and flow characteristics.

(6) Experimental data should be obtained which demonstrate the behavior of the blade boundary layers, i.e., transition and separation, during the interaction of the blade with a spatial distortion. Such measurements could be obtained with flush mounted hot-film sensors. Additionally, time varying measurements of the blade boundary layer profile and wake should be obtained to provide a better description of the unsteady blade interaction problem.

ACKNOWLEDGMENTS

This study was conducted under the primary sponsorship of NASA Research Grant No. NGR 39-009-275, Lewis Research Center. The administration of this grant was conducted through the Department of Mechanical Engineering, The Pennsylvania State University. Partial support was provided by the U. S. Navy, Naval Sea Systems Command, Code 035, through the Applied Research Laboratory, The Pennsylvania State University (ARL/PSU) which made available the facilities used in this study.

REFERENCES

1. "Aircraft Engine Noise Reduction," Proceedings of a Conference held at Lewis Research Center, May 16-17, 1972, NASA SP-311.

2. Mugridge, B. D. and Morfey, C. L., "Sources of Noise in Axial Flow Fans," Journal of the Acoustical Society of America, Vol. 51, No. 5 (Part I), 1972.

3. Bragg, S. and Bridge, R., "Noise from Turbojet Compressors," Journal of the Royal Aeronautical Society, Vol. 68, No. 637, pp. 1-10, January 1964.

4. Morfey, C. L., "Sound Generation in Subsonic Turbomachinery," Journal of Basic Engineering, ASME Transactions, Vol. 92D, pp. 450-458, September 1970.

5. Kemp, N. H. and Sears, W. R., "Aerodynamics Interference Between Moving Blade Rows," Journal of the Aeronautical Sciences, Vol. 20, No. 9, pp. 585-597 and 612, September 1953.

6. Kemp, N. H. and Sears, W. R., "The Unsteady Forces Due to Viscous Wakes in Turbomachines," Journal of the Aeronautical Sciences, Vol. 5, No. 10, pp. 379-390, August 1938.

7. von Karman, T. and Sears, W. R., "Airfoil Theory for Nonuniform Motion," Journal of the Aeronautical Sciences, Vol. 5, No. 10, pp. 379-390, August 1938.

8. Sears, W. R., "Some Aspects of Nonstationary Airfoil Theory and Its Practical Application," Journal of Aeronautical Sciences, Vol. 8, No. 3, pp. 104-108, January 1941.

9. Horlock, J. H., "Fluctuating Lift Forces on Aerofoils Moving Through Transverse and Chordwise Gusts," Journal of Basic Engineering, ASME Transactions, Vol. 90D, No. 4, pp. 494-500, 1968.

10. Naumann, H. and Yeh, H., "Lift and Pressure Fluctuations of a Cambered Airfoil Under Periodic Gusts and Applications in Turbomachinery," Journal of Engineering for Power, ASME Transactions, Series A, Vol. 95, pp. 1-10, 1973.

11. Yeh, H. and Eisenhuth, J. J., "The Unsteady Wake Interaction in Turbomachinery and Its Effect on Cavitation," Journal of Basic Engineering, ASME Transactions, Series D, Vol. 81, pp. 181-189, 1959.

12. Meyer, R. X., "The Effect of Wakes on the Transient Pressure and Velocity Distributions in Turbomachines," ASME Transactions, Vol. 80, p. 1544, 1958.

13. Lefcort, M. D., "An Investigation Into Unsteady Blade Forces in Turbomachines," Journal of Engineering for Power, ASME Transactions, Series A, Vol. 87, pp. 345-354, 1965.

14. Whitehead, D. S., "Force and Moment Coefficient for Vibrating Aerofoils in Cascade," Aeronautical Research Council R and M 3254, February 1960.

15. Whitehead, D. S., "Bending Flutter of Unstalled Cascade Blades at Finite Deflection," Aeronautical Research Council R and M 3386, October 1962.

16. Lotz, M and Raabe, J., "Blade Oscillations in One-Stage Axial Turbomachinery," Journal of Basic Engineering, ASME Transactions, Vol. 90D, No. 4, pp. 485-493, 1968.

17. Smith, S. N., "Discrete Frequency Sound Generation in Axial Flow Turbomachines," University of Cambridge, Engineering Department Report, CUED/A-Turbo/TR29 (1971).

18. Arnoldi, R. A., "Unsteady Airfoil Response," NASA SP-207, 1969, pp. 247-256.

19. Henderson, R. E. and Daneshyar, H., "Theoretical Analysis of the Fluctuating Lift on the Rotor of an Axial Turbomachine," Aeronautical Research Council R and M 3684, 1972.

20. Henderson, R. E., "The Unsteady Response of an Axial Flow Turbomachine to an Upstream Disturbance," Ph.D. Dissertation, Churchill College, University of Cambridge, 1972.

21. Henderson, R. E., "The Unsteady Design of Axial-Flow Turbomachines," Proceedings of the IAHR/ASME/ASCE Symposium on Hydraulic Machinery, Fort Collins, Colorado, June 14-16, 1978.

22. Fujita, H and Kovasznay, L. S. G., "Unsteady Response of an Airfoil to Wake Cutting," Johns Hopkins University Report, December 1971.

23. Holmes, D. W., "Experimental Pressure Distribution on Aerofoils in Transverse and Streamwise Gust," University of Cambridge, Department of Engineering Report CUED/A-Turbo/TR 21, 1970.

24. Kemp, N. H., "On the Lift and Circulation of Airfoils in Some Unsteady-Flow Problems," Journal of the Aeronautical Sciences, Vol. 19, No. 10, pp. 713-714, October 1952.

25. Satyanarayana, B., "Unsteady Flow Past Aerofoils and Cascades," Ph.D. Dissertation, Wolfson College, University of Cambridge, 1975.

26. Satyanarayana, B., Henderson, R. E. and Gostelow, J. P., "A Comparison Between Experimental and Theoretical Fluctuating Lift on Cascades at Low Frequency Parameters," ASME Paper 74-GT-78, 1974.

27. Satyanarayana, B., "Some Aspects of Unsteady Flow Past Airfoils and Cascades," AGARD Conference Proceedings No. 177 on Unsteady Phenomena in Turbomachinery, April 1976.

28. Satyanarayana, B., "Unsteady Wake Measurements of Airfoils and Cascades," AIAA Journal, Volume 15, No. 5, 1977.

29. Bruce, E. P. and Henderson, R. E., "Axial Flow Rotor Unsteady Response to Circumferential Inflow Distortions," Project SQUID Technical Report, PSU-13-P, September 1975.

30. Howell, A. R., "The Present Basis of Axial Flow Compressor Design: Part I - Cascade Theory and Performance," Aeronautical Research Council R and M 2095, June 1942.

31. Bruce, E. P., "The ARL Axial Flow Research Fan - A New Facility for Investigation of Time-Dependent Turbomachinery Flows," ASME Paper No. 74-FE-27, 1974.

32. Krohn-Hite Corporation, "Operating and Maintenance Manual," Model 3342, Cambridge, Mass.

33. Bruel & Kjaer, "Instructions and Applications, Half-Inch Condenser Microphones," 1969.

34. Ostdiek, F. R., "A Cascade in Unsteady Flow," AGARD Conference Proceedings No. 177 on Unsteady Phenomena in Turbomachinery, April 1976.

35. Carta, F. O. and St. Hilaire, "Experimentallly Determined Stability Parameters of a Subsonic Cascade Oscillating Near Stall," ASME Paper No. 77-GT-47, Presented at ASME Gas Turbine Conference, Philadelphia, Pennsylvania, March 1977.

36. Bruce, E. P. and Henderson, R. E., "Axial Flow Rotor Unsteady Response to Circumferential Inflow Distortions," AGARD

Conference Proceedings No. 177 on Unsteady Phenomena in Turbomachinery, April 1976.

37. Wood, A., Acoustics, Dover Publications, Inc., New York, pp. 105.

38. Alster, M., "Improved Calculation of Resonant Frequencies of Helmholtz Resonators," Journal of Sound and Vibration, No. 24, pp. 63-85, 1972.

39. Hersh, A. S. and Rogers, T., "Fluid Mechanical Model of the Acoustic Impedance of Small Orifices," NASA CR-2682, 1976.

40. Iberall, A. S., "Attenuation of Oscillatory Pressure in Instrument Lines," J. Res. National Bureau of Standards, Vol. 45, No. 1, July 1950, pp. 85-108.

41. Bergh, H. and Tijdeman, H., "Theoretical and Experimental Results for the Dynamic Response of Pressure Measuring Systems," NLR Report F.238, 1965.

42. Baumuster, K. J. and Rice, E. J., "Visual Study of the Effect of Grazing Flow on the Oscillatory Flow in a Resonator Orifice," NASA TM X-3288, 1975.

43. Rogers, T. and Hersh, A. S., "Effect of Grazing Flow on Steady State Resistance of Isolated Square-Edged Orifices," NASA CR-2681, 1976.

44. Groeneweg, J. F., "Current Understanding of Helmholtz Resonator Arrays as Duct Boundary Conditions," NASA SP-207, pp. 357-368.

45. Tijdeman, H. and Bergh, H., "The Influence of the Main Flow on the Transfer Function of the Tube-Transducer Systems Used for Unsteady Pressure Measurements," NLR Report MP-72023-U, 1972.

14 March 1978
REH:GFF:jep

Appendix A

THEORETICAL RESPONSE OF TUBE-CAVITY SYSTEMS

Theoretical analyses of a tube-cavity system historically began with the classic resonator analogy. Similar to a mass on a massless spring, the significant fluid mass is assumed to be concentrated in the tube of the resonator, and the volume of the cavity acts as a massless spring, Figure A-1. This system is commonly known as a Helmholtz resonator. The resonant frequency is given in various references, e.g., [37] as

$$f_{resonant} = \frac{1}{2\pi}\sqrt{\frac{\pi d^2 c^2}{\forall(L+E)}}$$

where d is the tube diameter, c is the speed of sound, L is the tube length and $\forall$ is the cavity volume. The "end" correction, E, is added to account for the motion of the fluid outside the tube. The end correction is generally taken as 0.3d.

Alster [38] improved the basic model by considering the effects of motion of mass particles inside the cavity and was able to show the resonant frequency depends on the shape of the interior cavity.

Hersh and Rogers [39] have an excellent discussion of the progress made in theoretical analysis of tube-cavity systems and of orifices. The behavior of an orifice, similar to a tube-cavity system having a tube of negligible length, is frequently described in terms of its impedance, a complex quantity consisting of resistance and reactance. The magnitude of impedance is given by the ratio of cavity pressure to orifice velocity. For orifices,

two regimes may be considered. In the linear regime, which exists at low driving pressures, the reactance portion of the impedance is much greater than the resistance and the orifice impedance is essentially independent of incident pressure. In the nonlinear regime, at sufficiently high driving pressure, the fluid separates at the orifice and forms a jet. The orifice impedance can then be related to a time-average discharge coefficient. Although these results are not directly applicable to tube-cavity systems, it is reasonable to expect some similarities between the fluid mechanics of orifices and of tube-cavity systems.

Iberall [40] derived the tube-cavity response using the equations of momentum, energy, continuity and state. The flow is assumed laminar everywhere in the system with small sinusoidal pressure variations. Expansions were assumed polytropic and tube lengths are long compared to any tube radius. Bergh and Tijdeman [41] extended this analyses to a series of connected tubes and cavities.

The results of Iberall and Bergh and Tijdeman are used in this investigation. These analyses do not yield simple expressions. The resonant frequency predicted by Iberall, by the classical Helmholtz resonator theory and the resonant frequency indicated by dynamic calibration is shown in Figure 9. The uncertainty of the resonant frequency in the dynamic calibration indicated in Figure 11 is only a rough estimate based on the increment in driving frequency used in the dynamic calibration. Despite wave reflection effects mentioned in the discussion of the calibration setup, the resonant frequencies indicated by the dynamic calibration agree reasonably well with the values predicted by Helmholtz and

Iberall. The dynamic sensitivity of the Pitran transducer at low frequencies is generally within 2 db of the statically determined value.

The presence of flow parallel to the blade surface influences the tube-cavity response. The momentum of the tube inflow, or outflow, interacts with the momentum of the parallel flow past the blade. Baumeister and Rice [42] used thin streams of dye to observe streamlines in the parallel flow and in the tube flow. The parallel flow can act to restrict the tube outflow, or the streamline from the parallel flow can enter the tube during inflow. Thus, flow conditions are different for inflow and outflow. Rogers and Hersh [43] modeled the effect of a flow parallel an orifice subject to high pressure levels and found good agreement with experimental data.

Groeneweg [44] shows predicted and experimental data for resistance of a Helmholtz resonator versus Mach number of the parallel flow, Figure A-2. For conditions generally encountered in the AFRF, Mach number less than 0.06, the effect was small.

Tijdeman and Bergh [45] presented similar data in which the effect of the parallel flow was modeled and an expression developed which describes the response of the tube-cavity in the presence of parallel flow. Using an experimentally determined coefficient, good agreement was found between theory and experiment, Figure A-3. The effect for conditions encountered in this investigation is small.

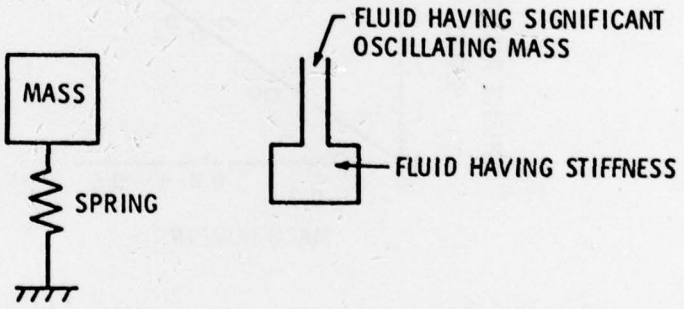


Figure A-1 - Cavity-Tube Model

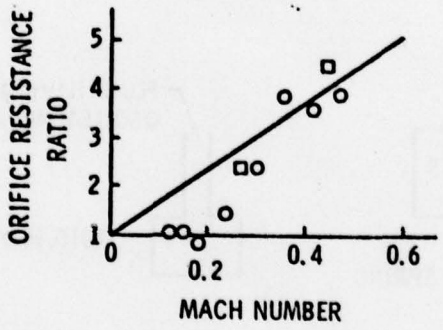
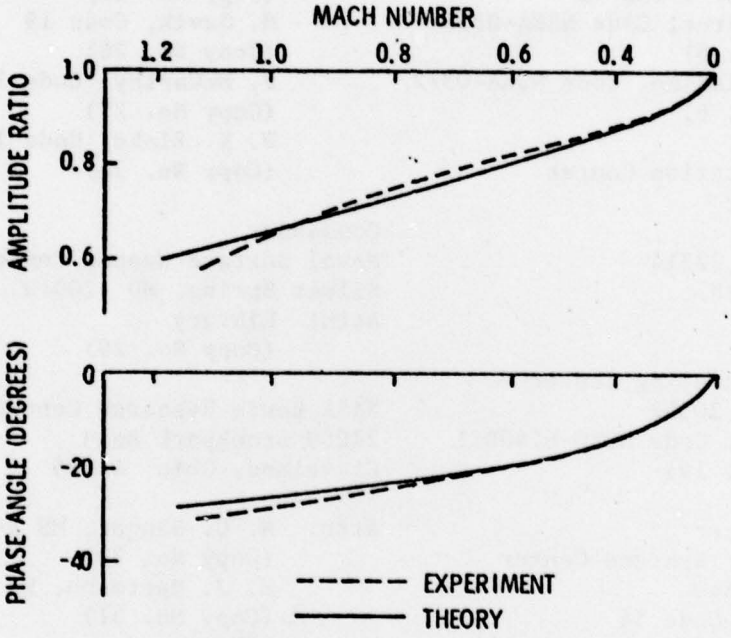


Figure A-2 - Orifice Resistance Ratio versus Mach Number, [44]



NOTE: INPUT FREQUENCY IS APPROXIMATELY ONE HALF OF RESONANT FREQUENCY FOR THE CONDITION SHOWN

Figure A-3 - Mach Number Effects on Cavity-Tube Response, [45]

DISTRIBUTION LIST FOR ARL UNCLASSIFIED TM 78-54 by R. E. Henderson and G. F. Franke dated 14 March 1978

Commander
Naval Sea Systems Command
Department of the Navy
Washington, DC 20362

Attn: Library, Code NSEA-09G32
(Copy Nos. 1 and 2)
Code NSEA-0342
(Copy Nos. 3 and 4)
T. E. Peirce, Code NSEA-0351
(Copy No. 5)
A. R. Paladino, Code NSEA-0372
(Copy No. 6)

Defense Documentation Center
5010 Duke Street
Cameron Station
Alexandria, VA 22314
(Copy Nos. 7 - 18)

Commander
Naval Ship Engineering Center
Washington, DC 20362
Attn: D. Burke, Code NSEC-6140B.1
(Copy No. 19)

Commanding Officer
Naval Underwater Systems Center
Newport, RI 02840
Attn: Library, Code 54
(Copy No. 20)

Commanding Officer
Naval Ocean Systems Center
San Diego, CA 92152

Attn: D. Nelson, Code 2542
(Copy No. 21)
Library
(Copy No. 22)

Officer In Charge
David W. Taylor Naval Ship R&D Center
Annapolis Laboratory
Department of the Navy
Annapolis, MD 21402
Attn: J. G. Stricker, Code 2721
(Copy No. 23)

Commander
David W. Taylor Naval Ship R&D Center
Department of the Navy
Bethesda, MD 20084

Attn: W. B. Morgan, Code 154
(Copy No. 24)
R. Cumming, Code 1544
(Copy No. 25)
M. Sevik, Code 19
(Copy No. 26)
J. McCarthy, Code 1552
(Copy No. 27)
W. K. Blake, Code 1942
(Copy No. 28)

Commander
Naval Surface Weapon Center
Silver Spring, MD 20910
Attn: Library
(Copy No. 29)

NASA Lewis Research Center
21000 Brookpark Road
Cleveland, Ohio 44135

Attn: N. C. Sanger, MS 5-9
(Copy No. 30)
M. J. Hartmann, MS 5-9
(Copy No. 31)
Library
(Copy No. 32)
J. Dittmar, MS 501-4
(Copy No. 33)
C. Feiler, MS 501-4
(Copy No. 34)

NASA Ames Research Center
Moffett Field, CA 94085
Attn: Dr. S. Bodapati, MA 227-9
(Copy No. 35)

Office of Naval Research
Department of the Navy
Arlington, VA 22217
Attn: J. Patton
(Copy No. 36)

DISTRIBUTION LIST FOR ARL UNCLASSIFIED TM 78-54 by R. E. Henderson and G. F. Franke dated 14 March 1978 (Continued)

Detroit Diesel Allison Division
P. O. Box 894
Indianapolis, Indiana 46206
Attn: Dr. S. Fleeter
(Copy No. 37)

United Aircraft Research Laboratory
East Hartford, Connecticut 06108
Attn: Dr. F. Carta
(Copy No. 38)

Massachusetts Institute of Technology
77 Massachusetts Avenue
Cambridge, Massachusetts 02139
Attn: Dr. E. M. Greitzer
(Copy No. 39)

Virginia Polytechnic Inst. &
State University
Mechanical Engineering Department
Blackburg, Virginia 24061
Attn: Mr. W. F. O'Brien, Jr.
(Copy No. 40)

Dr. John H. Horlock
Vice Chancellor
University of Salford
Salford, M5 4WT
ENGLAND
(Copy No. 41)

Dr. T. H. Okiishi
Mechanical Engineering Department
Iowa State University
Ames, Iowa 50010
(Copy No. 42)

Von Karman Inst. for Fluid Dynamics
Turbomachinery Laboratory
Rhode-Saint-Genese
BELGIUM
Attn: Library
(Copy No. 43)

Dr. D. S. Thompson
Turbine Research Department
Rolls Royce Ltd.
P. O. Box 31
Derby, ENGLAND
(Copy No. 44)

Whittle Turbomachinery Laboratory
Madingley Road
Cambridge, ENGLAND

Attn: Library
(Copy No. 45)
Dr. D. S. Whitehead
(Copy No. 46)

Prof. R. E. Peacock
School of Mechanical Engineering
Cranfield, Bedford MK430AL
ENGLAND
(Copy No. 47)

Prof. J. P. Gostelow
School of Mechanical Engineering
NSW Institute of Technology
Broadway
Sidney, AUSTRALIA
(Copy No. 48)

Applied Research Laboratory
Post Office Box 30
State College, PA 16801

Attn: R. E. Henderson
(Copy No. 49)
F. S. Archibald
(Copy No. 50)

Dr. P. van Oossanen
Netherlands Ship Model Basin
P. O. Box 28
6700 AA Wageningen
THE NETHERLANDS
(Copy No. 51)

GTWT Library
Applied Research Laboratory
Post Office Box 30
State College, PA 16801
(Copy No. 52)